Doctoral thesis
博士論文

Investigations on surface phonon-polariton thermal transport in dielectric multilayers

（誘電体多層膜における表面フォノンポラリトンの熱輸送に関する研究）

Associate Professor Masahiro NOMURA

Department of Electrical and Information Systems,
Graduate school of Engineering, The University of Tokyo,

37-187067,　Saeko Tachikawa

Abstract

Surface phonon-polaritons (SPhPs) are hybridization of phonons and photons at the interface of a dielectric material, and those waves propagate along the interface in the infrared range. Recent studies demonstrate theoretically and experimentally that SPhPs can contribute to thermal transport in membranes in the in-plane direction. Thermal transport by SPhPs is even predominant in nanofilms where surface-to-volume ratio is higher. Therefore, SPhP is now in great interest as another heat carrier, especially in semiconductor industries where the device structure is miniaturized into nano-scale and local heating causes crucial damage to transistor performances.

However, a suspended nanofilm is technically challenging to fabricate and not a realistic structure in an application point of view.

Here, we study SPhP propagation in SiO_2/Si/SiO_2 three-layered systems, in which SPhPs generated in SiO_2 nanolayers can couple inside a non-absorptive, 10-μm-thick Si layer.

In our theoretical studies, we calculate SPhP dispersion relation in the system to investigate its in-plane propagation length and thermal conductivity. We also analyse SPhP thermal conductivity in the system as a function of SiO_2 and Si thicknesses.

In experimental studies, we experimentally investigate the SPhP in-plane propagation through a gap. It is well-known that cross-plane evanescent component of SPhP can carry thermal energy to another body at a close vicinity (near-field radiative heat transfer), and exceed the heat exchange of blackbody limit. Recent studies have shown that the in-plane propagative component of SPhPs can also contribute to far-field radiative heat transfer over the blackbody limit, as for absorbent materials. In this work, we experimentally demonstrate that far-field radiative heat transfer between non-absorbent bodies can also overcome the blackbody limit by simply coating them with an absorbent material. The demonstration was conducted by measuring the gap thermal conductance between SiO_2/Si/SiO_2 three-layered systems, and compare it to its counterpart in pristine Si layer system. We find that SPhP generated inside the SiO_2 layers couple with the resonant guided modes inside the Si layer and transport energy through the non-absorbent thick Si layer. The gap thermal conductance obtained for the three-layered system is almost twice higher than that of the

Si-only system. We analyse the results based on the conventional Planck's theory on radiative heat transfer in far-field regime and find that it cannot explain the enhancement. We investigate the in-plane SPhP energy distribution and calculate an effective gap thermal conductance of SPhP resonant guided modes which is in a relevant agreement with the experimental results.

Our findings show that SPhP can propagate its energy in non-absorbent materials and also contribute to the far-field radiative heat transfer beyond the blackbody limit, between non-absorbent bodies of dimensions comparable to or greater than the dominant radiation wavelength. This outcome was obtained with relatively simple geometries, and thus, opens new perspectives in terms of thermal management in silicon devices and of radiation.

Contents

List of Figures

Chapter 1

Introduction

1.1 Macro- and Nano- scale heat transport

Heat transfer is one of the most familiar phenomena in our daily life, with its mechanism being well-studied over centuries. It is known that there are three different mechanisms to carry the thermal energy: conduction, thermal radiation, and convection. Conduction is the transfer of energy through microscopic collisions of particles such as molecules, atoms and electrons inside a body, and it takes place in all phases of solid, liquid and gas. Radiative heat transfer is the transfer by electromagnetic waves, generated from thermal motions of particles, carrying energy in distances regardless of existence of medium. Convection is based on thermal transport by movements of particles in a mass or fluids. In this work, we mainly focus on conduction and radiative heat transfer. In both cases, recent studies have revealed that the thermal transfer physics in micro-, to nano-scales are different from the macroscopic, well-known classical theories.

The establishment of the classical theory of thermal conduction dates back to 1822, when Jean Baptiste Joseph Fourier formulated the so-called Fourier' s law [20], which states that the heat flux is proportional to the temperature gradient and opposite to it in sign:

$$\boldsymbol{j} = -\kappa \boldsymbol{\nabla} T, \tag{1.1}$$

where $\boldsymbol{j}$ is the heat flux density and $\boldsymbol{\nabla}$T is the temperature gradient. The coefficient κ is defined as the thermal conductivity. This is a material-based value, which is independent of the body size when the mean free path of phonons, quantized units of lattice vibrations which carries thermal energy, is much smaller than the characteristic size length, L, of the body. We call this regime diffusive. Mean free path (MFP) of phonons are typically in the range of micro-, nano-meters. Therefore, when the system size is reduced to micro- or even nanostructures, which is as comparable or smaller than the mean free path, phonon transport is not diffusive anymore. In such case,

phonons are more likely to be scattered at boundaries of the system and probabilities of this event start to substantially impact thermal conductivity, which is no longer independent of the size of the system. We call this regime ballistic or quasi-ballistic if internal scattering still exists. (Fig. 1.1).

Thermal conduction becomes less efficient in the system of micro-, and nanometric scale, as phonon-boundary scattering outperforms phonon-phonon scattering in suppressing phonons traveling in distances [21, 22, 23]. Therefore, thermal management is more challenging in micro-, nano-scale system and it is in great interest especially among semiconductor industries where transistor sizes are dramatically decreasing, generating non-negligible heat damage to the device and alter its performance. On the contrary, surface phonon-polaritons, hybridized electromagnetic waves and phonons at the interface, show more efficient energy transfer as the system scales down, which is introduced in the next section.

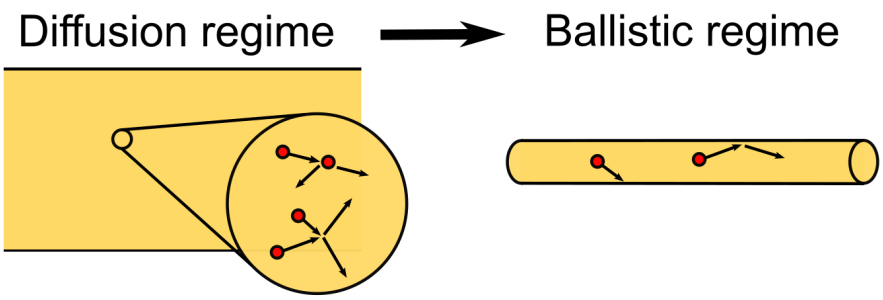

Figure1.1 Diffusive (left) and ballistic (right) regimes. As the system size is shorter than the phonon mean free path, ballistic transfer becomes predominant.

1.2 Introduction of SPhP

Surface phonon-polaritons (SPhP) are the result of the hybridization between optical phonons at an interface of a polar-material and electromagnetic waves (Fig. 1.2). As atoms of polar materials oscillate, they act like dipoles and emit electromagnetic waves in the corresponding spectrum. This radiation at the interface will again excite the charge oscillation and yield phonon and photon coupling. This hybrid excitation is called surface phonon-polariton (SPhP). Its energy intensity is confined at the interface, and decays exponentially in the out-of-plane direction. It propagates in the in-plane direction and its resonance frequency lies in the infrared range, thus, it is known to carry thermal energy along the interface. Recent studies have revealed that it can propagate

by more than hundreds of μm, and since the surface effects predominate over the volumetric ones when the surface-to-volume ratio increases, it is now of great interest as another heat carrier especially in nanomaterials.

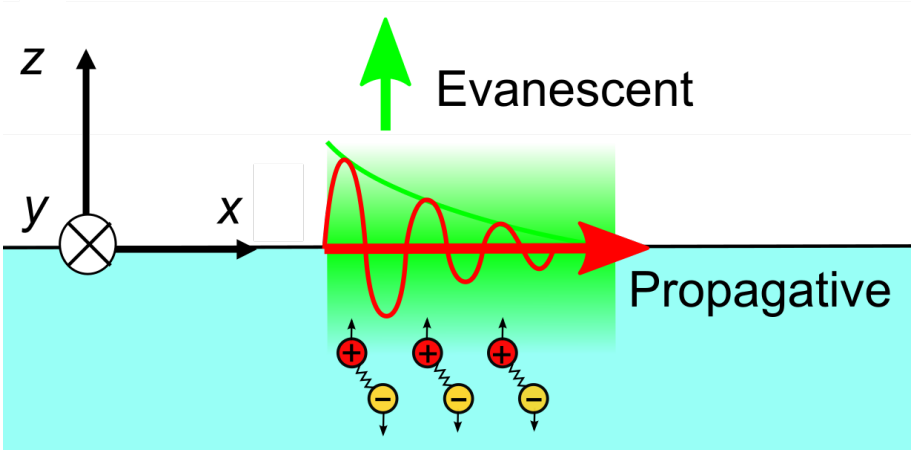

Figure1.2 Schematic image of surface phonon-polaritons generated by the oscillation of polar molecules coupled by electromagnetic waves at the interface of a polar material. The energy is confined at the interface with an evanescent in the cross-plane direction and is propagating in the in-plane direction.

1.2.1 SPhP thermal transport in the cross-plane direction

In macro-scales, Planck's s law is the fundamental principle in the study of radiative heat transfer. According to Stefan-Boltzmann's law, which is a consequences of Planck's law, the total emissive power of an object is proportional to T^4, the forth power of its temperature, with the Stefan-Boltzmann constant σ as proportionnality coefficient. This formula yields the maximum radiative heat flux between two flat plates separated by a vacuum to be $\sigma(T_1^4 - T_2^4)$, when the temperatures of the two plates are referred to as T_1 and T_2. This flux only depends on the temperature to the fourth power difference and does not depend on the distance of separation. This regime is called far-field radiative heat transfer. However, the Stefan-Boltzmann's law is only consistent when separation scales are much larger than the critical distance of λ_T which is the Wien's wavelength [1]. Gap separation below this scale generates overlap of evanescent waves at the surfaces of both plates (Fig. 1.3a).

This evanescent coupling contributes to energy exchange enhanced above Planck's limit (Fig. 1.3b) [2] by a few orders of magnitude compared to that of far-field. Excitation of near-field radiative heat transfer is stronger in polar materials or highly doped materials where there are more charges to induce phonon-photon coupling [24, 3]. Radiation is also known to be monochromatic

in this near-field regime, showing peak at the resonant frequency defined by the dielectric function of the material (Fig. 1.4a) [24, 3].

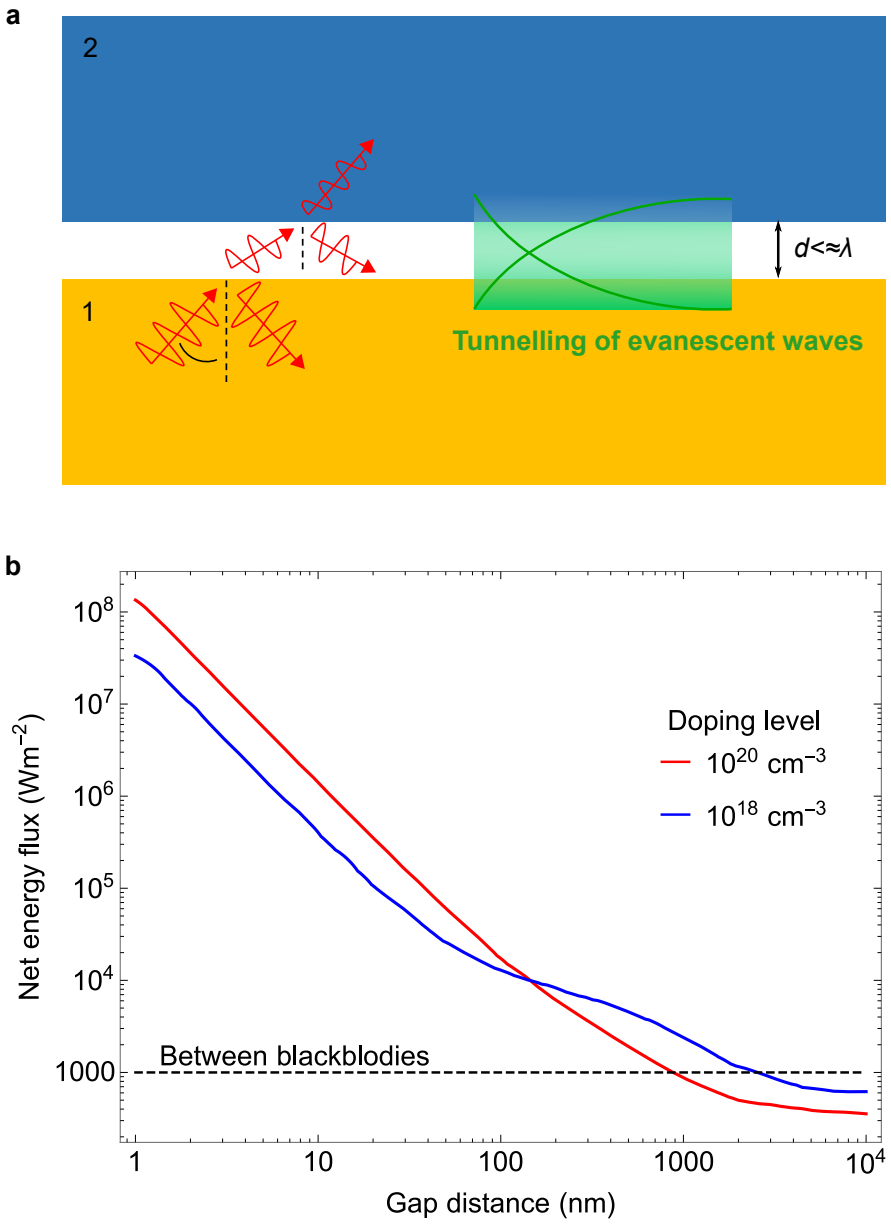

Figure1.3 **a** Schematic image of far-field and near-field radiative heat transfer [1]. **b** Net energy flux between doped-Si at different doping levels versus gap width. The dashed line refers to the net energy transfer between two blackbodies. The emitter side and the receiver side are maintained at 400 K and 300 K, respectively [2].

Near-field radiative heat transfer is also demonstrated experimentally, although the number of experiments is limited compared to the one of theoretical studies due to difficulties in making a nanometric gap between two objects. One approach is to use atomic force microscopy (AFM)

or scanning tunnelling microscope (STM) tips or spheres to achieve a gap in the nanometer scale [25, 26, 27, 28, 29, 30]. This approach is successful in terms of achieving extremely small gaps, down to a few nanometers. However, theoretical description of near-field radiative heat transfer is complicated for curved surfaces. Another approach is to position two flat plates in their close vicinity [31, 32, 33, 4, 6, 34, 35]. The results are often well-fitted, since theoretical calculations of heat exchanges between flat surfaces is well established. But, due to the difficulties of aligning large flat areas separated by a nano-gap without any dust or snap-in and with a good parallelism, achievable gap size remains larger than the tip-plate cases (Fig. 1.4b). In both approaches, it is challenging to estimate the gap size precisely with errors less than one nanometer, which is critical for gap less than a few tens of nanometers.

1.2.2 SPhP thermal transport in in-plane direction

While SPhP can carry thermal energy only within a wavelength scale in cross-plane direction, it is known to carry energy for a larger distance along the interface. Propagation of surface waves can be described by solving Maxwell's equations at the interface under certain boundary conditions. This derivation provides electric field decaying exponentially in the cross-plane direction and propagating in the in-plane direction (see discussion in Chapter 2). In suspended nanofilms, SPhPs propagating over typical distances of a few hundreds of micrometers along their interfaces [36]. This fact positions them as powerful energy carriers to transport energy along the plane of nanomaterials especially while phonons conduction is suppressed in such materials. Ordonez-M., *et al.* also proposed that SPhPs would perform as an alternative channel to heat transfer in nano-scale structures [37]. Although SPhP in-plane thermal transfer in a nanofilm is well studied theoretically, experimental demonstrations are very limited due to difficulties in suspending a nanofilm and distinguishing SPhP contribution to heat from conduction by phonons [16, 15] (see discussion in Part 3).

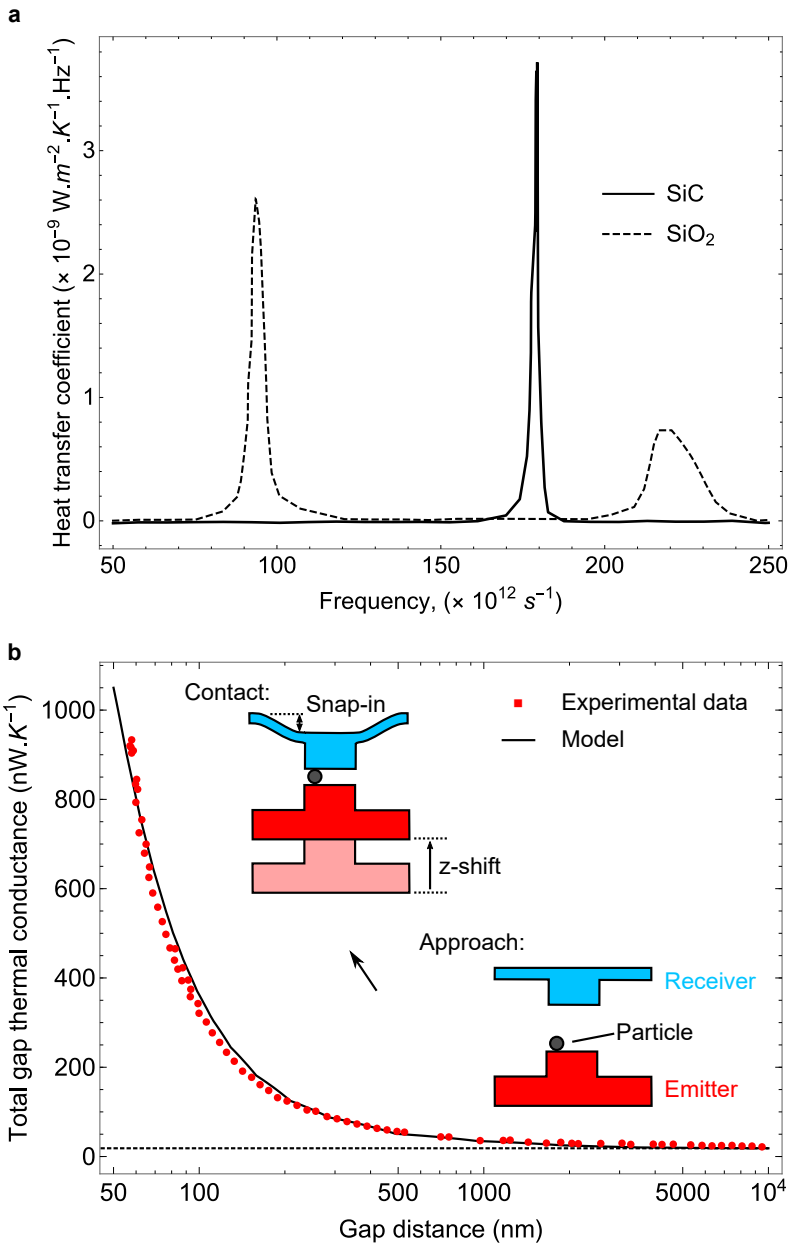

Figure1.4 **a** Monochromatic radiative heat transfer coefficient versus frequency for two semi-infinite bodies of SiC or glass separated by a distance d =10 nm at T = 300 K [3]. **b** Comparison of the measured radiative thermal conductance (displaced by 55 nm) with computational data. Dashed line: radiative conductance between black-body surfaces Insets: the minimum achievable gap size is limited by the presence of nanoscale particles and snap-in [4].

1.3 Thermal management and applications

Near-field thermophotovoltaic systems (TPV) are of great interest to enhance the efficiency of conventional TPV. A TPV system is an energy conversion device that generates electric power out of heat through radiative heat transfer. The key advantage of TPV systems is utilization of the wasted heat. The system consists of an emitter and a photovoltaic (PV) cell [38]. The cell is basically a p-n junction semiconductor. As the emitter is heated, emitted radiation creates electron-hole pairs inside the cell. Only the photons with energy within the band gap of the cell can contribute to the generation of the electron-hole pair. By positioning the emitter and the TPV cell closer in the near-field regime with monochromatic emission, radiative heat transfer into the cell should dramatically increase. Fiorino, *et al.* has conducted an experimental proof of concept [5]. A microfabricated emitter was located above a PV cell (Fig. 1.5 a). Photons are emitted from the hot emitter and absorbed in the p-n junction cell. The gap size is controlled by piezoelectric actuation underneath the cell. The power output was measured while reducing the gap size for different temperature (Fig. 1.5 b). A 40-fold enhancement in power output in NFTPV systems was reported in direct comparison to otherwise identical far-field TPV systems. The modelled energy flux spectrum from emitter to cell is also plotted in Fig. 1.5c. The figure shows the computed spectral energy flux at the smallest gap (d = 60 nm) when the emitter is at 655 K. The green region represents the maximum energy extracted by the TPV at this gap size, whereas the red regions represent losses. At a 60 nm gap, the energy flux exceeds the limit for blackbodies more than threefold.

Using a phase change material enables a thermal switch or rectifier of a high energy density due to the near-field radiative heat transfer. The group of L. Wang has reported theoretical prediction of a thermal switch using vanadium dioxide [39]. The vanadium dioxide undergoes a phase-change from the insulating state to the metallic state around 340 K [40]. They predicted that 80% heat transfer reduction when the gap distance between the emitter and the receiver of vanadium oxide is less than 30 nm. The experimental demonstration was done by K. Ito, *et al.* [6].

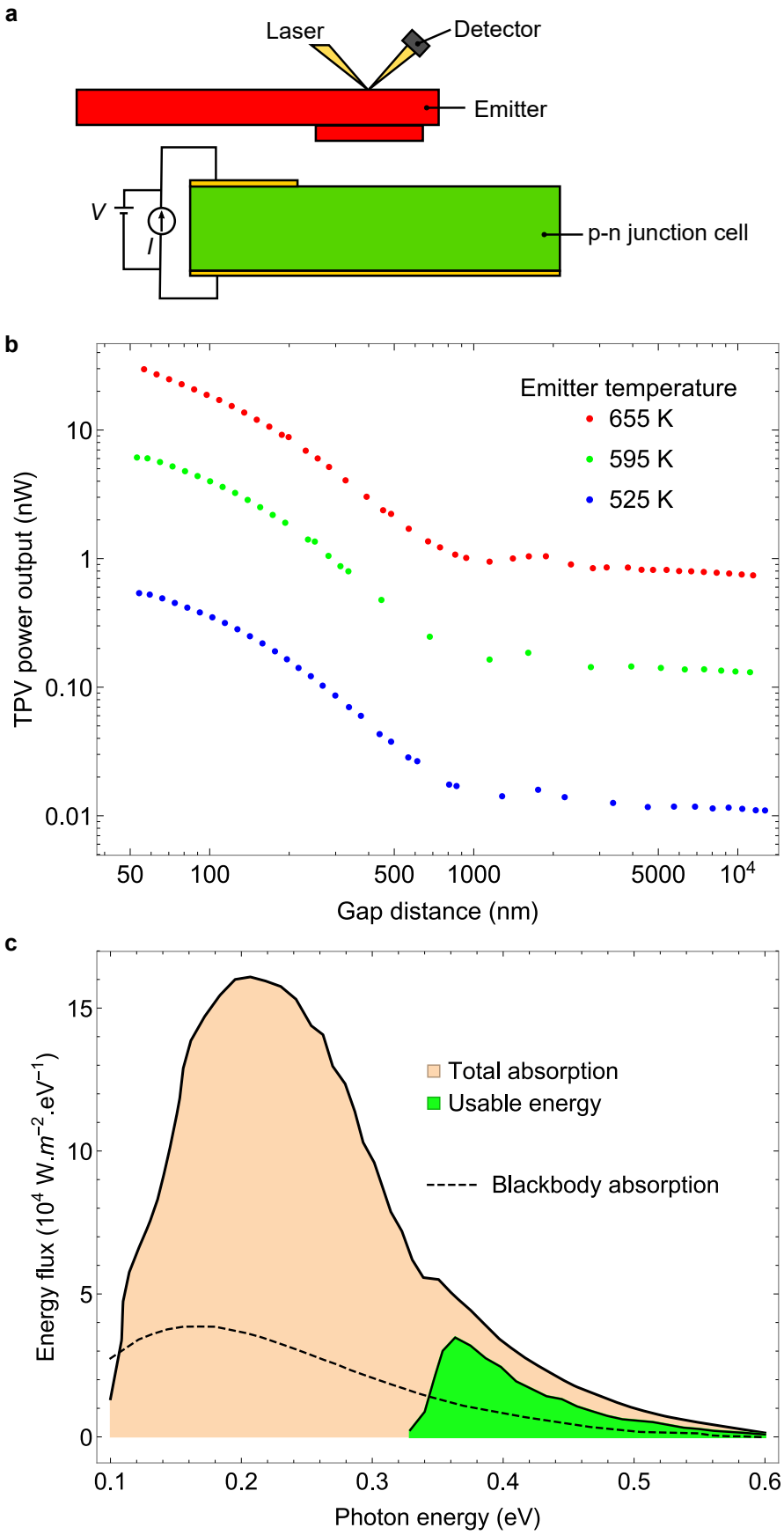

Figure1.5 **a** Schematic side view of the TPV measurement setup. **b** Measured power output versus gap size for emitter temperature ranging from 525 K to 655 K. **c** Calculated spectral energy flux for emitter temperature of 655 K and gap size d = 60 nm [5].

They built up the setup in which an emitter and a receiver of silicon dioxide are brought into contact by a compressive spring (Fig. 1.6a). Vanadium dioxide is deposited on the receiver to modulate the radiative heat flux by its change of permittivity. They fabricated spacers to guarantee the constant gap size, which was measured by an interferometer. Figure 1.6b shows the measured heat flux. The gap and the temperature difference between the emitter and the receiver were fixed at 370 nm and 60 K, respectively. The vanadium oxide was doped with tungsten to lower the phase-change temperature. They obtained almost twice the difference in the heat flux when the receiver temperature was lower at T_R = 295 K to maintain vanadium dioxide at insulator state and when T_R = 325 K for vanadium oxide changing to metal state.

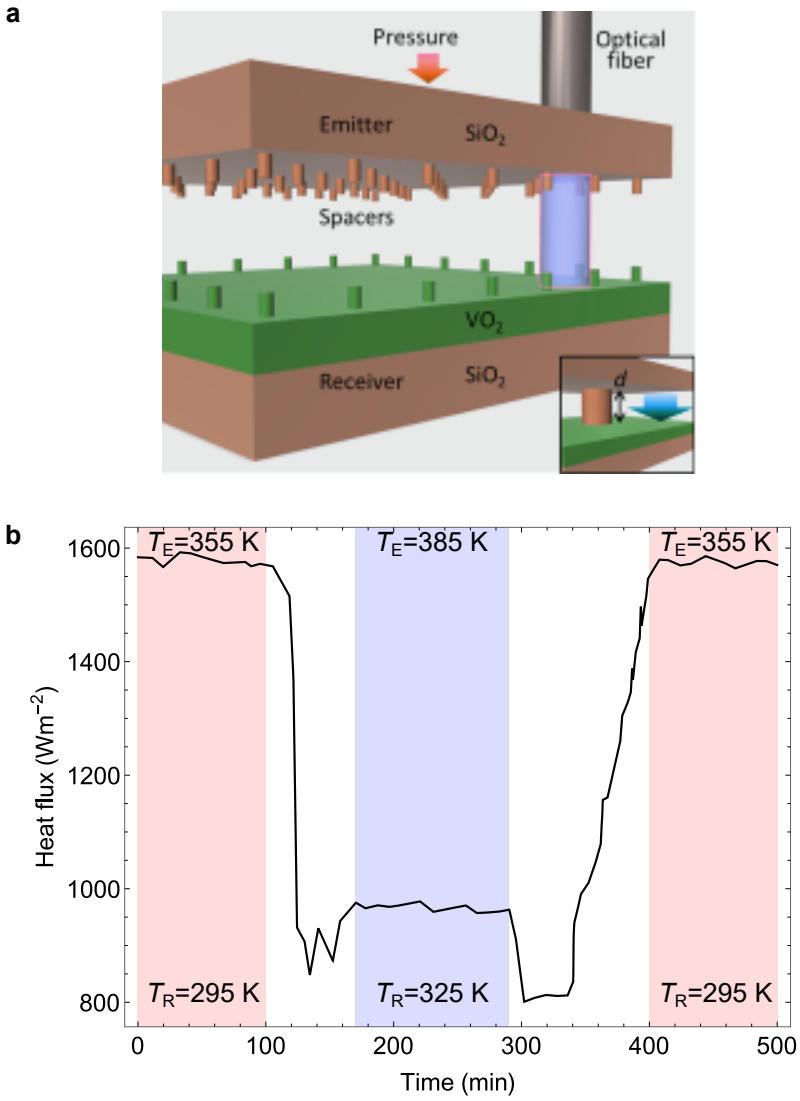

Figure1.6 **a** Schematic of near-field radiative thermal rectifier [6]. **b** Measured transient heat flux before and after the phase-change of the vanadium dioxide. [6].

Another interesting application consists in modifying the emissivity of the surface by diffracting the SPhPs. The first demonstration of a tuning SPhP emission was the work by Greffet *et al.* [7]. They fabricated the gratings on the surface of SPhP supporting material (SiC) with a periodicity designed to couple surface waves with the far-field. A coherent thermal emission was achieved by the diffraction of SPhPs (Fig. 1.7).

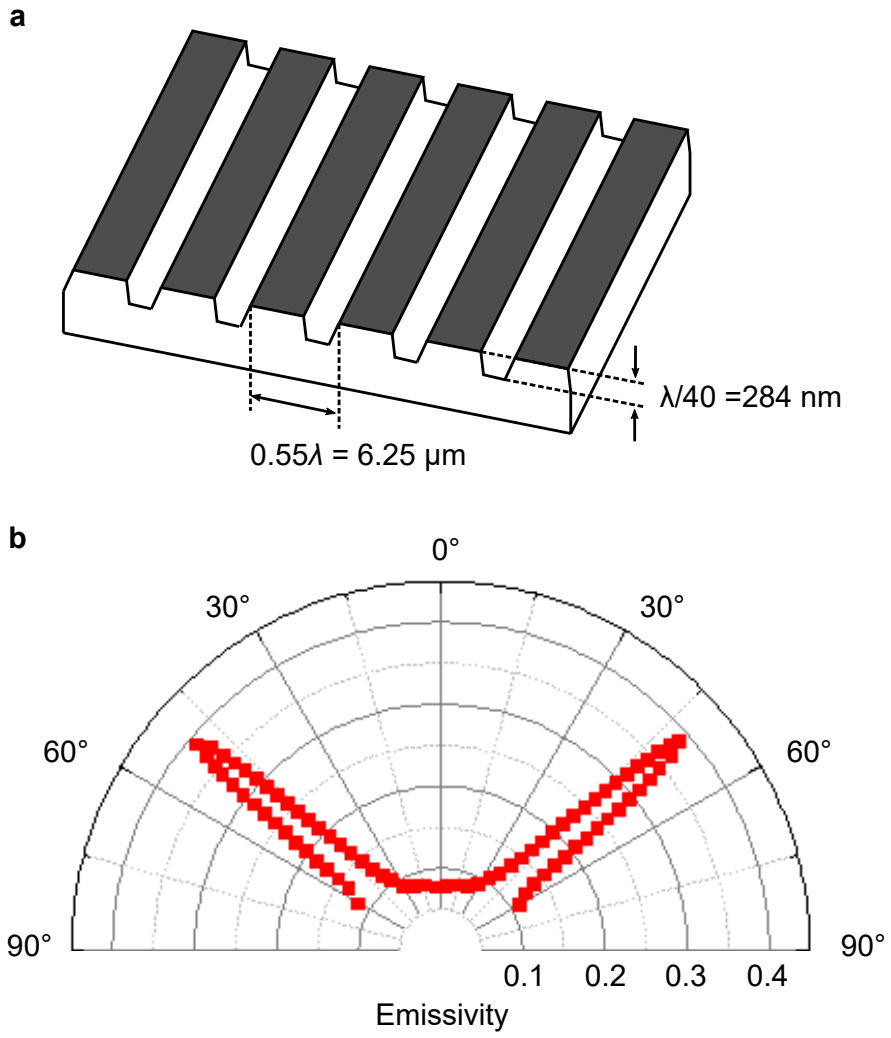

Figure1.7 **a** Schematic of SiC gratings. **b** Polar plot of emissivity of the SiC gratings [7].

This demonstration was an important concept for applications in passive cooling. Rephaeli *et al.* has integrated photonic crystals to modify emissivity matched with the atmospheric window. Figure 1.8 shows their device with two different photonic structures: A multi-layered structure to reflect radiations in the range of the solar spectrum and photonic crystals to emit radiations in the range of the atmospheric window. The photonic crystals support efficient emission into the cold

atmosphere and therefore ensure passive cooling. This is a beneficial idea in a way that it can be integrated over a large area.

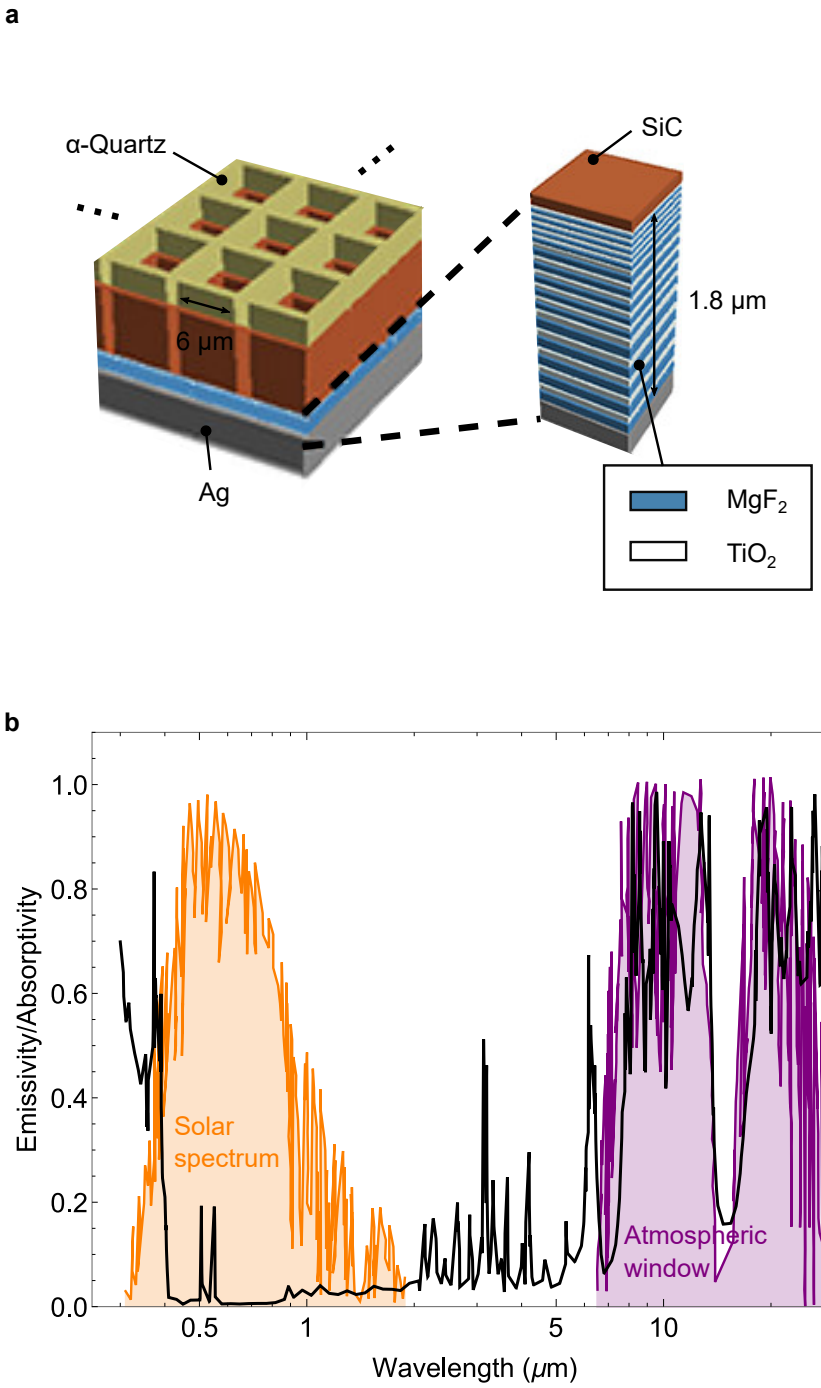

Figure1.8 **a** Schematic of a radiative cooler. Photonic crystals are patterned on the top of the multilayered solar reflector. **b** Optimized emissivity of the device [8].

1.4 Objective of this work

Although it is predicted theoretically that SPhP can act as another heat channel in the in-plane direction, not many experimental demonstrations have been conducted to deepen the understanding of its role as an energy carrier due to the difficulties in suspending a nanometric film. The objective of this work is to investigate further the SPhP thermal transport in in-plane direction using a multilayered structure. We adapt the multilayer structure of a 10-μm-thick silicon (Si) layer sandwiched by nanofilms of silicon dioxide (SiO_2), which we call SiO_2/Si/SiO_2 three-layer system throughout the rest of the thesis. The thick Si layer works as a mechanical support, whereas polar material of SiO_2 nanolayers excite SPhPs. The SPhPs generated inside the SiO_2 nanolayers would couple inside the non-absorptive Si layer and would propagate along the system. Thus, the system is expected not only to guarantee the mechanical stability, but also to show efficient thermal transport even though it is not a nanometric film as demonstrated in previous studies. Moreover, with this multilayered system, we aim an experimental demonstration of SPhP in-plane thermal transport through a gap. While radiative thermal transport through a nanogap in the cross-plane direction is well-studied, radiative thermal transport in the in-plane direction has never been proved. It has been already demonstrated experimentally that SPhPs can enhance the heat conduction in nanoiflms of polar materials [16, 15]. Therefore, if the in-plane SPhP energy is emitted from one film and absorbed in another film, SPhPs could also contribute to the radiative heat transfer in the in-plane direction through a gap. Our work is the first experimental demonstration of SPhP transport along multilayered systems and through a gap. The obtained gap radiation exceeds the far-field black-body limit according to an unexpected mechanism which is finally explained.

1.5 Outline of the thesis

This work is organized as follows.

In Chapter 2, we present the theoretical studies on SPhP propagation and thermal properties inside the SiO_2/Si/SiO_2 three-layer system. First, we start from analysis on SPhP propagation along primitive systems of a single interface and a single film, as already shown in previous studies. Next, we apply the calculations on the SiO_2/Si/SiO_2 three-layer system to derive SPhP dispersion relation and propagation length. The calculations are then compared with wave vectors obtained from numerical simulations to verify the validity of the calculations. The SPhPs thermal conductivity is also analyzed for different thicknesses of Si_2 and Si layers.

From Chapter 3 to Chapter 5, we present our experimental works.

In Chapter 3, we introduce our experimental setup to measure the radiative thermal transport between a hot and a cold plate through a gap. The setup is based on the combined techniques of 3ω technique and the Wheatstone bridge. We show our specified design of the device, which has hot and cold plate, both consisted of SiO_2/Si/SiO_2 three-layer system. We present the thermal model according to the measurement techniques and the device design.

In Chapter 4, we show fabrication techniques and process methods of the device. We use semiconductor microfabrication techniques to fabricate the suspended device and integrate metal transducers to measure the temperature on the hot and the cold plates. Process flow is presented with an introduction to each technique and machine.

In Chapter 5, we present the experimental results and provide discussions. We compare the radiative heat transfer through a gap between Si-only plates and that between SiO_2/Si/SiO_2 three-layer system and find the twice higher conductance for the SiO_2/Si/SiO_2 three-layer system. We analyse the data first by using the conventional Planck's radiation theory to verify that it cannot explain the enhancement. Then we investigated SPhP energy distribution and calculated effective gap thermal conductance accordingly to find it can fit with the experimental results. We also consider the contribution of near-field radiative heat transfer and the effect of metal transducers to the SPhP thermal transport.

The general conclusion and the prospective are provided at the end of the thesis.

Chapter 2

Theoretical studies on SPhP thermal transfer in SiO_2/Si layered syetems

2.1 Introduction to the state-of-the-art

As micro- to nanotechnology has rapidly developed, scientists focus on surface waves such as surface plasmon-polaritons and surface phonon-polaritons to enhance the performance of devices. Yang, F. *et al.* have demonstrated that a material with a complex dielectric function surrounded by dielectric media can support long-range surface modes in a thin membrane via coupling between two surfaces [41]. Many theoretical works then have been done on surface waves at the interfaces of film-based structures of different polar materials such as SiC [42, 43, 44, 45], SiO_2 [46, 45, 47, 9, 48, 10], SiN [15], and hBN [49, 50, 51, 52]. Surface phonon polariton (SPhP) is a surface wave existing at the interface of polar materials which have negative real part of the dielectric function, meaning absorptive materials. It results in a hybridization of optical phonons and electromagnetic waves. Significance of SPhP is that it propagates over hundreds of micrometers in thin films and in the infrared range [47]. Therefore, it collects attentions for its capability to carry the heat energy not only in perpendicular direction [25] but also in parallel direction to the interface, and it becomes significant in nanometric structures. The group of G. Chen has analysed the thermal property of SPhP in in-plane direction of nanofilm using the in-plane thermal conductivity defined as follows [9]:

$$\kappa = \frac{1}{4\pi d} \int_{\omega_L}^{\omega_H} \hbar\omega\Lambda\beta_R \frac{\partial f_0}{\partial T} d\omega, \tag{2.1}$$

where d is the film thickness, ω denotes the angular frequency, ω_L and ω_H are lowest and highest cut-off frequency for the SPhP modes. $\hbar$ refers to the reduced Planck's constant, β_R is the

real part of the wave vector along the interface, Λ represents the propagation length of SPhP, f_0 the Bose-Einstein distribution function, and T the temperature of the structure.

According to their theoretical predictions, the SPhP in-plane thermal conductivity of a SiO_2 film exceeds the phonon one when the film thickness is less than 50 nm (Fig. 2.1).

The film thickness analysis is further discussed in detail in terms of dispersion relations and propagation lengths for a SiO_2 film in the work of J. Ordonez-Miranda, *et al.* [10]. For thinner membranes, the dispersion relation becomes closer to the light line, showing photon-like behavior of SPhP and the propagation length becomes longer due to less absorption inside the material (Fig.2.2). The propagation length reaches ~1 cm for the thickness of 0.1 μm. Although these works indicate great possibilities of SPhP as an additional heat dissipation channel while thermal conductivity of phonons tend to decrease when the structure scales down, nanometric suspended thin films are mechanically unstable and incompatible with highly compacted structure. Taken into account that in semiconductor industries where the local heat can cause serious damages to the performance of microelectronics and vertical heterostructure with dielectric materials, further studies on SPhP in multilayered structures have become active. Ordonez-Miranda *et al.* have studied the thermal conductivity of nanolayered structure due to SPhP [11]. This study approached theoretically the effective permittivity of a layered system from the permittivity of each layer.

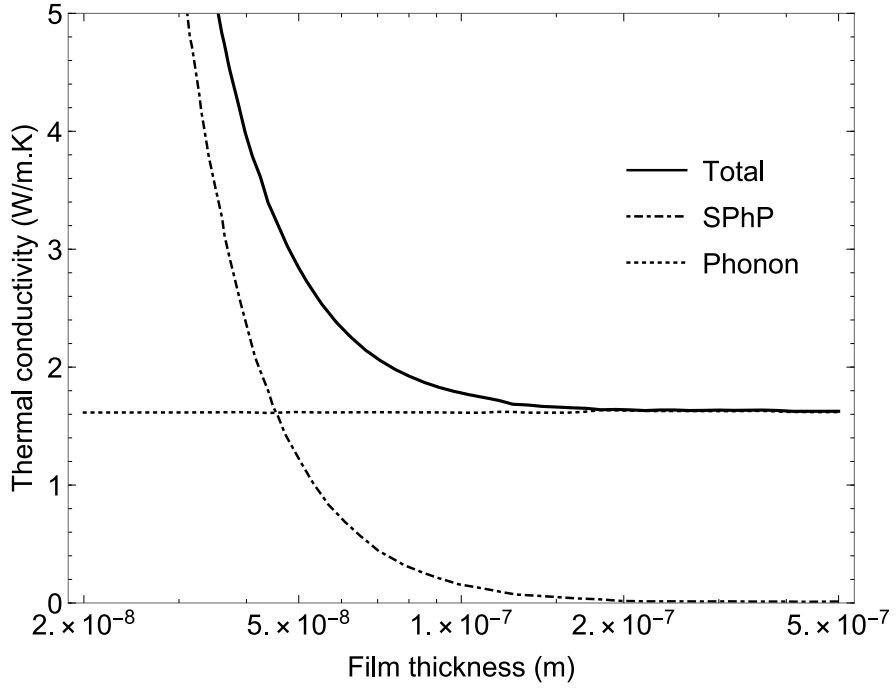

Figure2.1 Amorphous SiO_2 thermal conductivity due to phonons and surface phonon-polaritons as a function of film thickness at 500 K [9].

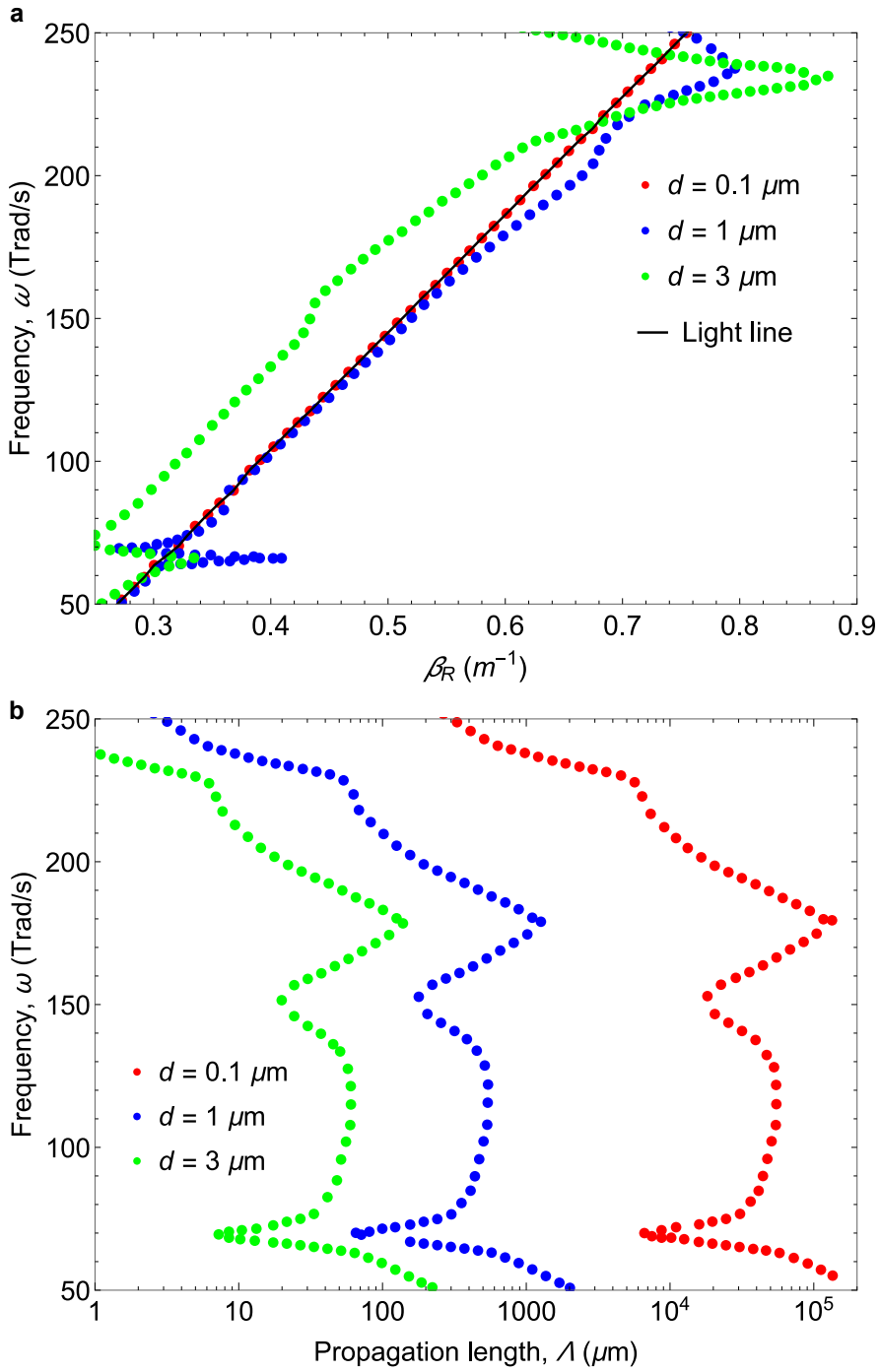

Figure2.2 **a** Dispersion relation and **b** in-plane propagation length as a function of the frequency, for suspended SiO_2 thin film [10]

.

They showed that, with optimizing both permittivities and thicknesses, layered structures can yield higher thermal conductivities than a single membrane (Fig.2.3).

They demonstrated that an ensemble of different layers provide higher thermal conductivities

due to more SPhP propagation channels. More interestingly, the nanolayered structure with a substrate of KBr (slightly higher permittivity that air, $\epsilon_{KBr} = 1.24$) yields higher thermal conductivity than the one surrounded by air. This result indicates the potential of SPhP to tackle the problem of overheating in nanolayered structures. Lim *et al.* [53] have conducted a full analysis on various combinations of different dielectrics in layered structures. They calculated analytically the dispersion relation for configurations of: Glass-Dielectric-Substrate, Dielectric-Glass-Substrate, and Glass-Dielectric-Glass-Substrate. They established a genetic computation algorithm to scan for the optimized permittivity and configurations to achieve the high thermal conductivities. Studies on enhancing the SPhP thermal conductivity in realistic geometries seen in electric devices are now in great need and interest.

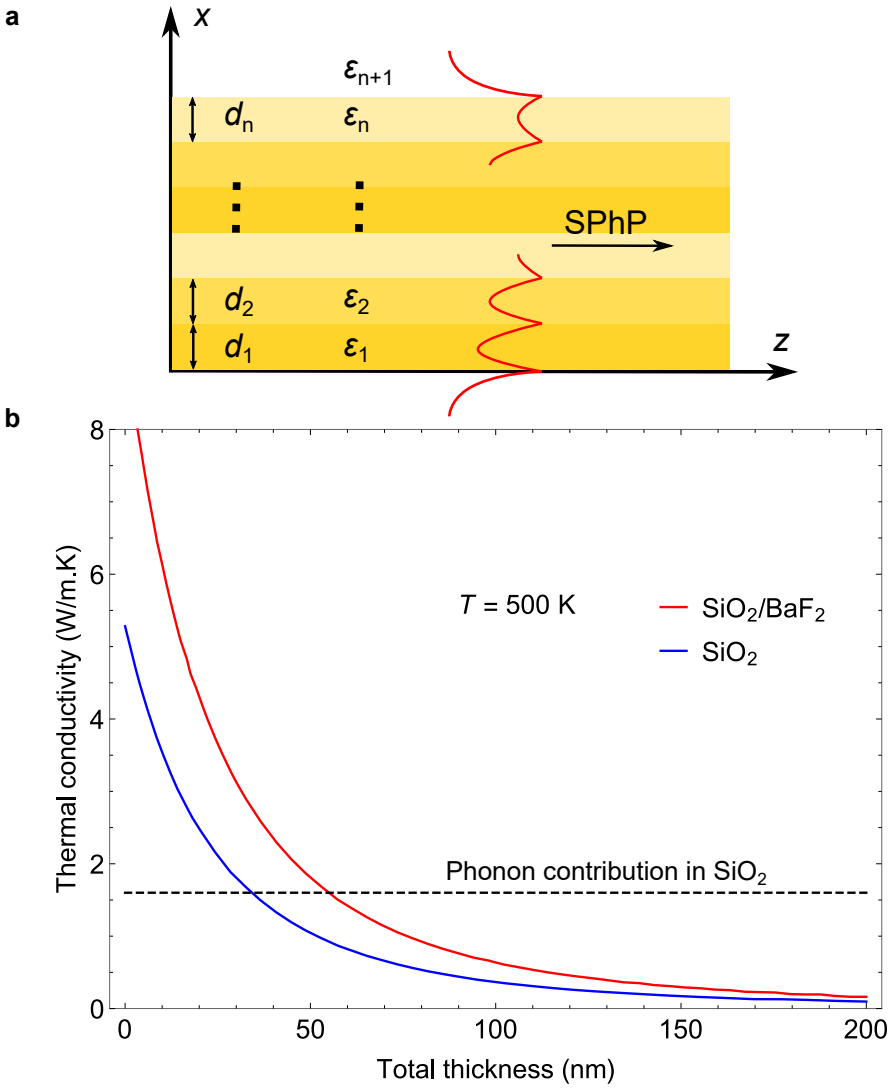

Figure2.3 **a** Schematic of the cross-section of the layered structure. **b** thermal conductivity for the single membrane of SiO_2 and layered structure of SiO_2/BaF_2 as a function of the total thickness at 500 K [11]

.

Before showing the calculations on the dispersion relation of multilayered structure, let us start from explaining the general phonon-polaritons and then to surface phonon-polariton (SPhP) dispersion relation at a single interface. After showing the calculations on SPhP in a single film, we analyse the SPhP in the three-layered system.

2.2 Introduction of phonon-polariton

2.2.1 Polarization and relative permittivity

In electromagnetism, electric flux density is defined as,

$$\boldsymbol{D} = \epsilon_0 \boldsymbol{E} + \boldsymbol{P}, \tag{2.2}$$

where ϵ_0 is a permittivity in vacuum, $\boldsymbol{E}$ is an electric field and $\boldsymbol{P}$ is a polarization. Polarization is a sum of dipole moment caused by the electric field $\boldsymbol{E}$, described as

$$\boldsymbol{P} = Nq\boldsymbol{u}, \tag{2.3}$$

where N is a number of dipoles in a unit volume, $q\boldsymbol{u}$ is a dipole moment in which positive and negative charges of q are separated by a position vector of $\boldsymbol{u}$. Assuming that the polarization is linearly dependent on the electric field, $\boldsymbol{P}$ can be expressed as

$$\boldsymbol{P} = \epsilon_0 \chi \boldsymbol{E}, \tag{2.4}$$

with the coefficient χ being electric susceptibility. Combined with Eq. 2.2, the electric flux density is rewritten as

$$\boldsymbol{D} = \epsilon_0 \boldsymbol{E} + \boldsymbol{P} = \epsilon_0 (1 + \chi) \boldsymbol{E}. \tag{2.5}$$

The relative permittivity is defined as $\epsilon_r = 1 + \chi$. To evaluate the relative permittivity of the materials which possess ion polarization, we consider polarization of ion pairs and its equation of motion which is described as

$$M \frac{\partial^2 \boldsymbol{u}}{\partial^2 t} + M\omega_0^2 \boldsymbol{u} = q\boldsymbol{E}, \tag{2.6}$$

where M is an effective mass of an ion pair and ω_0 is a frequency of lattice vibration. Applying Eq. 2.3 to the above equation of motion gives

$$\frac{\partial^2 \boldsymbol{P}}{\partial^2 t} + \omega_0^2 \boldsymbol{P} = \frac{Nq^2}{M} \boldsymbol{E}. \tag{2.7}$$

We assume the solution of $e^{-i\omega t+\boldsymbol{k}\cdot\boldsymbol{r}}$, which gives the above equation of motion as

$$(-\omega^2+\omega_0^2)\boldsymbol{P}-\frac{Nq^2}{M}\boldsymbol{E}=0. \tag{2.8}$$

Therefore, the relative permittivity is

$$\epsilon_r=1+\frac{\boldsymbol{P}}{\epsilon_0\boldsymbol{E}}=1+\frac{\epsilon_0 Nq^2/M}{\omega_0^2-\omega^2}. \tag{2.9}$$

This is a Lorentzian permittivity. Replacing ω by $\omega+i/\tau$, where τ is a relaxation time of diffusion, the relative permittivity becomes a complex number and the attenuation can be considered. The real and imaginary part of the relative permittivity are

$$\epsilon_{r,R}=1+\frac{\omega_p^2(\omega^2-\omega_0^2)}{(\omega^2-\omega_0^2)+\omega^2/\tau^2}, \tag{2.10}$$

$$\epsilon_{r,I}=1+\frac{\omega_p^2\omega/\tau}{(\omega^2-\omega_0^2)+\omega^2/\tau^2}, \tag{2.11}$$

respectively, with the plasma frequency of $\omega_p=\frac{Nq^2}{M\epsilon_0}$ [54]. Figure 2.4 shows the real and the imaginary of the permittivity of silicon carbide. The imaginary part of the relative permittivity corresponds to the absorption spectrum. The resonant frequency is at 12.56 μm, which indicates that silicon carbide is a lossy material in the infrared range.

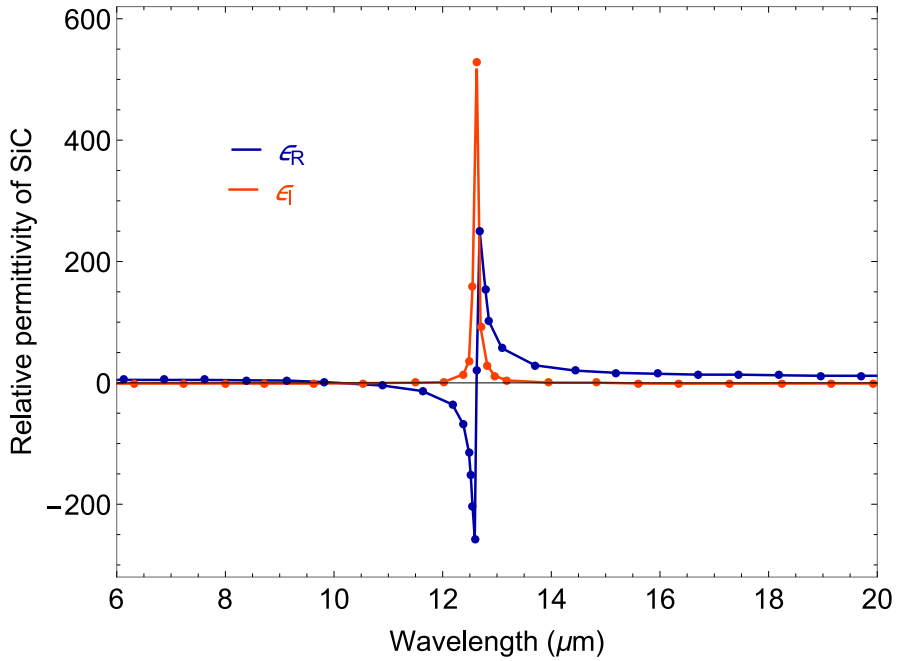

Figure2.4 Real (ϵ_R) and imaginary (ϵ_I) parts of the relative permittivity of silicon carbide reported in Ref [12].

2.2.2 Polaritons

In lattice vibrations, there exist acoustic and optical modes (Fig. 2.5). The optical modes can hybridize with electromagnetic waves and this hybridization is called phonon-polariton.

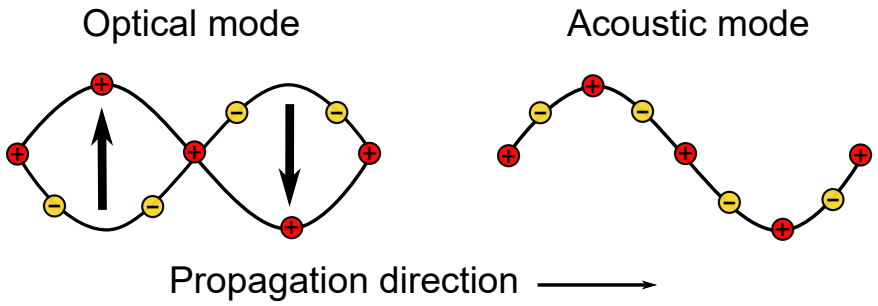

Figure2.5 (Left) Optical and (Right) acoustic mode of lattice vibration.

To describe phonon-polaritons, we combine the equation of motion and Maxwell's equations. The Faraday' s law and the Ampère' s law are

$$\boldsymbol{\nabla} \times \boldsymbol{E} = -\frac{\partial \boldsymbol{B}}{\partial t} = i\omega\mu_0 \boldsymbol{H}, \tag{2.12}$$

$$\boldsymbol{\nabla} \times \boldsymbol{H} = \frac{\partial \boldsymbol{D}}{\partial t} = -i\omega(\epsilon_0 \boldsymbol{E} + \boldsymbol{P}). \tag{2.13}$$

Substracting H from above equations gives

$$-\omega^2 \boldsymbol{P} + (c^2k^2 - \omega^2)\epsilon_0 \boldsymbol{E} = 0. \tag{2.14}$$

By combining Eq. 2.8 and Eq. 2.14, we can get the simultaneous equation as

$$\begin{bmatrix} \omega^2 - \omega_0^2 & Nq^2/M \\ \omega^2 & (\omega^2 - c^2k^2)\epsilon_0 \end{bmatrix} \begin{bmatrix} \boldsymbol{P} \\ \boldsymbol{E} \end{bmatrix} = 0. \tag{2.15}$$

The condition to solve the simultaneous equation is

$$\begin{vmatrix} \omega^2 - \omega_0^2 & Nq^2/M \\ \omega^2 & (\omega^2 - c^2k^2)\epsilon_0 \end{vmatrix} = 0, \tag{2.16}$$

which gives

$$\omega^4 - (\omega_0^2 + c^2k^2 + Nq^2/\epsilon_0 M)\epsilon_0\omega^2 + \omega_0^2 c^2 k^2 \epsilon_0 = 0. \tag{2.17}$$

The solution is

$$\omega^2 = \frac{1}{2}\left[\omega_0^2 + c^2k^2 + Nq^2/\epsilon_0 M\right] \pm \left(\frac{1}{4}\left[\omega_0^2 + c^2k^2 + Nq^2/\epsilon_0 M\right]^2 - \omega_0^2 c^2 k^2\right)^{\frac{1}{2}}, \tag{2.18}$$

which is plotted in Fig. 2.6.

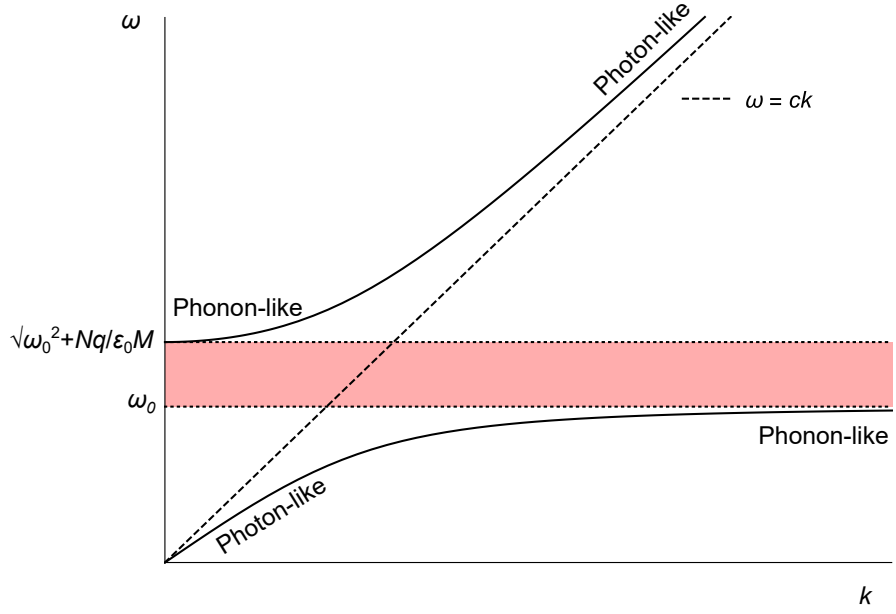

Figure2.6 Dispersion relation of phonon-polariton in a bulk.

The dispersion relation of the coupling between the lattice vibration and the electromagnetic waves is plotted in solid lines in Fig. 2.6. The dispersion relation has two branches, one starting from along the light line (photon-like behavior) and saturate along the acoustic mode of phonon (phonon-like behavior), and the other one starting from the optical mode of phonon (phonon-like behavior) and increases along the light line (photon-like behavior). The energy gap between two branches (pink zone in Fig. 2.6) corresponds to the region where the wave vector is pure imaginary and evanescent mode.

In the next section, we show the dispersion relation of surface phonon-polaritons.

2.3 SPhP dispersion relation calculation

2.3.1 SPhPs at a single interface

Surface phonon-polaritons are phonon-polaritons found particularly at the interface of dielectric materials. In a dielectric material, the bound charges polarize as outside forces or thermal energy makes charges to vibrate. According to two different types of polarizations, phonons, quanta of vibrational energy, are categorized as acoustic phonons and optical phonons.Acoustic phonons are the major carriers of heat and although optical phonons contribute negligibly to the thermal transport for its small group velocity, they easily couple with electromagnetic waves as their large polarization displacements generate electromagnetic waves. This coupling of optical phonons and electromagnetic waves in the range of resonant frequencies are surface phonon-polaritons. Suface phonon-polaritons are known to propagate along the interface and decay exponentially along the cross-plane direction, and those waves can be described by Maxwell's equations in matter:

$$\nabla \cdot \boldsymbol{D} = \rho, \tag{2.19}$$

$$\nabla \cdot \boldsymbol{B} = 0, \tag{2.20}$$

$$\nabla \times \boldsymbol{E} = -\frac{\partial \boldsymbol{B}}{\partial t}, \tag{2.21}$$

$$\nabla \times \boldsymbol{H} = \boldsymbol{J} + \frac{\partial \boldsymbol{D}}{\partial t}, \tag{2.22}$$

where $\boldsymbol{D} = \epsilon \boldsymbol{E}$ and $\boldsymbol{B} = \mu \boldsymbol{H}$. Here we consider the situation of the free point charge and electrical current, $\rho = 0$ as well as $\boldsymbol{J} = 0$.

We first consider an infinite single interface in Figure 2.7. We take x and y axis along the interface, and z axis perpendicular to the interface. Media 1 and 2 have a dielectric constant,

which is defined as the following complex quantity:

$$\epsilon_{j=1,2} = \epsilon_{R,j} - i\epsilon_{I,j}. \tag{2.23}$$

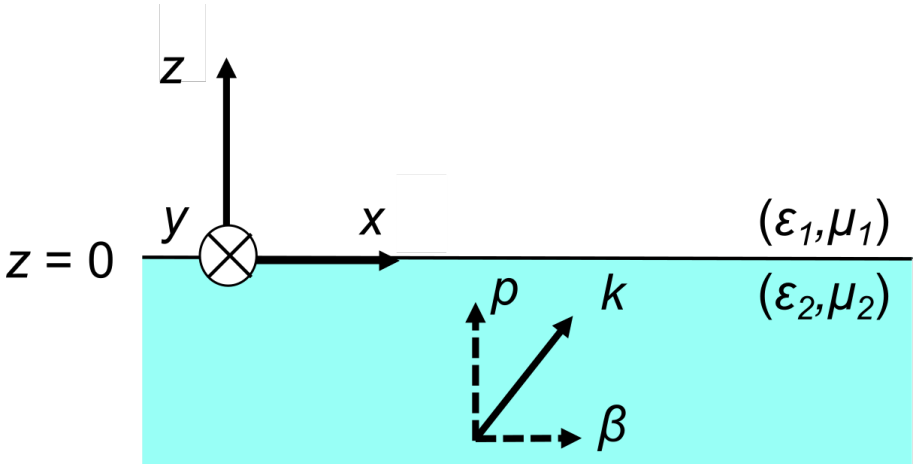

Figure2.7 Schematic of the cross-sectional view of a single interface between medium 1 and medium 2. (ϵ_1, μ_1) and (ϵ_2, μ_2) refer to dielectric functions and permeabilities of media 1 and 2 respectively.

When electric fields and magnetic fields fluctuate with time, they take forms of;

$$\boldsymbol{E}(\boldsymbol{r}, t) = \boldsymbol{E}(\boldsymbol{r})e^{i\omega t}, \tag{2.24}$$

$$\boldsymbol{H}(\boldsymbol{r}, t) = \boldsymbol{H}(\boldsymbol{r})e^{i\omega t}. \tag{2.25}$$

Replacing Eqs. 2.21 and 2.22 with electric field and magnetic field described above gives

$$\boldsymbol{\nabla} \times \boldsymbol{E} + i\mu\omega\boldsymbol{B} = 0, \tag{2.26}$$

$$\boldsymbol{\nabla} \times \boldsymbol{B} - i\epsilon\omega\boldsymbol{B} = 0. \tag{2.27}$$

Applying rotor to both Eqs. 2.26 and 2.27 yields

$$(\boldsymbol{\nabla}^2 + \mu\epsilon\omega^2)\boldsymbol{E} = 0, \tag{2.28}$$

$$(\boldsymbol{\nabla}^2 + \mu\epsilon\omega^2)\boldsymbol{B} = 0. \tag{2.29}$$

Since TM mode is predominant for surface waves and propagates along the x axis, E_z is independent of y and Eqs. 2.28 and 2.29 are then reduced to

$$\frac{\partial^2 E_{x,j}}{\partial^2 z} - p_j^2 E_{x,j} = 0, \tag{2.30}$$

$$H_{y,j} = \frac{-i\omega\epsilon_j}{p_j^2}\frac{\partial E_{x,j}}{\partial z}, \tag{2.31}$$

$$E_{z,j} = \frac{-i\beta}{p_j^2}\frac{\partial E_{x,j}}{\partial z}, \tag{2.32}$$

while p_j is defined as

$$p_j^2 = \beta^2 - \epsilon_j k_0^2, \tag{2.33}$$

where j=1,2, k_0=ω/c and c is the speed of light in vacuum. To derive the dispersion relation, we discuss the continuity on the interface region where $z = 0$ to set the boundary condition for solving. The continuity of the electric field writes:

$$E_{x,1} = E_{x,2}. \tag{2.34}$$

The continuity condition of the magnetic field yields:

$$\frac{\epsilon_1}{p_1}E_{x,1} + \frac{\epsilon_2}{p_2}E_{x,2} = 0. \tag{2.35}$$

We have the following solution:

$$\frac{\epsilon_1}{p_1} + \frac{\epsilon_2}{p_2} = 0. \tag{2.36}$$

Together with Eq. 2.33, Eq. 2.36 leads to the dispersion relation of:

$$\beta = \frac{\omega}{c}\sqrt{\frac{\epsilon_1\epsilon_2}{\epsilon_1 + \epsilon_2}}. \tag{2.37}$$

In order to have surface modes localized at the interface, β as a real number, the dielectric constants should satisfy the following condition:

$$\epsilon_1\epsilon_2 < 0, \epsilon_1 + \epsilon_2 > 0. \tag{2.38}$$

As an example, we consider vacuum as medium 1 and SiO_2 as medium 2. The important parameter defining the materials for SPhP is their dielectric function. The dielectric function for vacuum is $\epsilon_1 = 1$. Figure. 2.8 shows the plot of the real and imaginary parts of the dielectric function of SiO_2 [12].The relative permittivity of SiO_2 is complex and frequency-dependent.

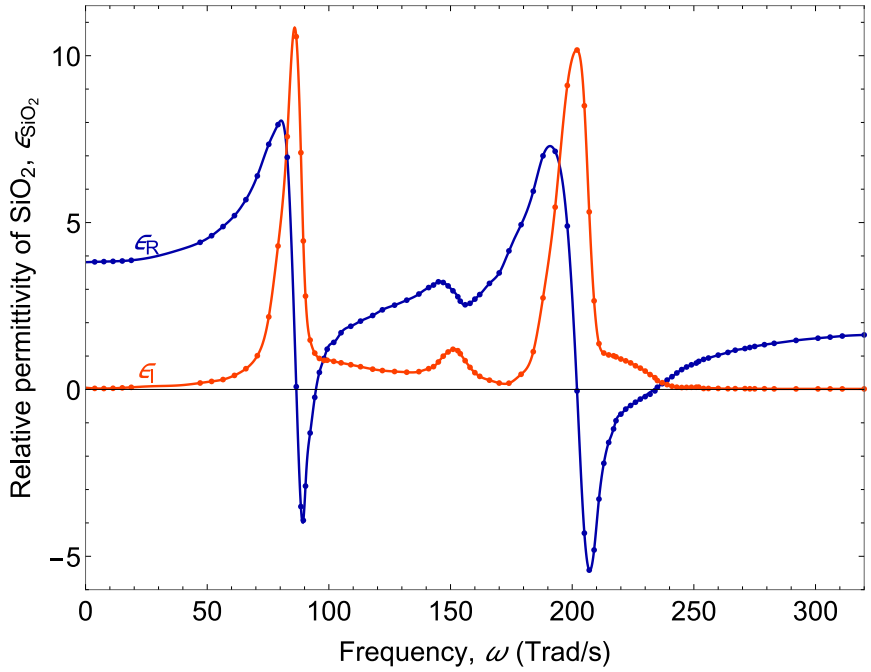

Figure2.8 Real (ϵ_R) and imaginary (ϵ_I) parts of the relative permittivity of SiO_2 reported in Ref [12].

ϵ_I has its peaks at about 87 Trad/s and 202 Trad/s which indicates that the SiO_2 absorbs significant energy from the electromagnetic field at those frequencies. On the contrary, the minimum of ϵ_I at 174 Trad/s indicates that modes can propagate for relatively large distances within the SiO_2, at this frequency without being absorbed. According to Eq. 2.37, the dispersion relation is plotted for vacuum-SiO_2 interface (Fig.2.9a).

The real part of the wave vector β_R becomes larger than the light line, meaning that the surface waves are localized at the interface (evanescent in perpendicular direction to the interface), typically at the two dips of ϵ_R at 89 Trad/s and 207 Trad/s. Therefore, those frequencies are considered as SPhP resonance frequencies. The vicinity of the minimum of ϵ_I and the main dip of ϵ_R are expected to contribute the most to the SPhP thermal transport. The imaginary part of the wave vector, β_I, also possess the important information on SPhP propagation. The mean free path of SPhPs is defined as inversely proportional to the imaginary part of the wave vector, and is called propagation length [55]:

$$\Lambda = \frac{1}{2\beta_I}. \tag{2.39}$$

The propagation length is is defined for SPhPs at the vacuum-SiO_2 interface in Fig. 2.9b.

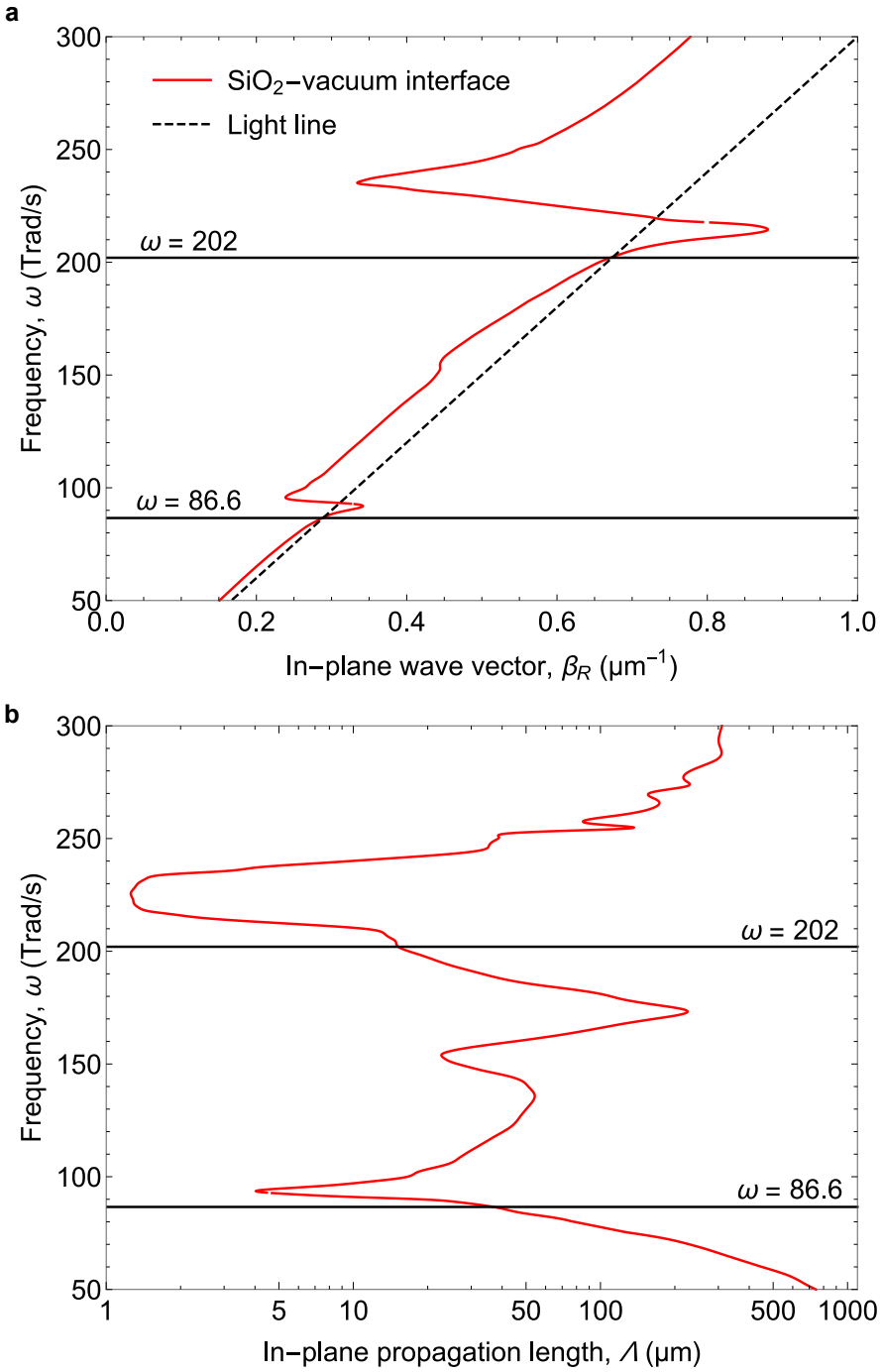

Figure2.9 **a** Dispersion relation and **b** in-plane propagation length of SPhP in SiO_2-vacuum single interface.

2.3.2 SPhPs in a film

Next, we consider the SPhP dispersion relation in a film configuration. Figure.2.10 shows the schematic of the system. A single film of thickness d is surrounded by media 1 and 3.

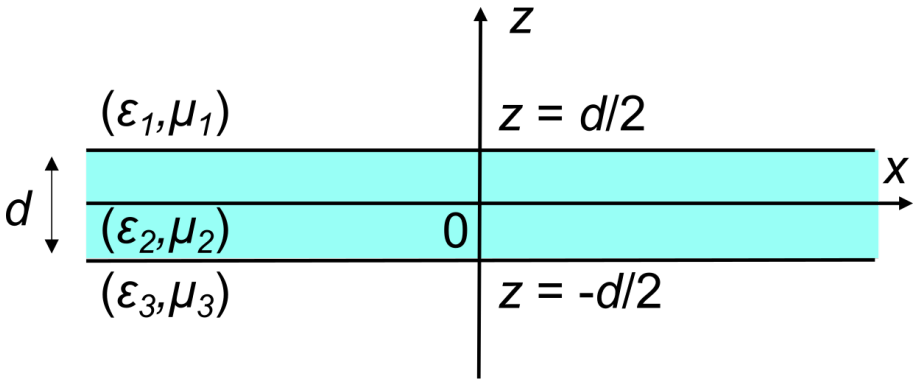

Figure2.10 Schematic of the cross-sectional view of a thin film of thickness d, surrounded by medium 1 and medium 3. (ϵ_j,μ_j) refers to dielectric function and permeability of medium j = 1 3.

Basically, Eqs. 2.30, 2.31, 2.32 can be again used to derive the dispersion relation, but with boundary conditions applied at both $z = d/2$ and $z = -d/2$. This combination yields the dispersion relation as below,

$$tanh(p_2 d) = -\frac{p_2\epsilon_2(p_1\epsilon_3 + p_3\epsilon_1)}{p_2^2\epsilon_1\epsilon_3 + p_1 p_3\epsilon_2^2}. \tag{2.40}$$

Detailed calculations can be found in [56]. When the film is surrounded by the same media, $\epsilon_1 = \epsilon_3$, Eq. 2.40 leads to two cases;

$$tanh(\frac{p_2 d}{2}) = -\frac{p_2\epsilon_1}{p_1\epsilon_2}, \tag{2.41}$$

$$tanh(\frac{p_2 d}{2}) = -\frac{p_1\epsilon_2}{p_2\epsilon_1}. \tag{2.42}$$

$$\tag{2.43}$$

Equation 2.41 is a branch which gives odd magnetic field and Eq. 2.42 is a branch of even magnetic field. Since even branch gives longer propagation length[57], we consider from now on only the even branch. When the film is thick enough, meeting $p_2 d/2 >> 1$, Eq. 2.42 can be

simplified to:

$$p_1\epsilon_2 + p_2\epsilon_1 = 0, \tag{2.44}$$

which is exactly the same as the case of the single interface. On the contrary, When the film thickness is thin enough, $p_2 d/2 << 1$, Eq. 2.42 can be then simplified to:

$$\frac{p_2 d}{2} = -\frac{p_1\epsilon_2}{p_2\epsilon_1}. \tag{2.45}$$

Again, as an example, we consider vacuum as media 1 and 2, and SiO_2 as medium 2, assuming a SiO_2 film suspended in vacuum. The dispersion relations of SPhPs in a film of different thickness of 100 *nm* and 1 μm are plotted in Fig. 2.11a. In both cases, the dispersion relation was below the light line, meaning evanescent modes, in most of the frequency range. As the thickness decreases, the curve approach closer to the light line and almost superposed. Figure. 2.11b shows the propagation length of SPhP in a SiO_2 film. The thinner the film is, the longer the propagation length since there is less material to absorb the energy, and SPhP at the top interface and the bottom interface of the film can couple strongly inside the film before decaying completely in the cross-plane direction.

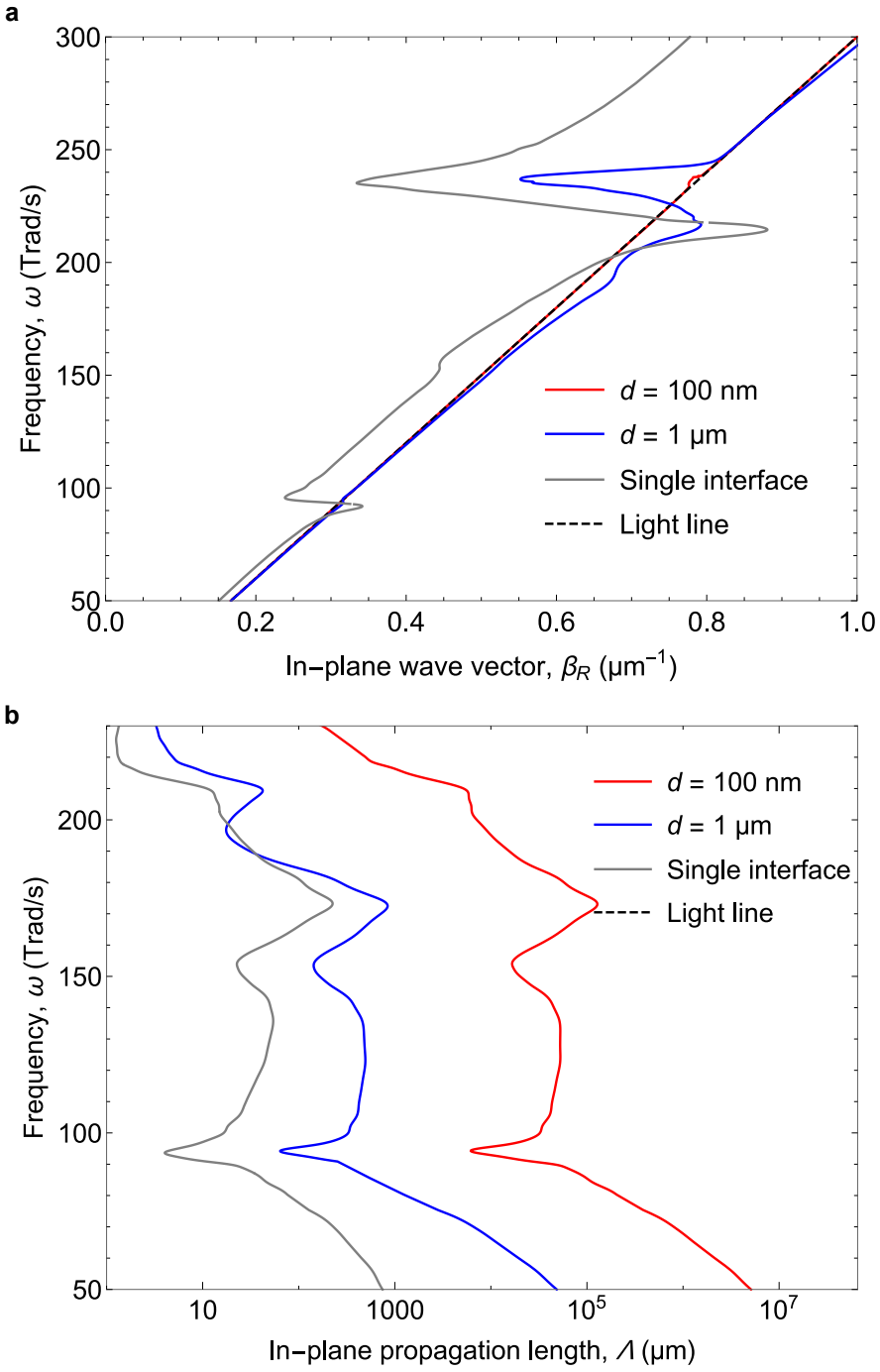

Figure2.11 **a** Dispersion relation and **b** in-plane propagation length of SPhP in a suspended SiO_2 film of 100 nm and 1 μm thickness.

2.3.3 SPhPs in a three-layer system

From now, we demonstrate the dispersion relation calculation of three-layer structure(Fig. 2.12).

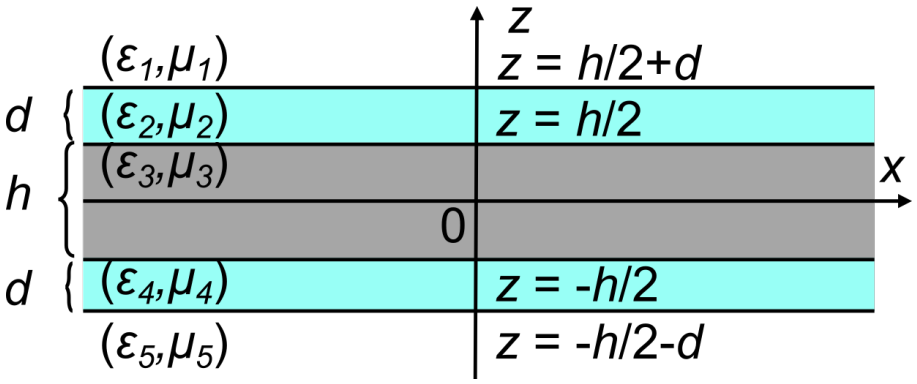

Figure2.12 Schematic of the cross-sectional view of a three-layer system. Medium 3 of thickness h, sandwiched by medium 2 thickness d, is surrounded by medium 1. (ϵ_j,μ_j) refers to dielectric function and permeability of medium j = 1 3.

Again, Eqs. 2.30, 2.31, 2.32 are used to derive the dispersion relation. The continuity of fields as boundary conditions were applied at $z = -d - h/2, -h/2, h/2$ and $d + h/2$. This yields the dispersion relation as:

$$tanh(p_3 h) = -\frac{2S_{23}[S_{12} + tanh(p_2 d)][S_{12} tanh(p_2 d) + 1]}{[S_{12} + tanh(p_2 d)]^2 S_{23}^2 + [S_{12} tanh(p_2 d) + 1]^2}, \tag{2.46}$$

where $S_{mn} = p_m \epsilon_n / \epsilon_m p_n$.

2.3.4 SPhP in a SiO_2/Si/SiO_2 three-layer system

In the following discussion, we consider SiO_2 as medium 2, Si as medium 3, and vacuum as medium 1. Both SiO_2 and Si are common materials in semiconductor industries and compatible with existing fabrication technologies. We particularly consider the case where the Si layer is relatively thick in micrometer range, so that the configuration can guarantee mechanical stability compared to suspended nano-films. SiO_2 acts as the polariton active media while Si is treated as non-absorptive material with the dielectric function of $\epsilon_3 = 11.7$. The dispersion relation of SiO_2-Si-SiO_2 three-layer system is plotted in Fig. 2.13a. The thickness of SiO_2 and Si are set to $d = 1\mu$m and $h = 10\mu$m respectively.

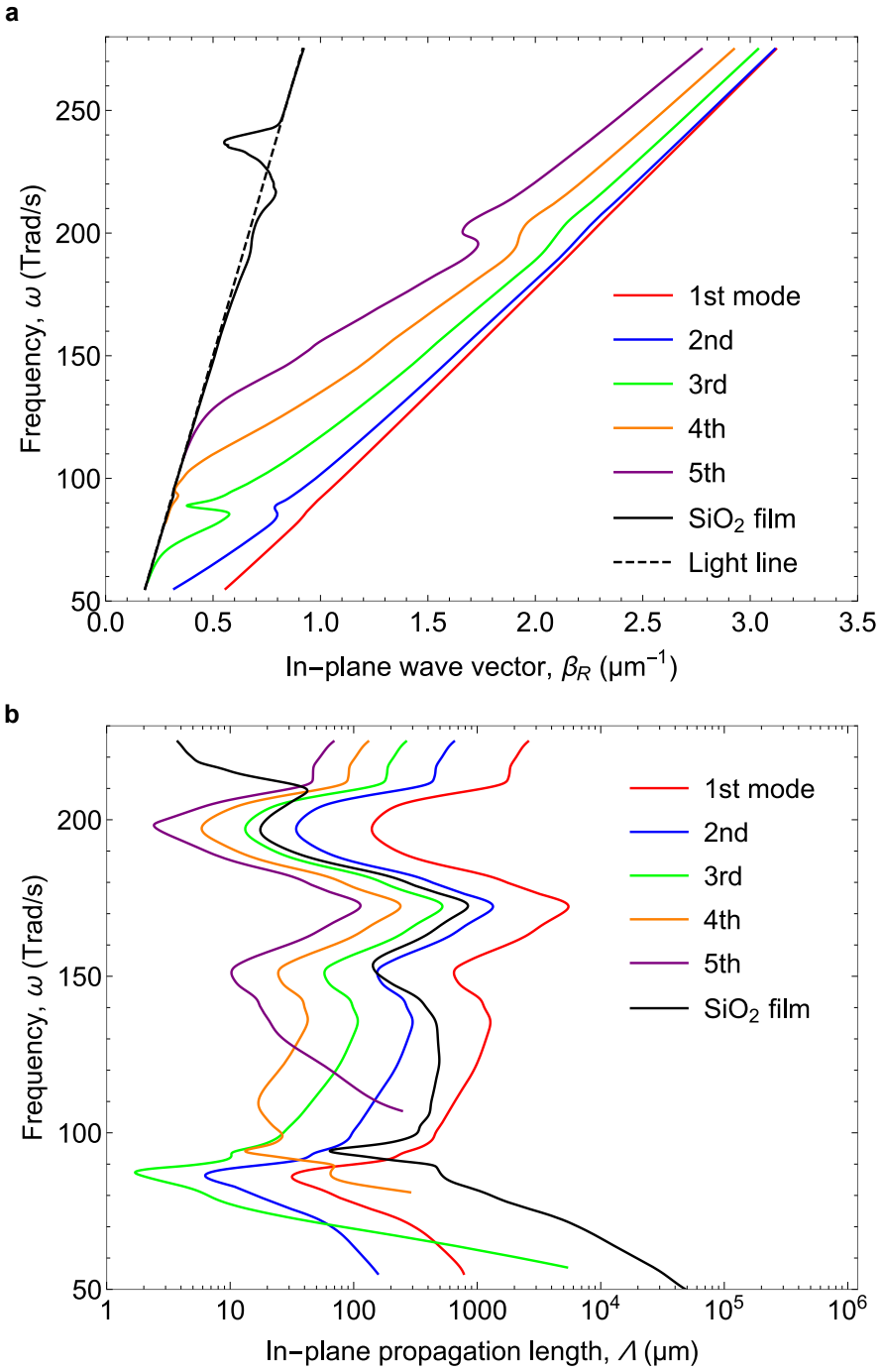

Figure2.13 **a** Dispersion relation and **b** in-plane propagation length of SPhP in a SiO_2/Si/SiO_2 three-layer system. SiO_2 thickness d =1 μm and Si thickness h =10 μm.

The dispersion relation has multiple branches. This is due to the term, $tanh(p_3 h)$ in Eq. 2.46. Since h is realtively thick, we cannot apply the simplifications and the equation does not reduce to the linear relation, thus giving several solution or branches. The propagation length of each branch are plotted in Figure. 2.13b Each branch has different propagation length, and 1st branch shows the longest propagation length, even longer than that of a suspended SiO_2 film case in most of the frequency range.

2.4 Numerical simulations of SPhPs in SiO_2/Si structures

2.4.1 Computational cell

The numerical simulations were computed using Finite Element Method (FEM) simulation software named "COMSOL". It solves the Maxwell's equations in each mesh, taking into account certain boundary conditions. The advantage of using the simulation is that one can derive the wave vectors of electromagnetic waves in the system as a result of Maxwell's equations at each point, therefore we applied it to cross-check the validity of the analytical calculation on the dispersion relation for three-layer systems. Figure.2.14a shows the computational cell that we developed. It is a basic two-dimensional model with the cross-section of SiO_2-Si-SiO_2 three-layer system surrounded by air. The thickness of each layer is 1 μm and 10 μm for SiO_2 and Si, respectively. The boundary of the computational cell was set to PML (Perfectly matched layer) to absorb the incident electromagnetic waves encountering the boundaries. Input wave of a certain frequency was injected from the side of the top SiO_2 layer. Another input was the dielectric function of each material. The dielectric function of air and Si were ϵ_{air}=1 and ϵ_{Si}=11.7, and the dielectric function of Figure. 2.8 was applied for SiO_2[12].

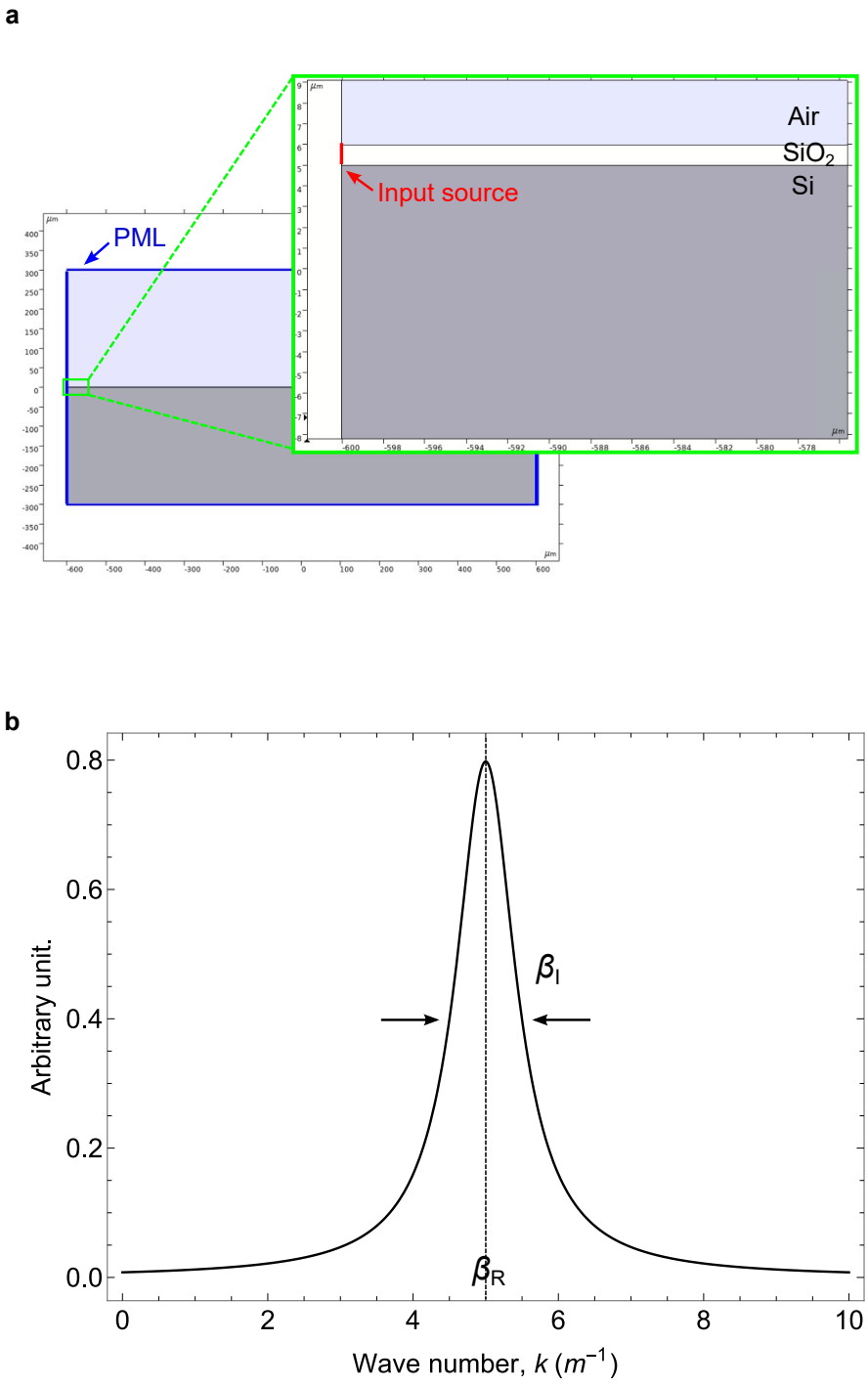

Figure2.14 **a** Computational cell for FEM simulations on SiO_2/Si/SiO_2 3-layer system. SiO_2 is of 1 μm and Si of 10 μm thickness. Boundary condition is set at perfectly matched layer (PML). Electromagnetic waves of certain frequencies were input from the side of the top SiO_2 layer. **b** Lorentzian function of arbitrary unit.

2.4.2 Derivation of wave vectors

The wave vectors were derived by Fourier transform of the electric fields. We obtained the profile of electric field along the interface between SiO_2 on top and air, which propagates and decay in the in-plane direction. Such field typically has the plane wave term of $e^{i\beta_R x - \beta_I x}$. Fourier transform of this field is:

$$\mathcal{F}[e^{i\beta_R x - \beta_I x}] = \frac{1}{\sqrt{2\pi}} \frac{i}{k + i\beta_I + \beta_R}. \tag{2.47}$$

The real part is:

$$\mathrm{Re}(\mathcal{F}[e^{i\beta_R x - \beta_I x}]) = \frac{1}{\sqrt{2\pi}} \frac{\beta_I}{(k - \beta_R)^2 + \beta_I^2}. \tag{2.48}$$

Equation. 2.48 is typically called the Lorentzian function. The wave number at the peak corresponds to the real part of the wave vector, while the full width at half maximum corresponds to the imaginary part of the wave vector(Fig.2.14b). The Fourier transform of the electric field obtained at the interface was fitted by the Lorentzian function to derive both β_R and β_I. β_R gives the dispersion relation and β_I gives the propagation length for each frequency.

2.4.3 Comparison of the wave vectors obtained from the analytical calculation and the numerical simulation

Figure. 2.15a shows the dispersion relation obtained for SiO_2(1 μm)-Si(10 μm)-SiO_2(1 μm) by both analytical calculation and numerical simulation. The solid lines refer to the analytical solutions, while the dots show what we obtained by numerical simulation. The numerical simulation also showed several branches, and both results met a good agreement. Figure.2.15b shows the propagation length obtained by both methods. Again, both results met a good agreement for each branch. The propagation length longer than 1800 μm were not fited properly since the computational cell has length limitation at 1800 μm. These results demonstrate the validity of our analytical calculations of a SiO_2/Si/SiO_2 three-layer system.

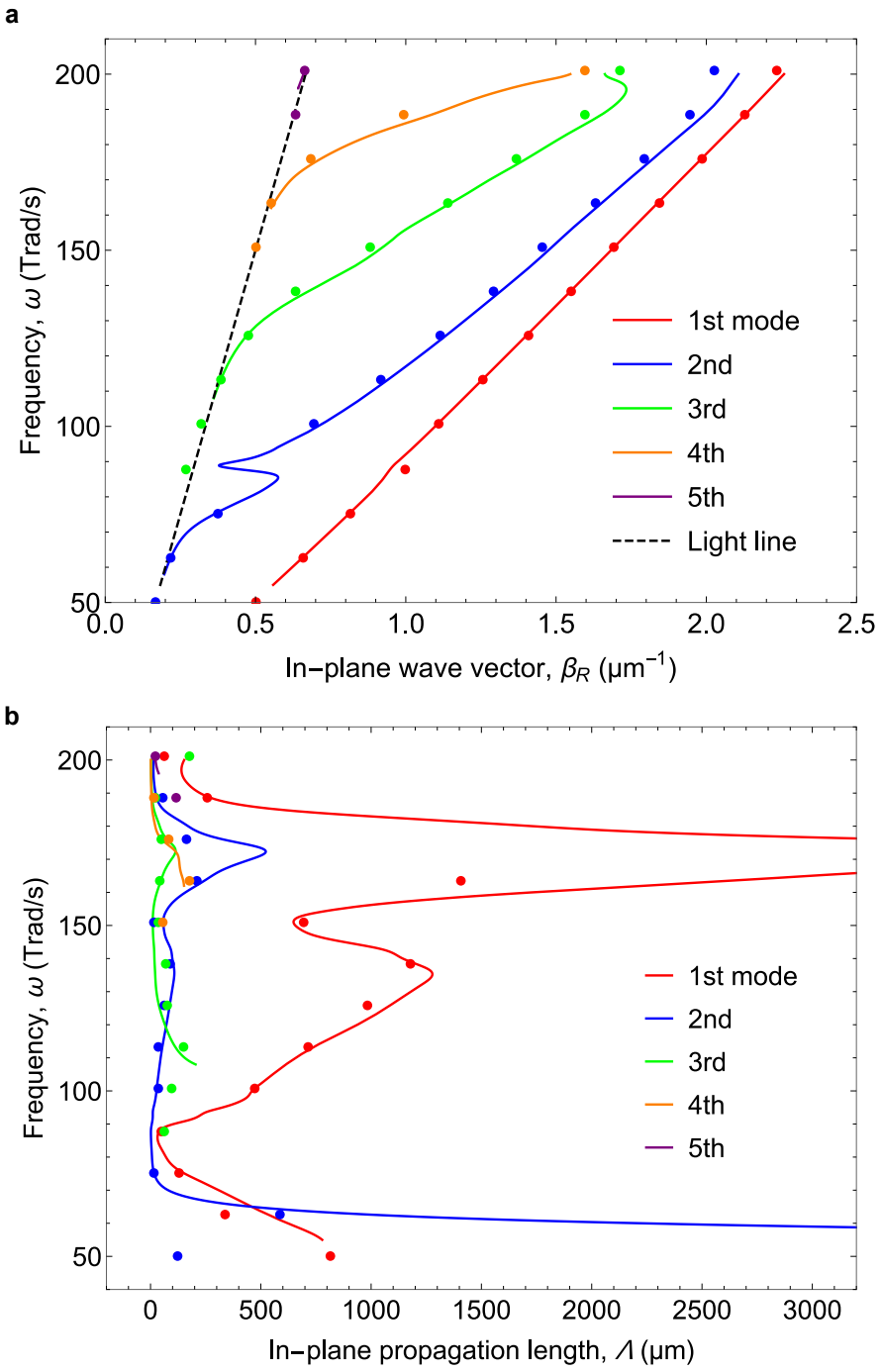

Figure2.15 **a** Dispersion relation and **b** in-plane propagation length of SPhP in three-layer system with SiO_2 of 1 μm and Si of 10 μm thickness. Solid lines correspond to analytical calculation results, while dots correspond to results gained by numerical simulations.

2.5 SPhP thermal conductivity

2.5.1 SPhP thermal conductivity of a SiO_2 film

In this section, SPhP thermal conductivity k of a SiO_2 film is calculated according to Eq. 2.1. In Fig.2.16a, the thermal conductivity of SiO_2 films of different thicknesses are plotted dependent on temperature. As we saw in Fig.2.11b, the propagation length of a film increases by orders of magnitude as the film thickness decreases due to less absorption inside the material. Therefore, the in-plane thermal conductivity of SPhP which is dependent on the propagation length, also increases dramatically along with the thickness reduction. For the thickness of 1 μm, k ~0.4 mW/m.K even at 700 K and is negligible compared to the phonon contribution, while for the thickness of 50 nm, k is already comparable with the phonon contribution at 300 K. The temperature dependency is shown as well in the figure. In any thickness case, the thermal conductivity is higher at higher temperature.

2.5.2 SPhP thermal conductivity of a three-layer system

For the SiO_2-Si-SiO_2 three-layer system, the thermal conductivity has contributions from each branch. Figure. 2.16b shows the thermal conductivity of each branch and sum of them as "Total" thermal conductivity for the SiO_2(1 μm)/Si(10 μm)/SiO_2 three-layer system. The 1st branch with the longest propagation length contributes the most to the total thermal conductivity at $\sim$ 75%. The higher the order of branch, the lower the contribution to the total thermal conductivity, $\sim$ 16%, $\sim$ 5.8% for 2nd and 3rd branch respectively.

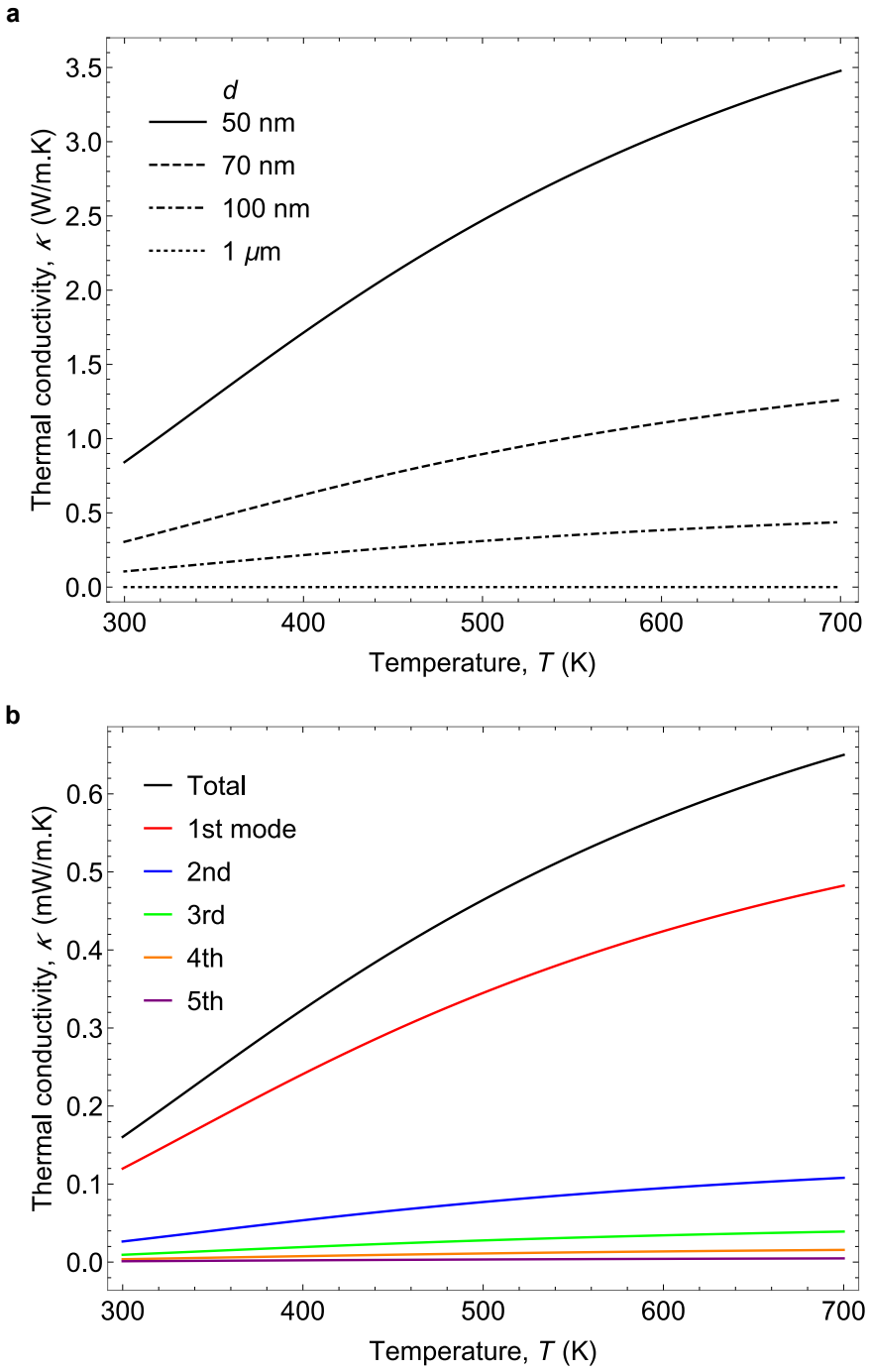

Figure2.16 **a** SPhP thermal conductivity of SiO_2 film of different thicknesses d against temperature. **b** SPhP thermal conductivity of each branch for SiO_2(1 μm)/Si(10 μm)/SiO_2 three-layer system against temperature. Total thermal conductivity corresponds to the sum of the thermal conductivity of each branch.

2.6 SiO_2 thickness dependence of SPhP thermal conductivity of a 3-layer system

We investigated the SiO_2 thickness dependence of SPhP thermal conductivity of SiO_2-Si-SiO_2 three-layer system. Regarding the effect of the film thickness reduction for a single film case, the SPhP thermal conductivity enhancement is expected by reducing the thickness of polariton active media, SiO_2 in this three-layer system case. Figure. 2.17a shows the SPhP thermal conductivity of three-layer system of different SiO_2 thickness, while the Si thickness is fixed at 10 μm. As expected, thinner the SiO_2 layer is, higher the SPhP thermal conductivity is. In Fig. 2.17b, we compared the SiO_2 thickness dependence of the SPhP thermal conductance for a SiO_2 film and SiO_2-Si-SiO_2 three-layer system cases. The thermal conductance was defined as:

$$G = \frac{W}{4\pi L}\int_{\omega_L}^{\omega_H} \hbar\omega\Lambda\beta_R\frac{\partial f_0}{\partial T}d\omega, \tag{2.49}$$

with W and L being the system width and length, respectively. The impact of SiO_2 thickness reduction is weaker on the three-layer system since the total thickness of the system is much larger than SiO_2 thickness. We found that for $SiO_2 > 150nm$, the SPhP thermal conductnace is higher for the three-layer system compared to that of a film. It indicates that a micrometric structure can achieve comparable or even higher thermal conductance than a film case, and this is technically interesting finding since it had been always believed that thickness of the system should be thinner to yield high thermal conductance, although such thin suspended film is mechanically unstable.

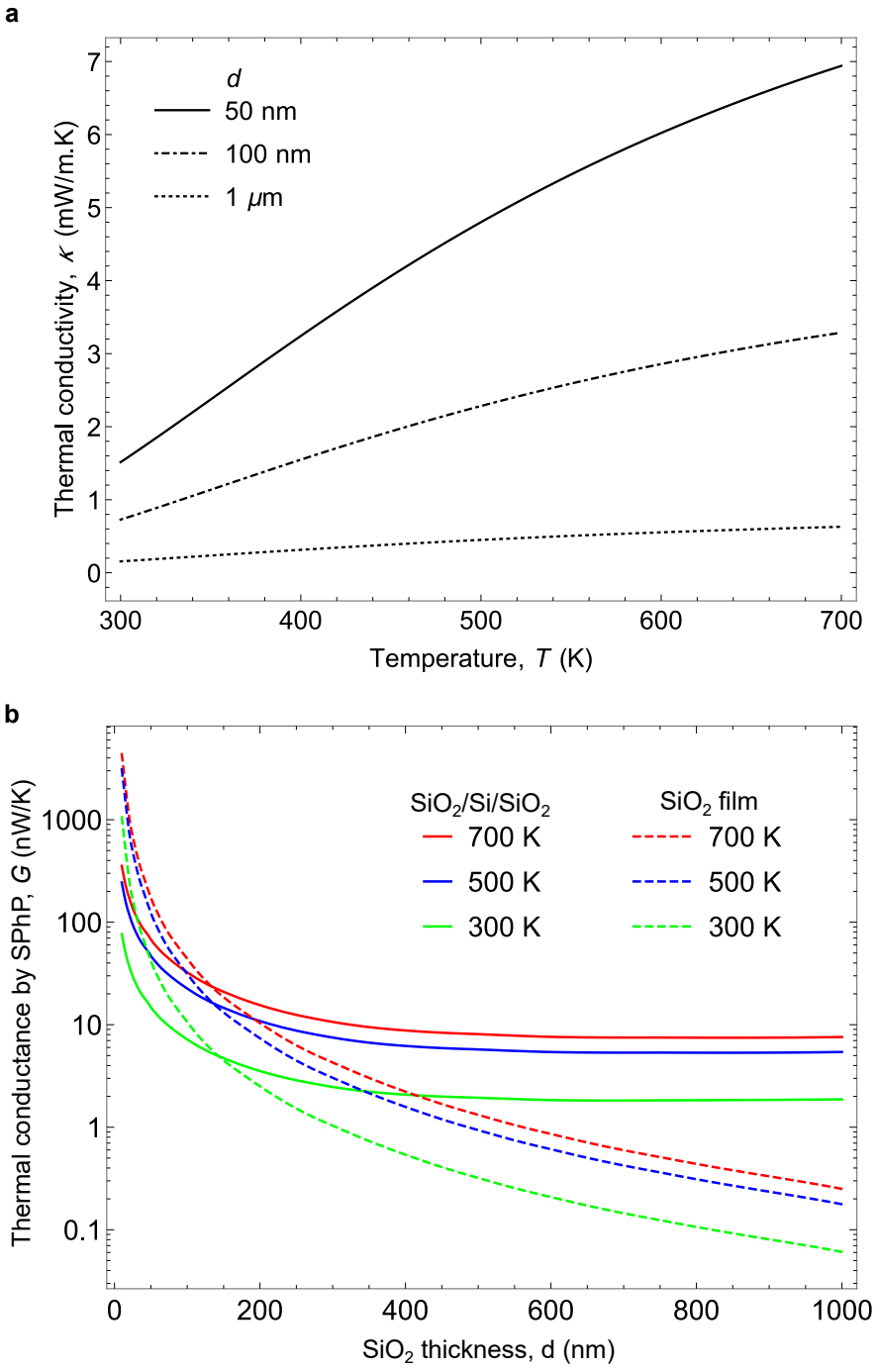

Figure2.17 **a** SPhP thermal conductivity of $SiO_2/SiSiO_2$ three-layer system for different SiO_2 thickness against temperature. **b** SiO_2 thickness dependence on SPhP thermal conductance of a SiO_2 film and $SiO_2/Si/SiO_2$ three-layer system.[13]

2.7 Si thickness dependence of SPhP thermal conductivity of a three-layer system

In this section, we report the Si thickness dependence of SPhP thermal conductivity in SiO_2-Si-SiO_2 three-layer systems. Our hypothesis was that when the thickness of Si is small, especially smaller than the typical wavelength of SPhP, the coupling between the SPhP at the top interface of Si and the SPhP at the bottom interface of Si becomes stronger, providing the longer propagation lengths therefore higher thermal conductivity. Figure. 2.18 shows the thermal conductivity of the three-layer systems with different Si thickness h. SiO_2 thickness was fixed at 100 nm. Contrary to our hypothesis, the system with thicker Si showed higher thermal conductivity. To investigate deeper, the dispersion relation is plotted for different Si thickness in Fig. 2.19a. Only the first branch is chosen for comparing its largest contribution to the thermal conductivity. For thickness thinner that the typical wavelength for SPhP, ~10 μm, the dispersion relation is more along the light line in vacuum especially at lower frequencies, and start to separate and approach the light line in Si, as the thickness becomes larger, especially for higher frequency range.

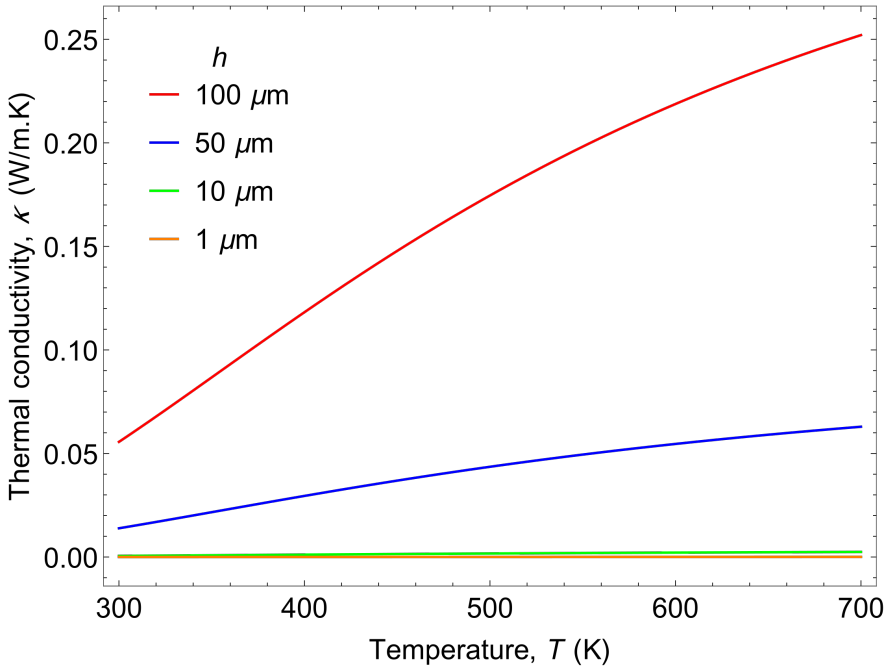

Figure2.18 Dependence of SPhP thermal conductivity to Si thickness h in SiO_2/Si/SiO_2 three-layer system. SiO_2 thickness is fixed at 100 nm.

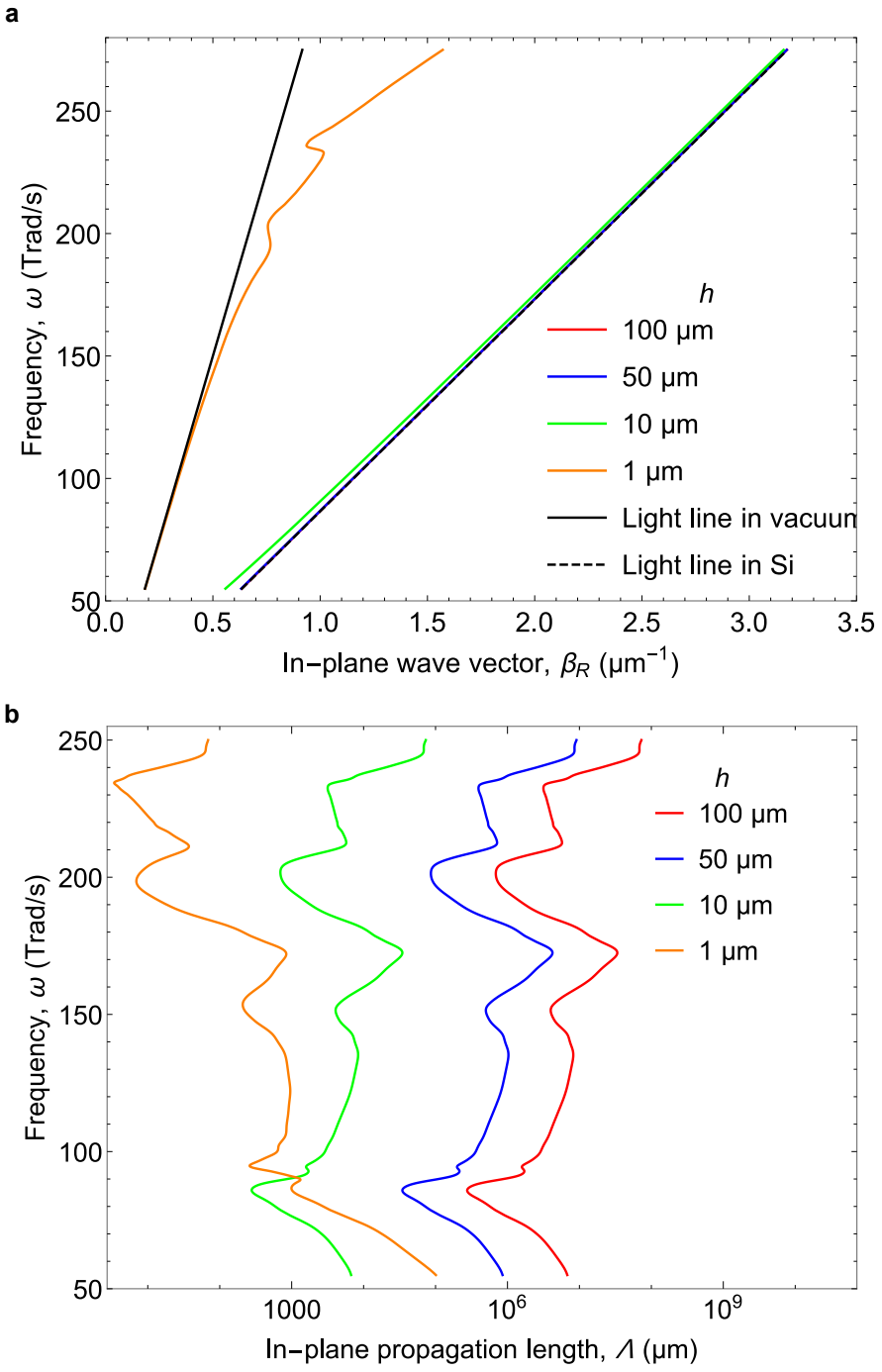

Figure2.19 Si thickness h dependence of **a** dispersion relation and **b** SPhP propagation length in SiO_2/Si/SiO_2 three-layer systems. SiO_2 thickness is fixed at 100 nm.

For thickness larger than 10 μm the dispersion curve is along the light line in Si. The red line for h =100 μm and the blue line for h =50 μm are superposed on the light line in Si. The SPhP propagation lengths for different Si thicknesses of three-layer systems is plotted in Fig.2.19b. Again, SiO_2 is fixed at 100 nm and the 1st branch is only taken into account. The thicker Si shows the longer propagation length for most of the frequency range which leads to higher thermal conductivity.

2.7.1 Oblique propagative waves inside Si

For further understanding of SPhP propagation inside the three-layer system for thick Si, we used FEM (Finite Element Method) simulation software named "COMSOL" to visualize the electric field. With the same computational cell as shown in Fig.2.14a, we set the Si thickness as 100 μm. The wave with frequency of 172 Trad/s was input on the sidewall of top SiO_2 of 1 μm thickness. Figure. 2.20a shows the y component of electric field propagating in the positive direction of the x-axis. It indicates that the electromagnetic wave input is partially propagating inside Si with an oblique angle. As this oblique wave reach the interface between Si and the bottom SiO_2, it partially excites in-plane waves at the interface, the rest of it is reflected. The reflected oblique waves reach the interface of Si and the top SiO_2 and activates the in-plane surface waves while being reflected partially again, and keep propagating in that manner.

Those oblique propagative waves result from the difference of refractive index between SiO_2 and Si. According to the Snell's law, the incident light entering from the media with the refractive index n_1, into the media with the refractive index n_2 at an angle of θ_1, is refracted by an angle of θ_2 (Fig.2.20b) and this refracted angle of θ_2 is defined as;

$$\theta_2 = \arcsin(\frac{n_1}{n_2}\sin\theta_1). \tag{2.50}$$

As the SPhP propagates along the interface, the incident angle is 90° which gives the refracted angle of θ_2 as $\theta_2 \sim 34°$ for the frequency of 172 Trad/s. We assumed that this oblique propagative waves returned to the interface excite surface waves and therefore provide longer propagation length since oblique waves do not lose energy while traveling in Si, a nonlossy material. In order to prove the contribution of oblique propagative waves, we investigated several different configurations; SiO_2 layer on a Si substrate (infinite thickness), SiO_2 layer on a Si film with Si thickness smaller than the wavelength of the oblique propagative waves.

a

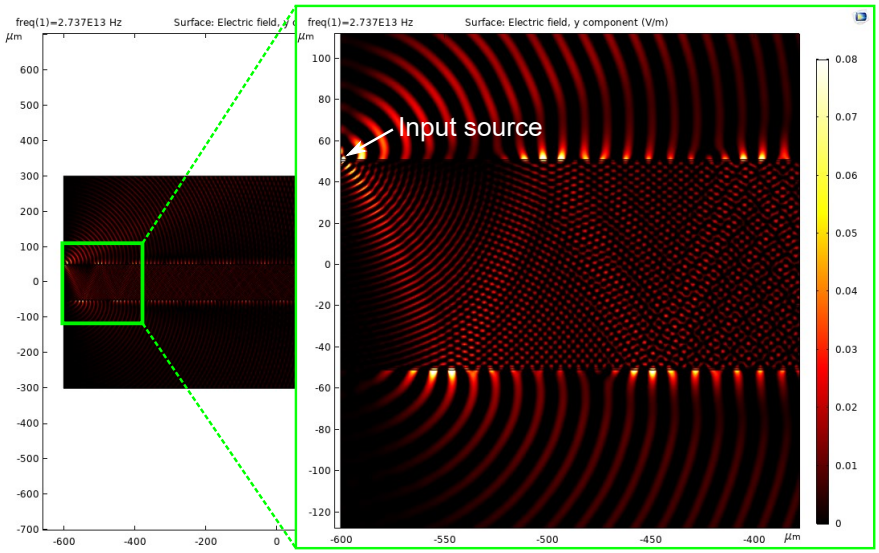

b

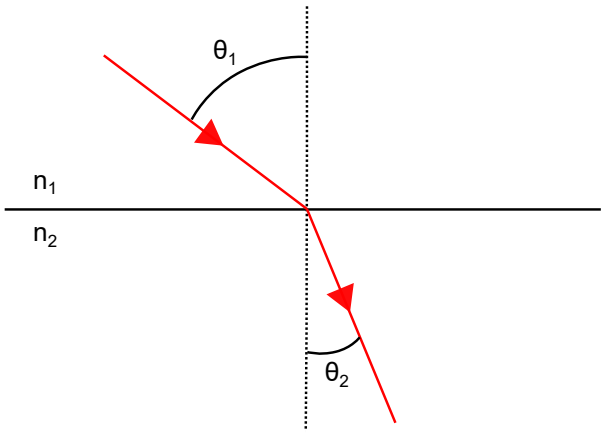

Figure2.20 **a** Electric field distribution in SiO_2 (1μm)/Si (100μm)/SiO_2 (1μm) three-layer system. **b** Schematic of the Snell's law

2.7.2 SiO_2 layer on a Si substrate

We conducted an analytical calculation of the dispersion relation and numerical simulations on the configuration of SiO_2 film on a Si bulk substrate. The computational cell is shown in Fig. 2.21a. SiO_2 layer of 1 μm thickness is placed on top of Si with infinite thickness. As shown in Fig.2.21b, The oblique propagative waves propagates into deeper Si and are not reflected back to the interface between SiO_2 layer and Si substrate to excite again surface waves.

Figures 2.22a and b are the dispersion relation and the propagation length of SPhP in the same configuration respectively, obtained by both analytical calculation and numerical simulation. There is only one branch for this configuration and propagation length is always less than 1 mm.

2.7.3 SiO_2 layer on a Si film

Another configuration is SiO_2 layer on a Si film thin enough to prevent the existence of oblique propagating waves. For frequencies in the range of 50 Trad/s $\sim$ 250 Trad/s where the SiO_2 permittivity has resonances, wavelengths in Si are in the range of 2.2 μm $\sim$ 10.9 μm. The wavelength of 2.2 μm gives the refractive angle of 14.6°. When the Si film is thinner than 1 μm, with the angle above, the oblique length is smaller than half of the wavelength of 2.2 μm, therefore no oblique propagative waves can exist inside Si. Figure.2.23a presents the computational cell of numerical simulations for the corresponding configuration. As seen in the electric field distribution shown in Fig. 2.23b, the oblique propagation waves do not exist inside Si and it works more like a waveguide.

Dispersion relation and propagation length of SPhP in the configuration, obtained by both analytical calculation and numerical simulation are plotted in Figs. 2.24a and b respectively. Again, the dispersion relation has only one branch, since the dispersion relation can be simplified to a linear relation for a thin enough Si. The propagation length at this frequency range is mostly below 1 mm and shorter than the case in which Si is thicker to accommodate oblique propagating waves.

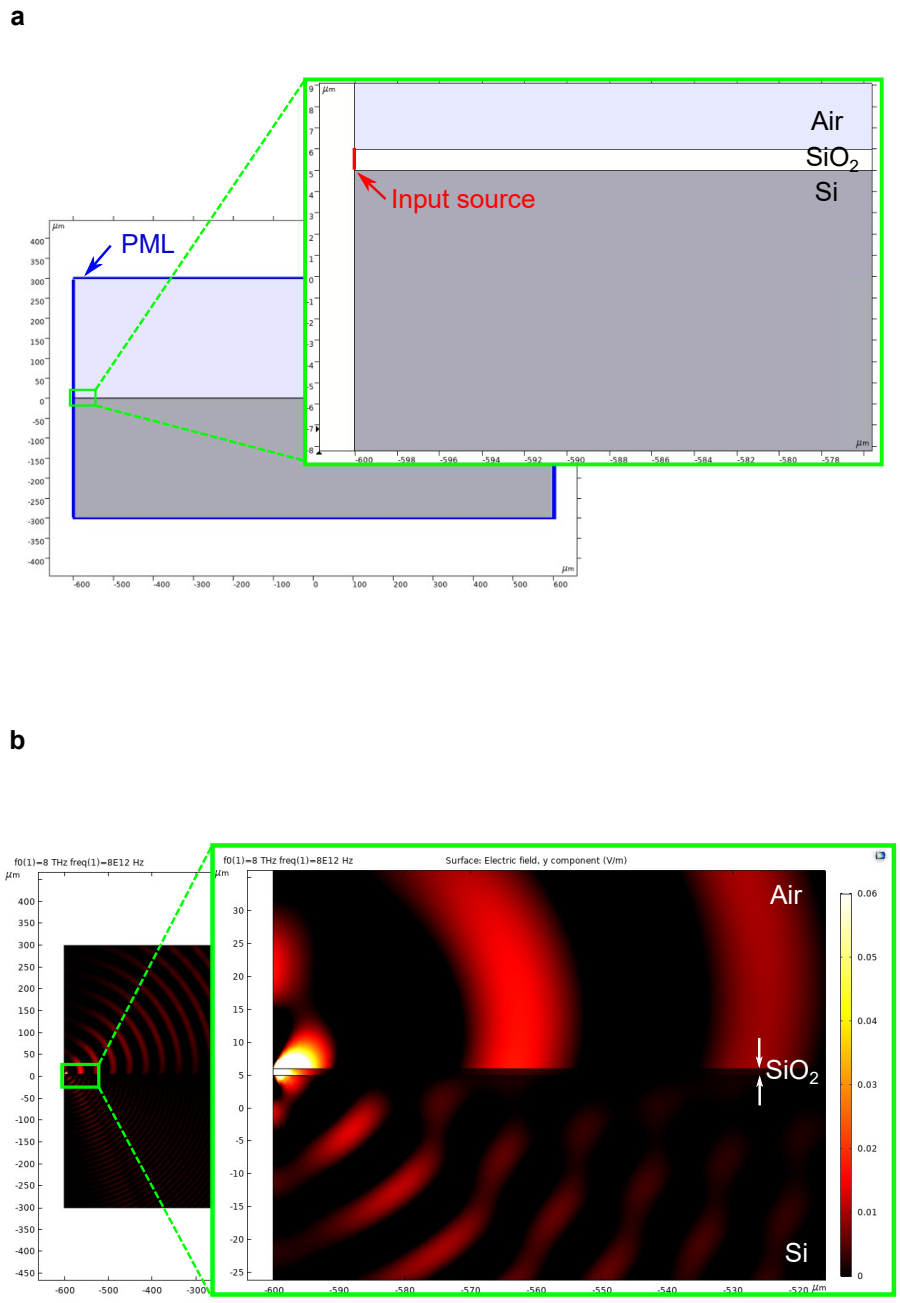

Figure2.21 **a** Computational cell for FEM simulations of a SiO_2 layer on a Si substrate. SiO_2 is of 1 μm and Si of infinite thickness. Boundary condition is set at perfectly matched layer (PML). Electromagnetic waves of certain frequencies were introduced from the side of the top SiO_2 layer. **b** Electric field distribution in SiO_2 (1 μm)/ Si substrate structure.

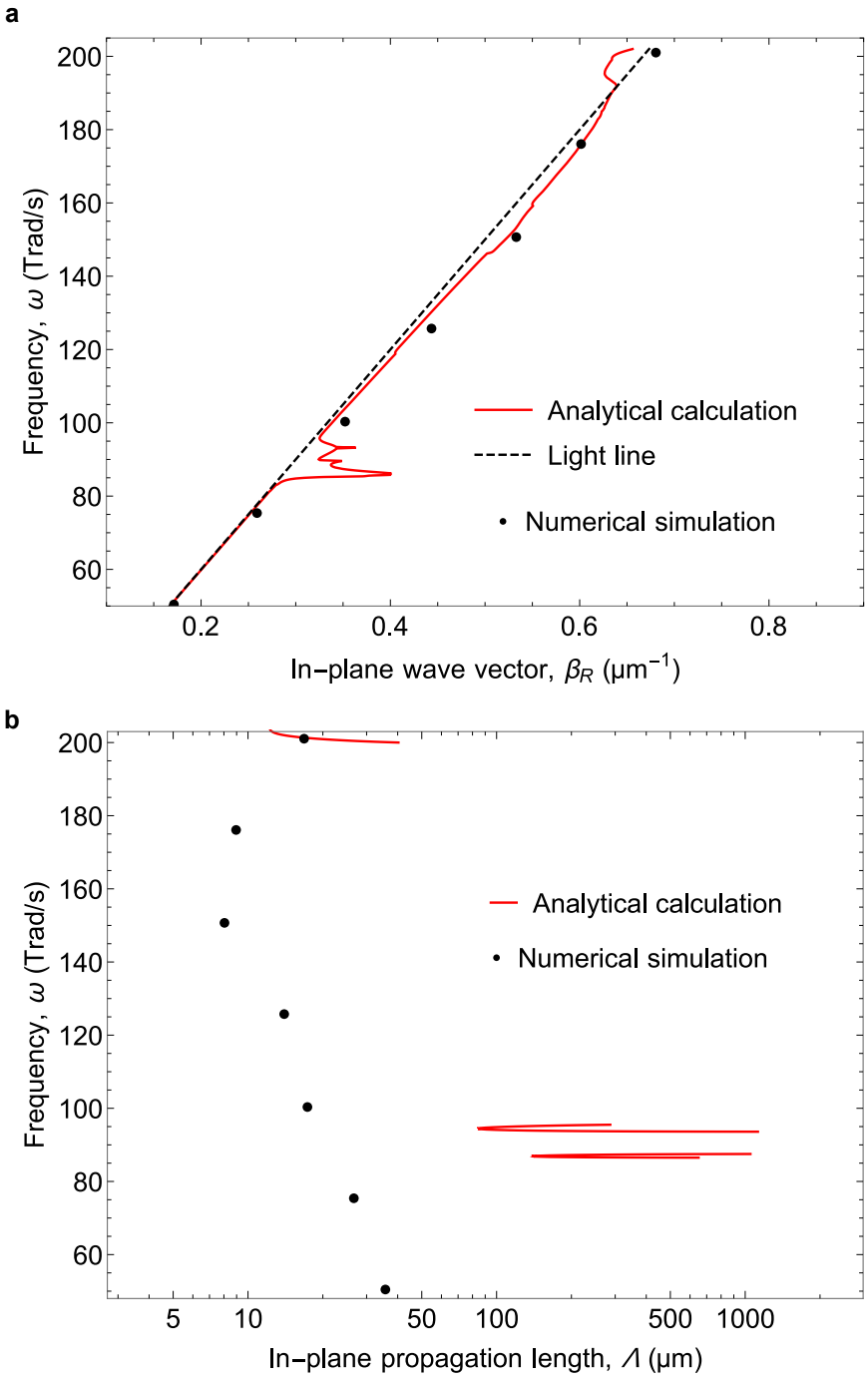

Figure2.22 **a** Dispersion relation and **b** in-plane propagation length of SPhP in SiO_2 (1 μm)/Si substrate configuration. The red solid line corresponds to the solutions from the analytical calculation, while black dots correspond to numerical calculation results.

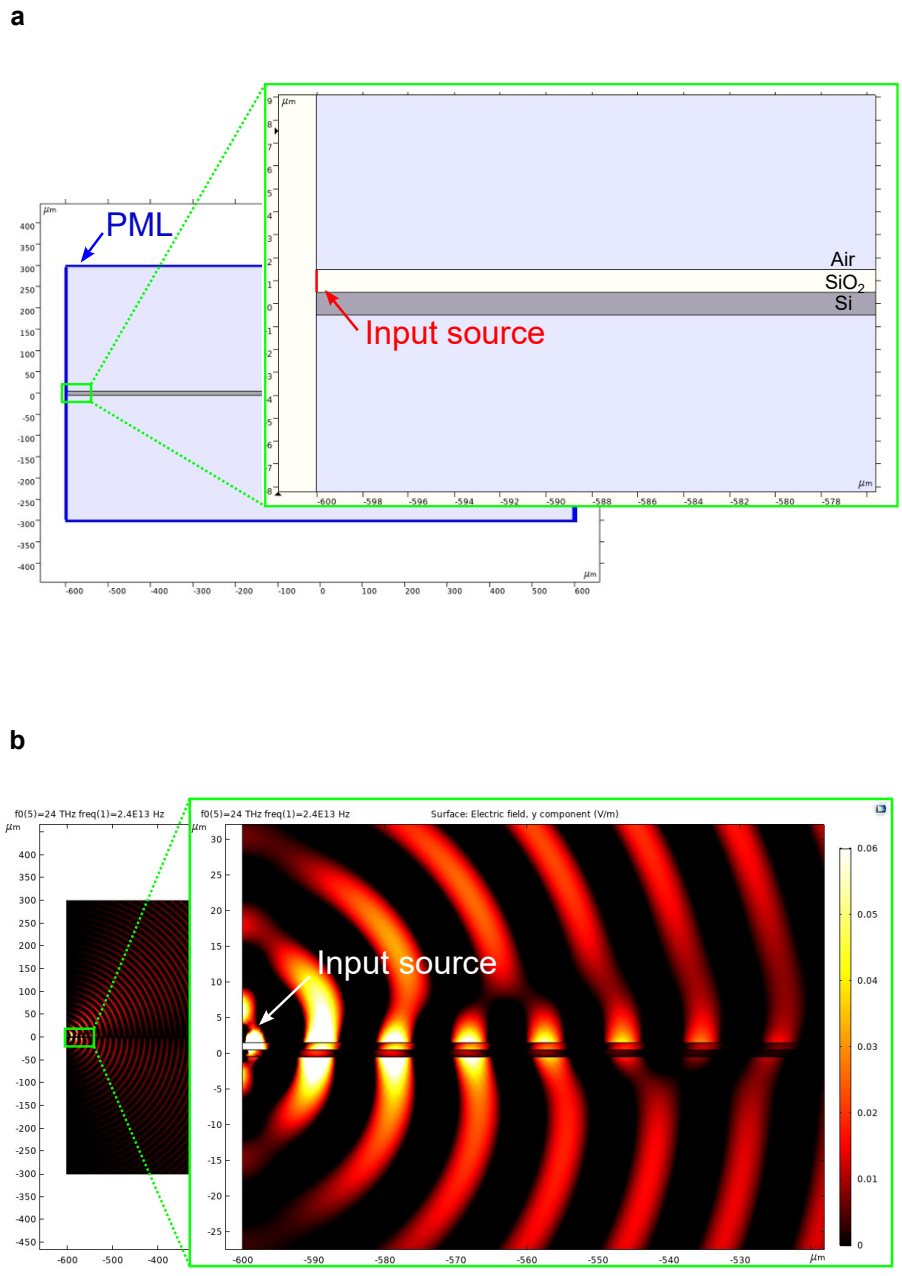

Figure2.23 **a** Computational cell for FEM simulations on SiO_2 layer on a Si film. SiO_2 and Si are of 1 μm thickness. Boundary condition is set at perfectly matched layer (PML). Electromagnetic waves of certain frequencies were introduced from the side of the top SiO_2 layer. **b** Electric field distribution in SiO_2 (1μm)/Si film (1μm).

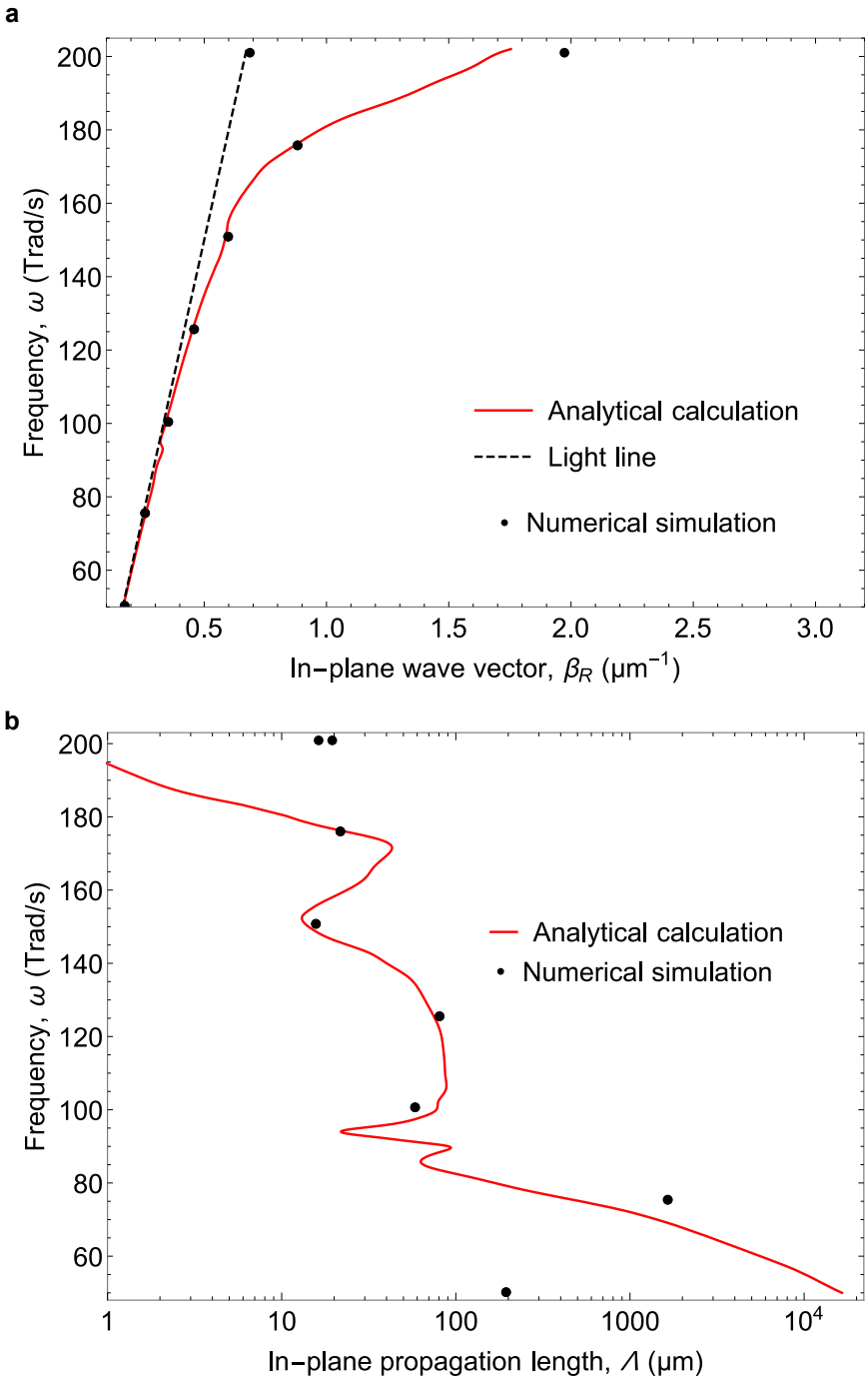

Figure2.24 **a** Dispersion relation and **b** in-plane propagation length of SPhP in SiO_2 (1 μm)/Si film (1 μm) configuration. The red solid line corresponds to the solutions from the analytical calculation, while black dots correspond to numerical calculation results.

2.7.4 Further scan of the Si thickness

We calculated the SPhP thermal conductivity for wider range of Si thickness in order to fully understand the Si thickness dependence. For thinner Si, there are two regimes; The regime in which the evanescent coupling is predominant and the regime in which the oblique propagative waves are predominant. Figure. 2.25 is a plot of thermal conductivity for Si thinner than 2 μm.

When Si thickness is thicker than 1 μm and capable of accommodate the oblique propagative waves, this contribution is predominant. Therefore the SPhP thermal conductivity reduces as the Si thickness is decreased. However, for thinner Si in which the oblique propagative waves do not exist, the thermal conductivity is enhanced as the Si thickness is decreased. This is due to the stronger coupling of evanescent waves at the top interface of Si and the bottom interface of Si.

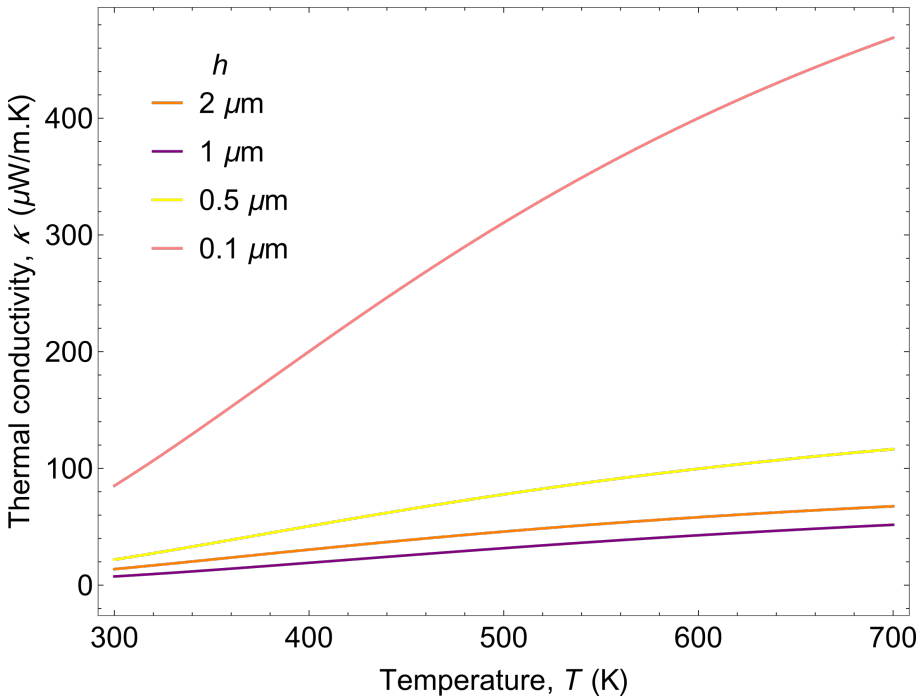

Figure2.25 Thermal conductivity due to SPhP for SiO_2/Si/SiO_2 three-layer systems depending on temperature. SiO_2 thickness is 100 nm.

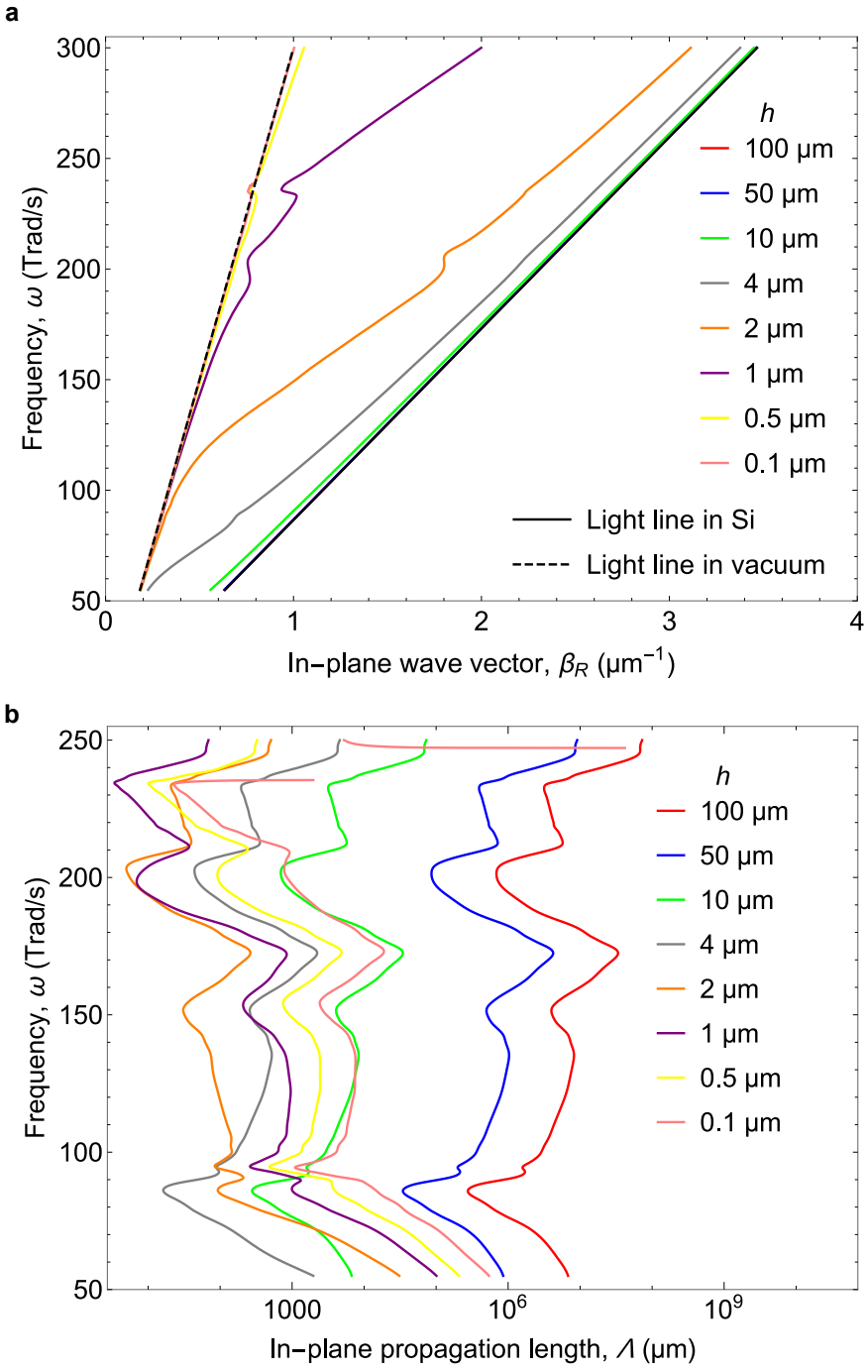

Figure2.26 **a** Dispersion relation and **b** in-plane propagation length of SPhP for SiO_2/Si/SiO_2 three-layer systems with various Si thickness. SiO_2 thickness is 100 nm.

Figure. 2.26a shows the dispersion relation for various Si thickness. The light line in Si, the $h = 100$ μm case, and the $h = 50$ μm case are superimposed. When the Si is thinner than 1 μm, the curve is more along the light line in vacuum and similar to a single film case. As the Si thickness becomes thicker, or the wavelength in Si becomes shorter compared to the thickness, the dispersion curve starts to depart from along the light line in vacuum and approach the light line in Si. This is the indication of the emergence of the oblique propagative waves inside Si. Figure. 2.26b shows the propagation length of each case. The case of $h = 0.1$ μm has propagation length as long as the case of $h = 10$ μm due to the strong evanescent coupling. We plotted the in-plane propagation length and the cross-plane decay length inside Si, for the first and the second branches, in Fig.2.27a and Fig.2.27b respectively. Both the in-plane propagation length and cross-plane decay length decreases as the Si thickness is reduced from 10 μm. However, the propagation and the decay lengths start to increase once the Si thickness is less than ~ 1 μm (~ 2 μm for the second branch). This is typically the half of the wavelength inside Si. When the Si thickness is smaller than half of the wavelength, the evanescent coupling becomes predominant. The smaller the Si thickness is, the stronger the evanescent coupling is, thus, the in-plane propagation length and the cross-plane decay length becomes longer for thinner Si. The minimum peak in the in-plane propagation length causes a minimum peak on the in-plane thermal conductivity as well. Figure 2.28 shows the sum of thermal conductivity given by the first and the second branches for different Si thicknesses.

Despite all the discussion above, it is unlikely that the thicker the Si, the higher the SPhP thermal conductivity for any semi-infinite thickness of Si. We scanned the thermal conductivity for even thicker Si and found a peak at Si thickness $h = 140$ μm (Fig. 2.29). The reduction of thermal conductivity for Si thicker than 140 μm is possibly due to decoupling of SPhPs at the top and the bottom interface.

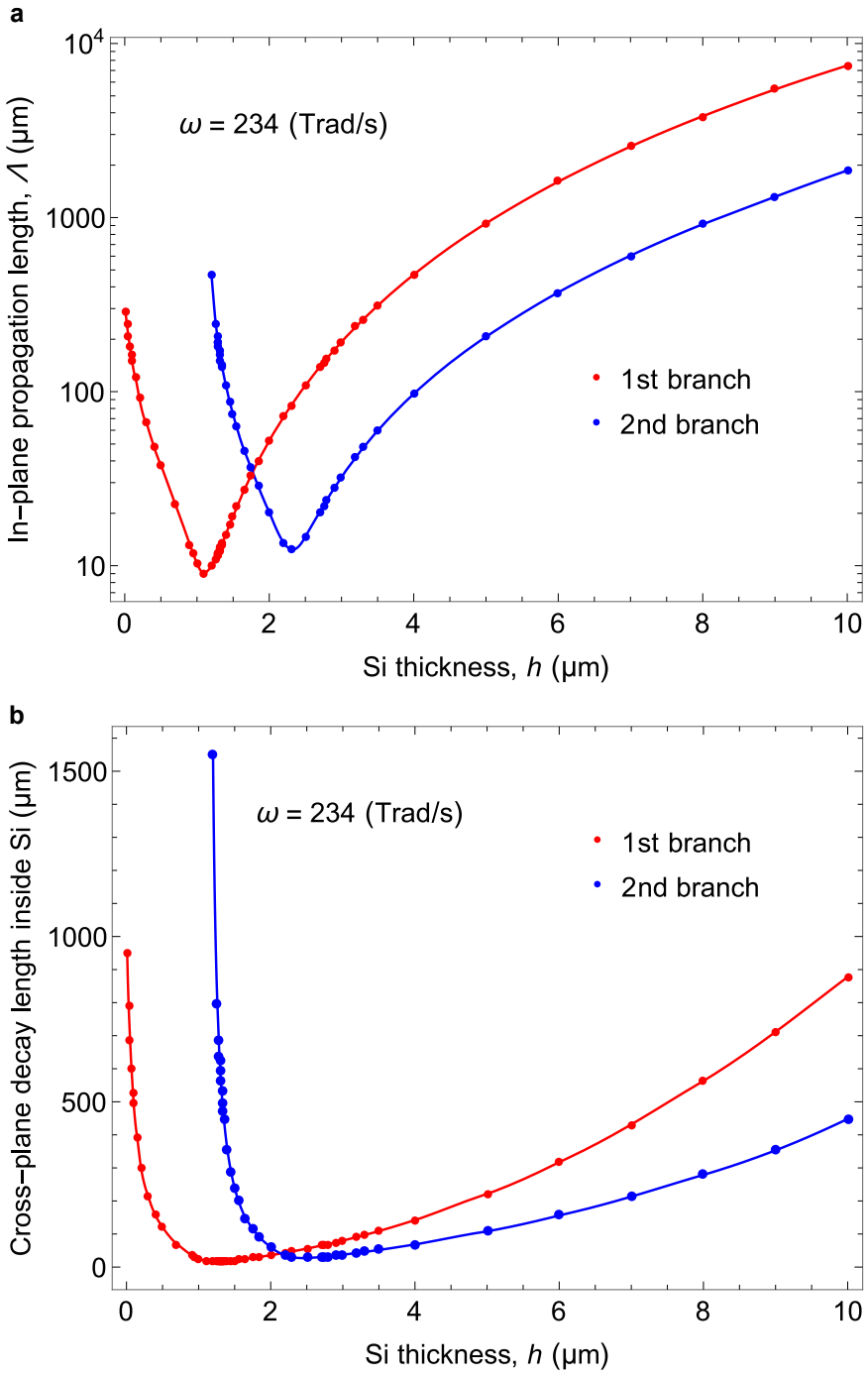

Figure2.27 **a** In-plane propagation length and **b** Cross-plane decay length inside Si for different Si thicknesses. The data were calculated at 234 Trad/s for the first and the second branches.

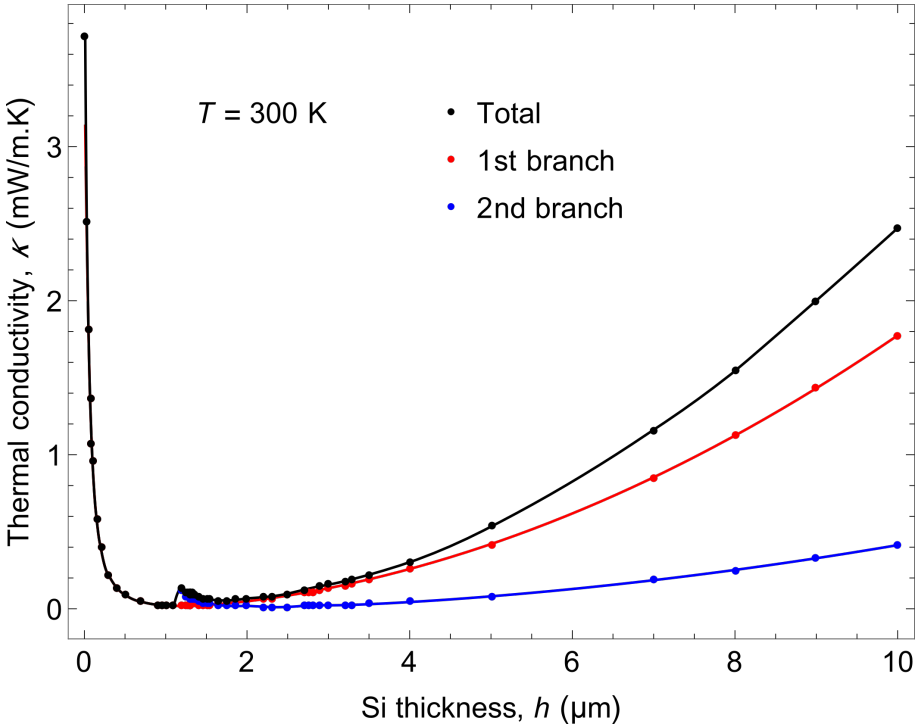

Figure2.28 Thermal conductivity for different Si thicknesses.

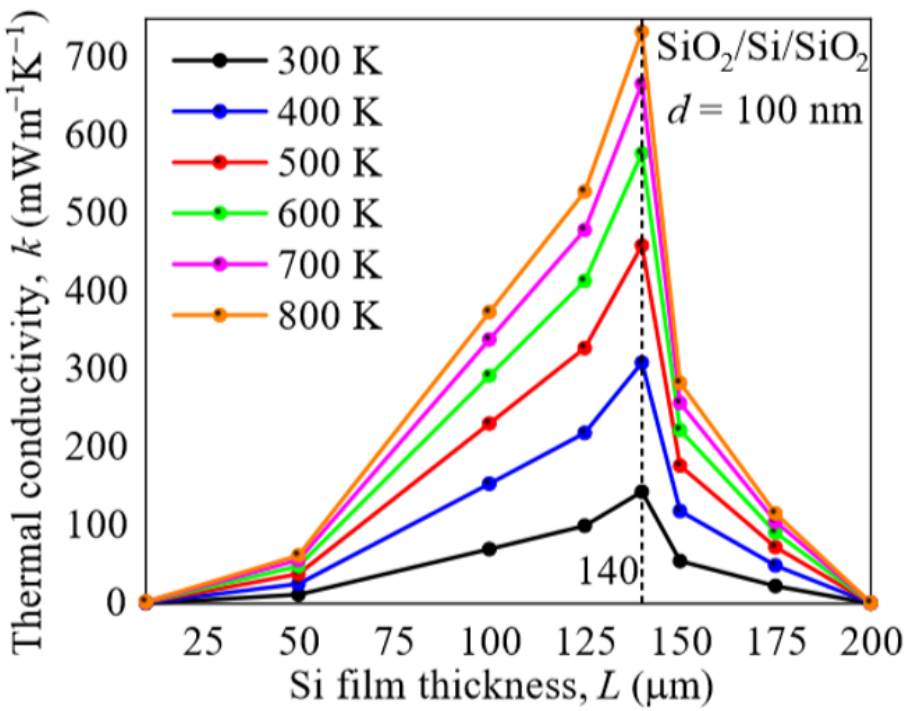

Figure2.29 Thermal conductivity of SPhP for $SiO_2/Si/SiO_2$ three-layer structure with Si thickness sweep. SiO_2 thickness is 100 nm.

2.8 Conclusions

In this chapter, we explore the SPhP propagation in three-layer systems, specifically, SiO_2-Si-SiO_2 3 layer systems. The SPhP thermal conductivity of this configuration is enhanced as the thickness of SiO_2 reduces, due to less absorption in the active polar material. For the Si thickness dependence of SPhP thermal conductivity, we found two different regimes; (1)The regime in which the evanescent coupling is predominant and (2)the regime in which the oblique propagative waves are predominant. (1) regime is when Si is thinner than any wavelength in Si, in the range of frequencies where SiO_2 permittivity has resonances, which is approximately ~ 1 μm. In this regime, the SPhP thermal conductivity is enhanced as the Si thickness is reduced, due to stronger coupling between evanescent wave at the top interface of Si and the bottom interface of Si. (2) regime is when Si is thicker than wavelength in Si for at least some frequencies. In this case, we witness waves inside Si, propagating with oblique angle which corresponds with the refractive angle defined by the refractive index difference between SiO_2 and Si. This oblique propagative wave propagates inside Si without energy loss, and excites surface waves when it reaches the interface. As the Si thickness increases, the oblique propagative wave can travel for longer distance without losing energy before reaching the SiO_2 interface, which yields longer propagation length. This leads to higher SPhP in-plane thermal conductivity with thicker Si. This finding is counter-intuitive since it had been believed that thinner structure is always better to yield high SPhP thermal conductivity, although such structure is mechanically unstable and not realistic for applications. Our results of Si and SiO_2 thickness dependency give insights to thermal design of the transistors and various other semiconductor devices.

Chapter 3

Experimental measurement setup

3.1 Introduction to experimental work of previous studies

In this chapter, we will introduce experimental researches conducted regarding the SPhP in-plane thermal transport, and their methods of measuring in-plane thermal properties of the sample.

3.1.1 The measurements of in-plane SPhP contribution to thermal conduction

Along with theoretical predictions of the in-plane component of SPhP enhancing the thermal conduction in nanofilms, several experimental demonstrations were reported [16, 17, 15]. Wu *et al.* have experimentally demonstrated SPhP thermal tranport inside SiN film using micro time-domain thermoreflectance (μTDTR) [15]. They used an optical approach to obtain the thermal property via sample reaction to the optical signals over different temperatures. The micro time-domain thermoreflectance setup is shown in Fig. 3.1a, consisted of 2 different lasers. One is a probe laser for monitoring the changes in the reflectance coefficient of the aluminium pad on the sample due to temperature changes, and the other is a pump laser which gives a pulse to the pad to periodically heat up the sample. In the work of Wu, Y. *et al.*, they placed the aluminum transducers on SiN films of four different thicknesses (30, 50, 100 and 200 nm) and measured in 300 $\sim$ 800 K conditions. For films thicker than 100 nm showed the measured thermal conductivity of film decreasing with the elevation of temperature, which indicates the phonon conduction is more predominant in relatively thick films (Fig. 3.1b). However, thinner films of 30 and 50 nm showed the thermal conductivity enhancement along with the temperature elevation. This is clearly due to the increasing contribution of SPhP over the reduction of phonon conduction.

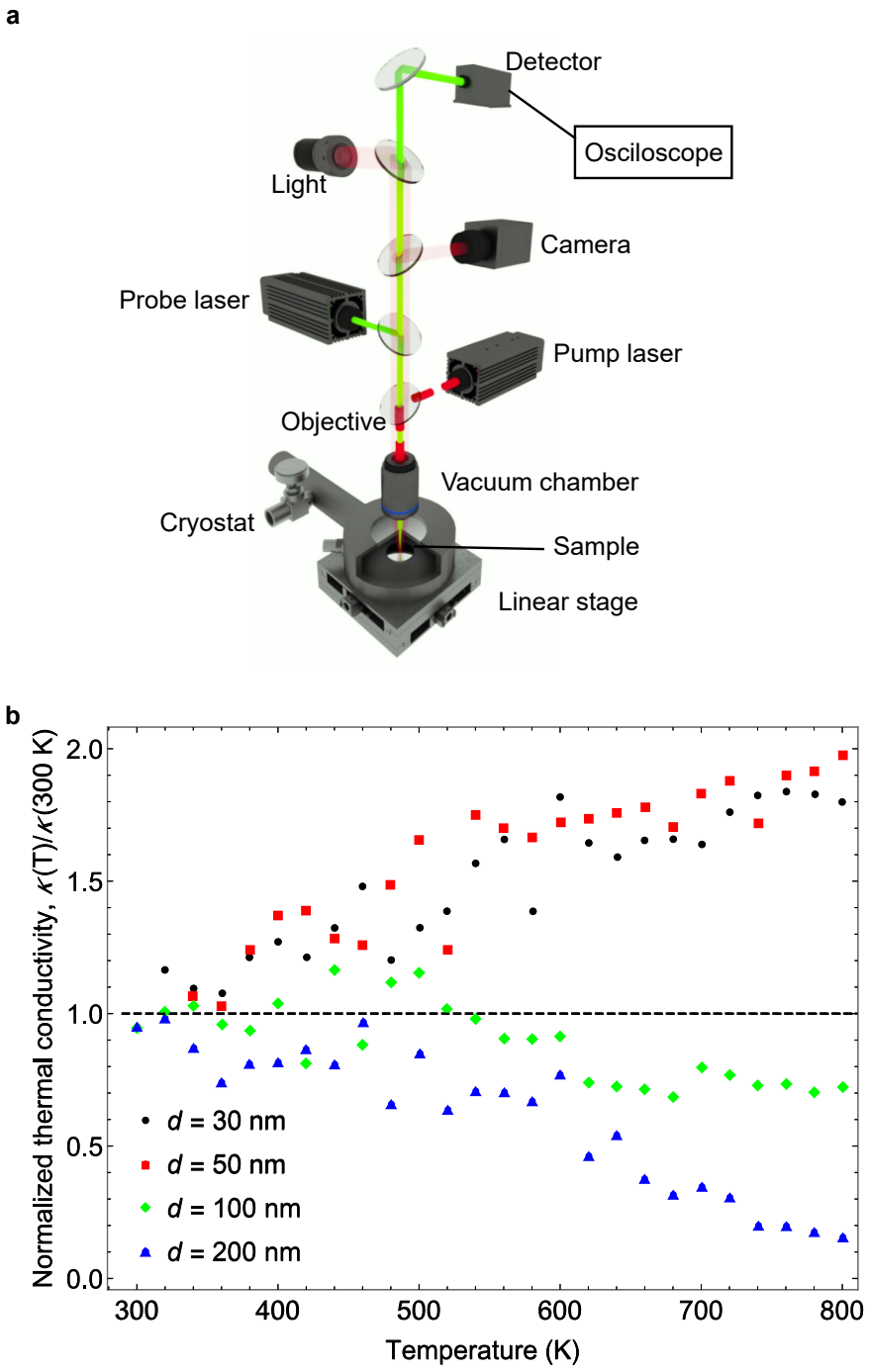

Figure3.1 **a** Schematics of μTDTR setup [14]. **b** In-plane thermal conductivity of SiN film over 300 ~ 800 K, normalized by the value at 300 K [15].

Another work on the SPhP thermal conduction of nanofilms is reported by L. Tranchant, *et al.*. They demonstrated the thickness dependence of SPhP in-plane thermal conductivity in SiO_2 film. They used both optical method and electrical method, a transient grating technique and a 3ω method respectively. The transient grating technique is a non-contact measurement without a need of heater or transducers, in which two lasers crossed at the sample film give an interference pattern as a spatially periodic temperature profile [58]. The electric measurement on in-plane thermal transfer is based on the general physics that electric resistance varies with temperature. Therefore, it requires a metal wire for joule heating and for monitoring the electrical resistance changes due to temperature changes. 3ω method is named after AC modulated input signal at 1ω, producing the resistance change at 2ω, given a component modulated at 3ω which is filtered by a Wheatstone bridge and a lock-in amplifier [59]. tranchant2019two observed the in-plane thermal conductivity increasing with the reduction of SiO_2 film thickness with both transient grating technique and 3ω method (Fig.3.2).

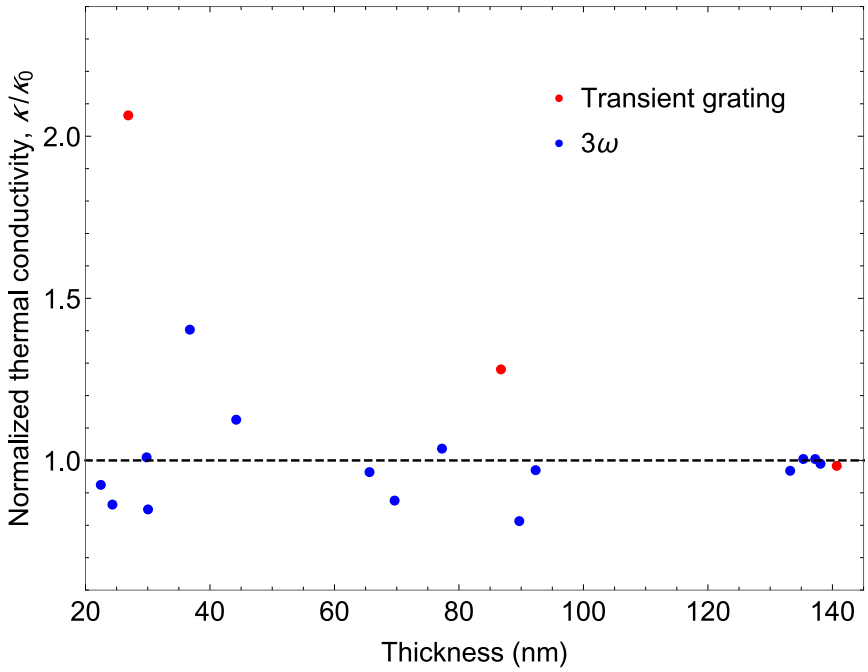

Figure3.2 Normalized in-plane thermal conductivity of SiO_2 film as a function of film thickness [16]

As for 3ω method, it is also possible to measure the in-plane thermal transfer through a nanostructure by integrating an electrical sensor. Shin *et al.* have achieved far-field coherent thermal emission in the regime of SiO_2 resonance, by tuning the thickness and width of a SiO_2 [17]. They

investigated the optimized thickness and width which is smaller than the skin depth and comparable to the thermal wavelength respectively, in order to suppress incoherent emissions and increase the coherent emission(Fig.3.3).

In their setup, they also built up a differential circuit on both heater and sensor side. For sensor side, they input DC signal and filtered 2ω signal to extract the electrical resistance modulation due to the heat dissipation from the heater. They have observed the enhanced thermal radiation losses in higher temperature and longer nanoribbons, and experimentally derived the emissivity of the nanoribbons (Fig. 3.4a). The nanoribbon with the width of 6.28 μm yields 8.5-fold higher emissivity compared to the thin film of the same thickness and the infinite width, due to the coherent resonant effect of SPhP (Fig. 3.4b).

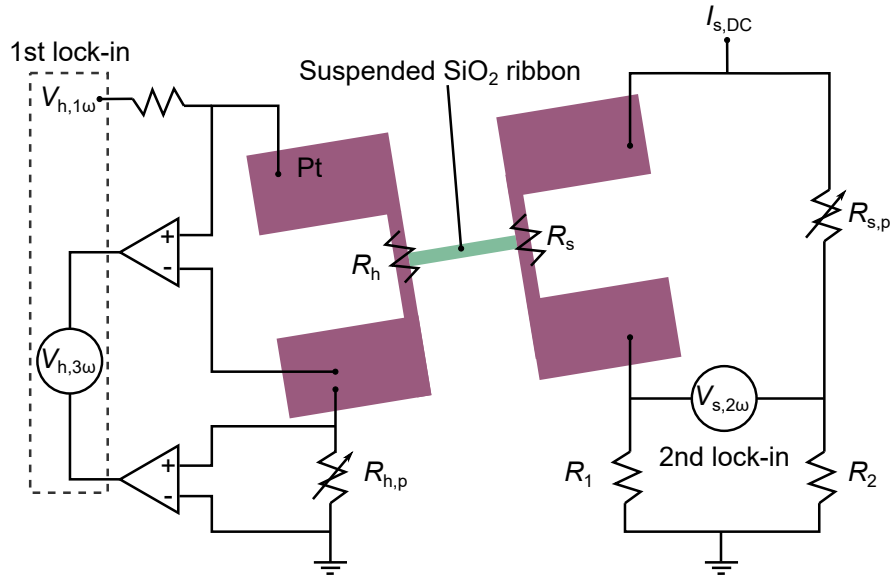

Figure3.3 Schematic of the device and the electrical setup for temperature modulation measurement. Platinum heater and sensor are integrated together with a SiO_2 nanoribbon in between [17].

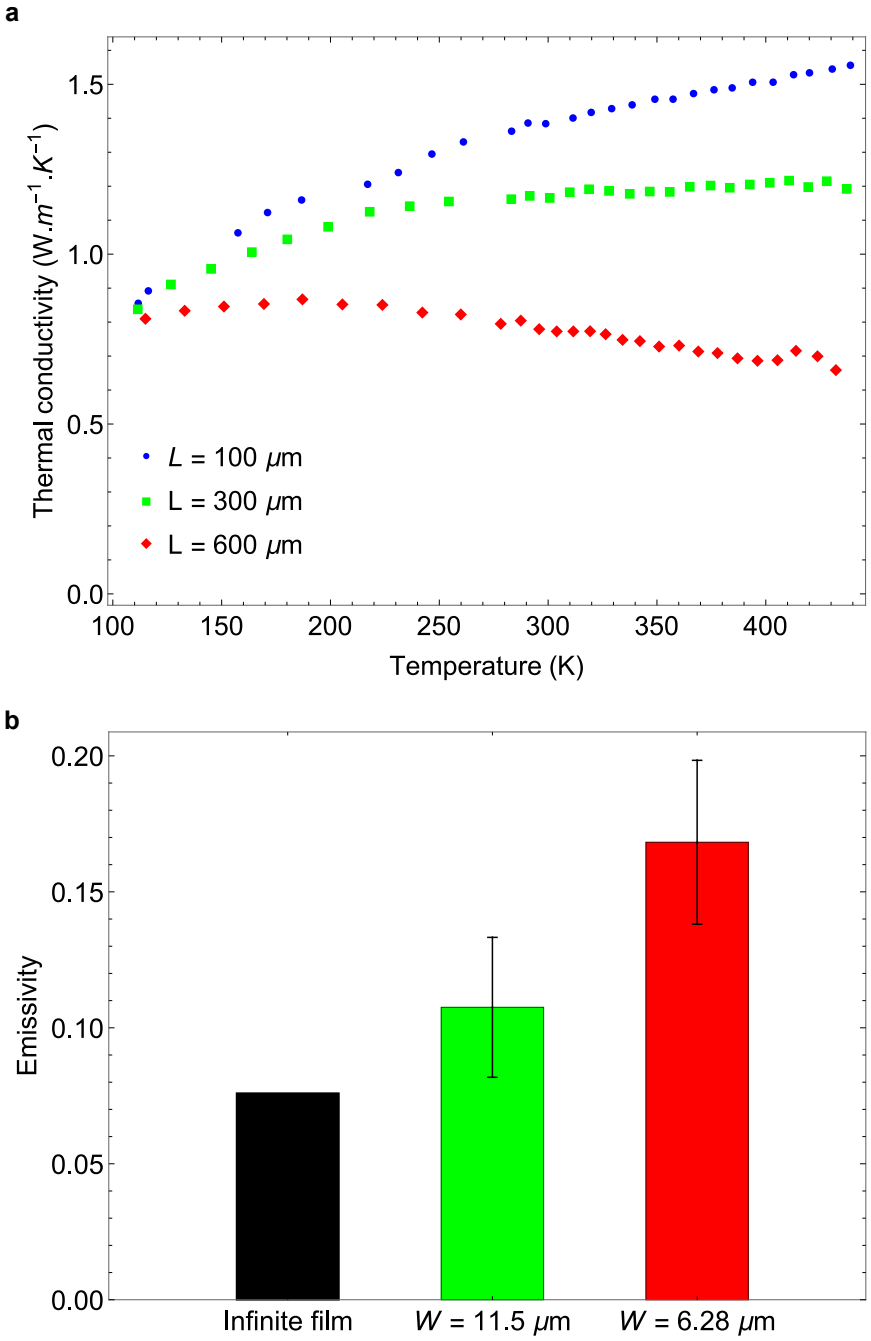

Figure3.4 **a** Measured thermal conductivity as a function of temperature for nanoribbons with width of 11.5 μm and various length. **b** Extracted emissivity of nanoribbons at room temperature. The gray bar represents the computed emissivity of an infinitely wide thin film of the same thickness [17].

3.1.2 The measurements of in-plane SPhP contribution to radiative heat transfer

The cross-plane component of SPhP contributing to the near-field radiative heat transfer is mentioned in the Chapter 1. This near-field radiative heat transfer can overcome the Planck's blackbody limit when the separation is smaller than the dominant wavelength. Another condition for overcoming the blackbody limit is the dimensions becoming smaller than the wavelength, typically in nanoscale [60, 61]. Since SPhPs can enhance thermal conduction in nanofilms, the in-plane energy of SPhPs, emitted by one body and absorbed by another, could contribute to the radiative heat transfer over Planck's limit, even in the far-field regime. The first experimental demonstration of in-plane SPhP contribution to the far-field radiative heat transfer was the work by D. Thompson, *et al.* [18]. They have measured the enhanced radiative heat exchange between SiN thin planar structures via electrical measurement. Figure. 3.5a shows their platform with two SiN thin planar structures suspended by 4 beams and Pt thermometries on to. When the thickness of the structure becomes smaller than the thermal wavelength, as predicted by Planck himself, radiative heat transfer exceeds Planck′s blackbody limit. They demonstrated this theory experimentally, by introducing the concept of the absorption cross-sections, which explains the experimental data well (Fig. 3.5b).

The same group has demonstrated the concept of thermal switch by the in-plane SPhP propagating along nanofilms [62]. They positioned a set of the emitter and the receiver of SiN nanofilms above another SiN membrane, which works as a modulator. They modulated the gap distance between the set of the emitter and the receiver and the modulator while measuring the radiative conductance between the emitter and the receiver ($G_{\text{e-m}}$). As the gap distance decreases, $G_{\text{e-m}}$ is reduced, with enhanced heat losses through near-filed radiative heat transfer between the emitter and the modulator (Fig. 3.6).

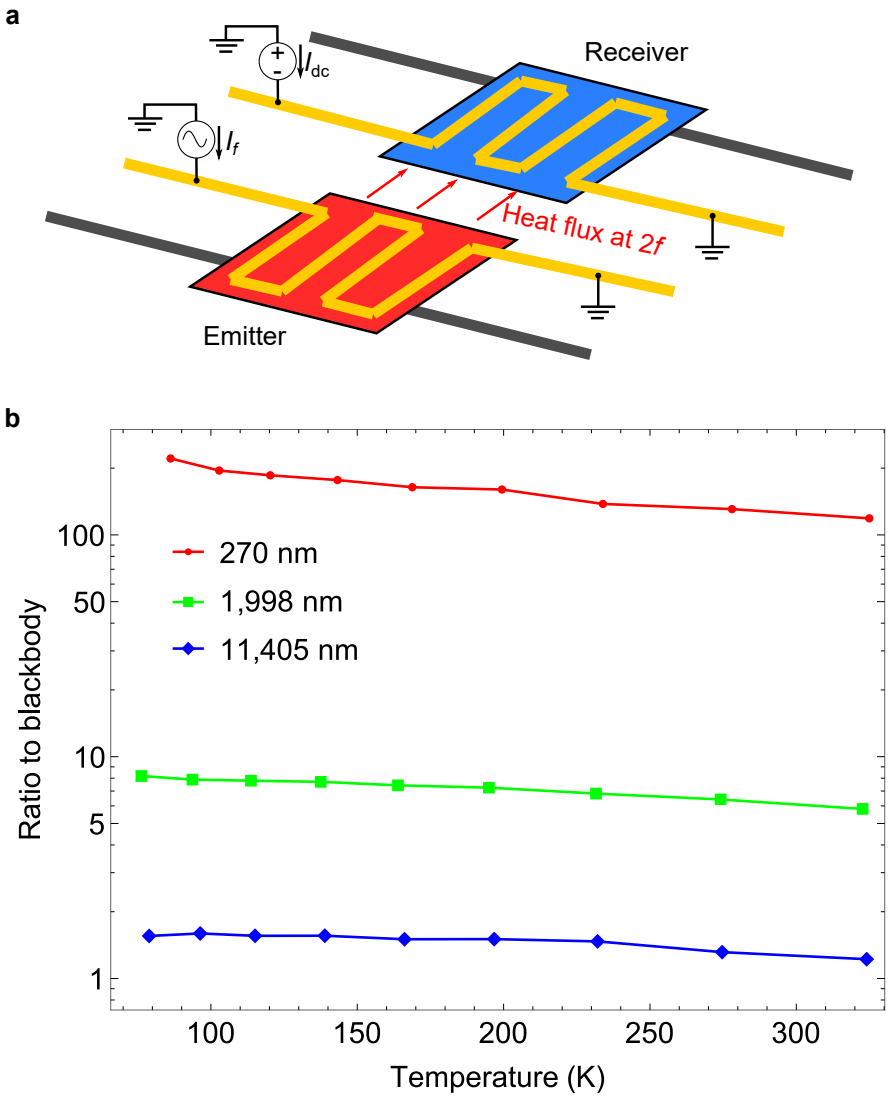

Figure3.5 **a** Schematic of the experimental platform of probing radiative heat transfer between SiN thin planar nanostructures. **b** Ratio of the measured to the estimated (using only far-field radiation theory) thermal conductance between nanostrucures. For thinner structures, it exceeds almost 100-fold of estimated value [18].

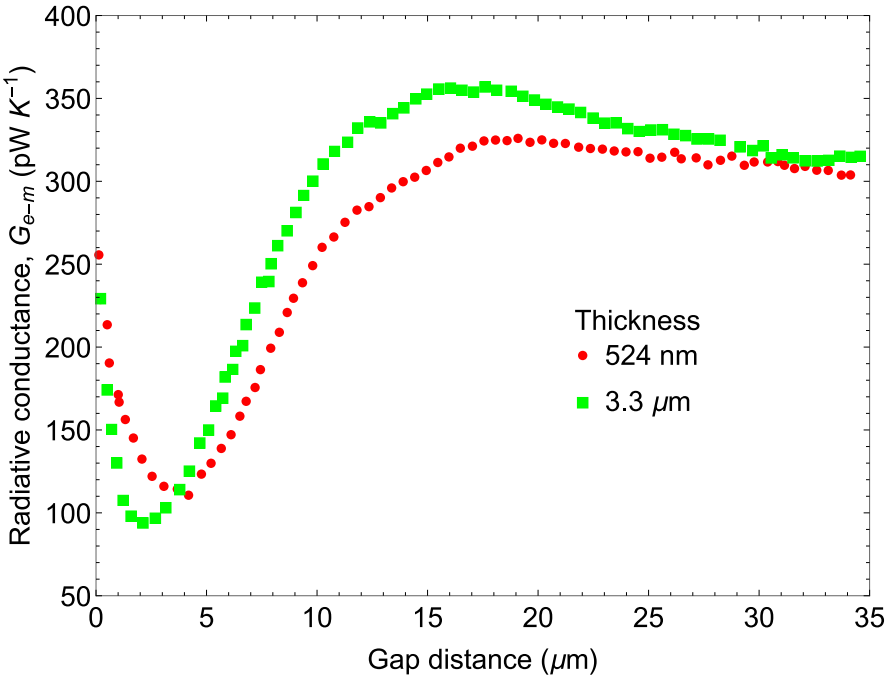

Figure3.6 Measured radiative conductance $G_{\text{e-m}}$ as a function of gap size for the 524-nm-thick (red) and 3.3-μ m-thick (green) SiN modulator. [18].

The highly sensitive 3ω method is beneficial especially for measuring radiative thermal transfer between two separated systems. In our experimental work, we utilise the electrical measurement, combining 3ω method with Wheatstone bridge, in order to achieve highly sensitive setup to observe SPhP in-plane thermal transfer between separated systems through a gap, which is explained in details in the following chapters.

3.2 Experimental setup and device fabrications

3.2.1 3 ω method coupled with Wheatstone bridge

For detection of radiative thermal transfer through a gap, high sensitivity measurement setup with separated platforms for a heater and a sensor is required. 3ω method is a method in which AC modulated input generates temperature modulated temperature, thus electrical signals also modulating at a certain frequency so that the signal can be filtered to achieve high sensitivity. When a current of $I = I_0 \cos(\omega t) = I_0 \mathrm{Re}(e^{i\omega t})$ is input into an electrical resistance of the heater, R_{h0}, the input power given by Joule's law is

$$P_{input} = R_{h0} I^2 = R_{h0} I_0^2 \cos^2(\omega t) = P_{dc}\left[1 + \cos(2\omega t)\right] = P_{dc}\mathrm{Re}(1 + e^{i2\omega t}), \tag{3.1}$$

while $P_{dc} = \frac{1}{2} R_{h0} I_0^2$. Meanwhile, Joule heating generates temperature elevation, leading to the electrical resistance increases which can be described as below.

$$R(T) = R_{h0}\left[1 + \alpha(T - T_0) + \beta(T - T_0)^2 + ...\right]. \tag{3.2}$$

The coefficients are defined $\alpha = \frac{R'(T_0)}{R(T_0)}$, $\beta = \frac{R''(T_0)}{2R(T_0)}$ as temperature derivatives, while T_0 is the ambient temperature and $T - T_0 = \Delta T_{h,dc} + \mathrm{Re}(T_{h,2\omega} e^{2i\omega t})$. This resistance changes induce the voltage on the resistance elevated accordingly.

$$V_h = RI = V_0\left[1 + \alpha(T - T_0) + \beta(T - T_0)^2 + ...\right]\mathrm{Re}(e^{i\omega t}), \tag{3.3}$$

where $V_0 = R_0 I_0$. Assuming that contributions from higher than the third order are negligible, the voltage above can be rewritten as,

$$V_h = V_0\left[1 + \alpha(T - T_0) + \beta(T - T_0)^2\right]\mathrm{Re}(e^{i\omega t}) = \mathrm{Re}(V_\omega e^{i\omega t} + V_{3\omega} e^{3i\omega t} + V_{5\omega} e^{5i\omega t}). \tag{3.4}$$

In the end, the relation between the voltage terms and temperature rise is

$$V_\omega = V_0\left[1 + \alpha\Delta T_{h,dc} + \beta\Delta T_{h,dc}^2 + \frac{1}{2}(\alpha + 2\beta\Delta T_{h,dc})T_{2\omega} + \frac{\beta}{2}|T_{h,2\omega}|^2\right], \tag{3.5}$$

$$V_{3\omega} = \frac{V_0}{2}\left[(\alpha + 2\beta\Delta T_{h,dc})T_{h,2\omega} + \frac{\beta}{2}|T_{h,2\omega}|^2\right], \tag{3.6}$$

$$V_{5\omega} = \frac{V_0}{4}\beta T_{h,2\omega}^2. \tag{3.7}$$

The coefficients are defined from the calibrations curve of V_ω for different temperatures by measuring the V_ω at high frequency where $T_{h,2\omega}$ is negligible and V_ω can be reduced to as follows,

$$V_\omega(\omega \to \infty) \equiv V_\infty = V_0(1 + \alpha\Delta T_{h,dc} + \beta\Delta T_{h,dc}^2). \tag{3.8}$$

Here, we defined a coefficient S as $\alpha + \beta\Delta T_{h,dc} = \sqrt{S}$. The coefficient S can be obtained by

$$S = \alpha^2 - 4\beta\left(1 - \frac{V_\infty}{V_0}\right). \tag{3.9}$$

The temperature elevation by Joule heating on the heater side $T_{h,2\omega}$ is derived from the 3ω signal and the coefficients:

$$\frac{V_{3\omega}}{V_0} = \sqrt{S}\frac{T_{h,2\omega}}{2} + \beta\left(\frac{T_{h,2\omega}}{2}\right)^2, \tag{3.10}$$

$$T_{h,2\omega} = \frac{\sqrt{S + 4\beta V_{3\omega}/V_0} - \sqrt{S}}{\beta}. \tag{3.11}$$

On the sensor side, small d.c. current (I_s) is input to detect the sensor voltage (V_s) elevation by the sensor resistance (R_s) increase due to the heat flux coming from the heater, oscillating at 2ω,

$$V_s = R_s I_s = V_{s0}\left[1 + \alpha(T_s - T_0) + \beta(T_s - T_0)^2 + ...\right]. \tag{3.12}$$

Taking account that $T_s - T_0 = \Delta T_{s,dc} + \mathrm{Re}(T_{s,2\omega}\mathrm{e}^{2i\omega t})$, the sensor voltage is rewritten,

$$V_s = V_m + \mathrm{Re}(V_{2\omega}\mathrm{e}^{2i\omega t} + V_{4\omega}\mathrm{e}^{4i\omega t}), \tag{3.13}$$

where

$$V_m = V_{s0}\left[1 + \alpha\Delta T_{s,dc} + \beta\Delta T_{s,dc}^2 + \frac{\beta}{2}|T_{s,2\omega}|^2\right], \tag{3.14}$$

$$V_{2\omega} = V_{s0}\left(\alpha + 2\beta\Delta T_{s,dc}\right)T_{s,2\omega}, \tag{3.15}$$

$$V_{4\omega} = \frac{V_{s0}}{2}\beta T_{s,2\omega}^2. \tag{3.16}$$

The coefficients are defined by the calibrating V_m by temperatures at high frequencies:

$$V_m(\omega \to \infty) \equiv V_{s\infty} = V_{s0}(1 + \alpha\Delta T_{s,dc} + \beta\Delta T_{s,dc}^2). \tag{3.17}$$

The coefficient S was defined again $\alpha + \beta\Delta T_{dc} = \sqrt{S}$ and derived by $S = \alpha^2 - 4\beta\left(1 - \frac{V_\infty}{V_{s0}}\right)$. The temperature elevation on the sensor side due to the heat flux from the heater side was obtained by

$$T_{s,2\omega} = \frac{V_{2\omega}}{\sqrt{S}V_{s0}}. \tag{3.18}$$

In order to achieve a highly sensitive thermal measurement setup, especially on the sensor side, we have coupled the 3ω method with the Wheatstone bridge. The heater resistance was connected to the half-bridge and the sensor side to the full-bridge (Fig.3.7).

Both bridges were balanced at the beginning of the measurement. On the heater side, only the voltage changes due to the temperature increases remain after being filtered by the third differential amplifier. The $V_{3\omega}$ which gives $T_{h,2\omega}$, the heater temperature elevation, is finally filtered by a lock-in-amplifier. On the sensor side, the voltage signal due to the temperature changes are detected at between point A and B (V_{AB}). Assuming the voltage on the fixed resistance of R_1 as V_1, solving the Wheatstone bridge circuit gives V_{AB} as,

$$V_{AB} = \frac{R_2 V_s - R_{sp} V_1}{R_2 + R_{sp}}. \tag{3.19}$$

Since $V_s = V_m + \mathrm{Re}(V_{2\omega}e^{2i\omega t} + V_{4\omega}e^{4i\omega t})$, V_{AB} can be also described as $V_{AB} = W_{dc} + \mathrm{Re}(W_{2\omega}e^{2i\omega t} + W_{4\omega}e^{4i\omega t})$. Typically, 2ω component $V_{2\omega}$ which gives $T_{s,2\omega}$ is

$$V_{2\omega} = \left(1 + \frac{R_{sp}}{R_2}\right) W_{2\omega}. \tag{3.20}$$

This signal is filtered again by a lock-in amplifier connected in between the point A and B. Therefore, the temperature rise on the sensor, $T_{s,2\omega}$ can be rewritten using the actual detected signal of $W_{2\omega}$:

$$T_{s,2\omega} = \left(1 + \frac{R_{sp}}{R_2}\right) \frac{W_{2\omega}}{\sqrt{S}V_{s0}}. \tag{3.21}$$

Figure. 3.8 shows the probe station in which the sample is positioned with 4 probes (2 on the heater side and 2 on the sensor side) probing the electrodes of the heater and the sensor.

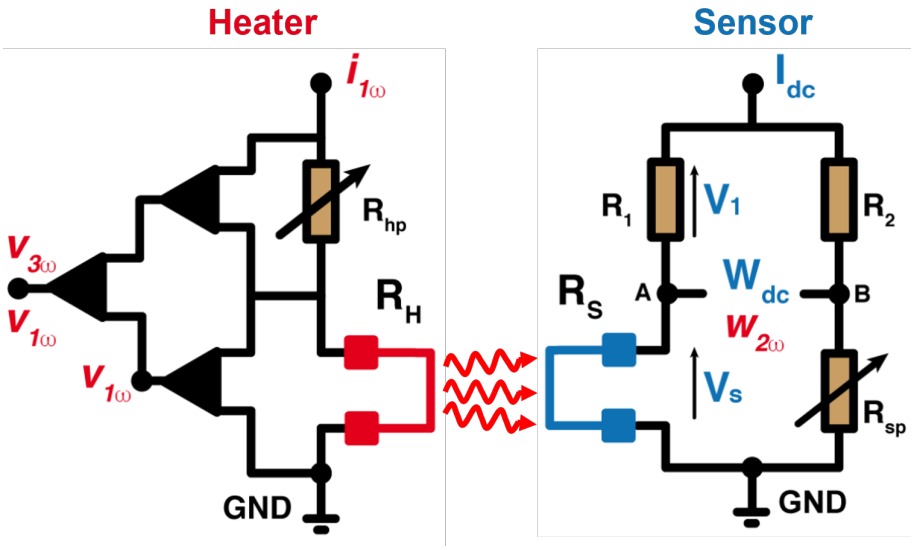

Figure3.7 Electrical circuit schematics of our setup of 3ω coupled with Wheatstone bridge technique. There is a differential circuit on the heater side and a Wheatstone bridge on the sensor side to filter 3ω and 2ω signal respectively.

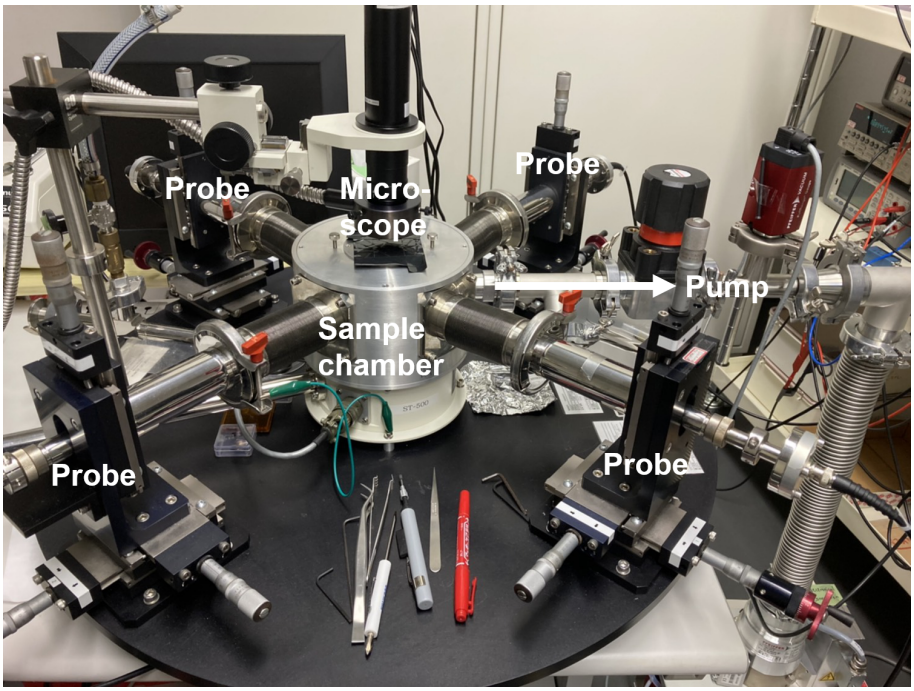

Figure3.8 Picture of the probe station of 3ω coupled with Wheatstone bridge setup. Four probes are integrated in the sample chamber, which is pumped to be vacuum.

Figure. 3.9 shows devices and equipment consisting the setup. Two lock-in-amplifiers (LIA) filter the 1ω signal and the 3ω signal at each output of the differential amplifier on the heater side. The LIA at the output of the differential amplifier on the R_h monitors 1ω component in order to calculate R_{h0}. The LIA at the output of the third differential amplifier filters 1ω component and 3ω component in order to minimize the differential 1ω component and to calculate $\Delta T_{h,ac,amp}$ respectively. On the sensor side, 2 nanovoltmeters measure V_{Rs} and V_{R1} to derive R_{s0} and I_2, therefore R_{sp}. Another voltmeter measures the DC component between the bridge for balancing. The LIA filters 2ω component between the bridge. The temperature in probe the station chamber is manipulated by a temperature controller, varying from the room temperature to 400 K.

A specific labview interface is built up for this setup. What is unique about this interface is that it scans the parameters: temperature of the probe station, Ac amplitude and frequency of the input current, DC current input, by remote controls. This allows us to extract TCR for each parameter conditions, instead of reusing the value which was obtained for one certain condition.

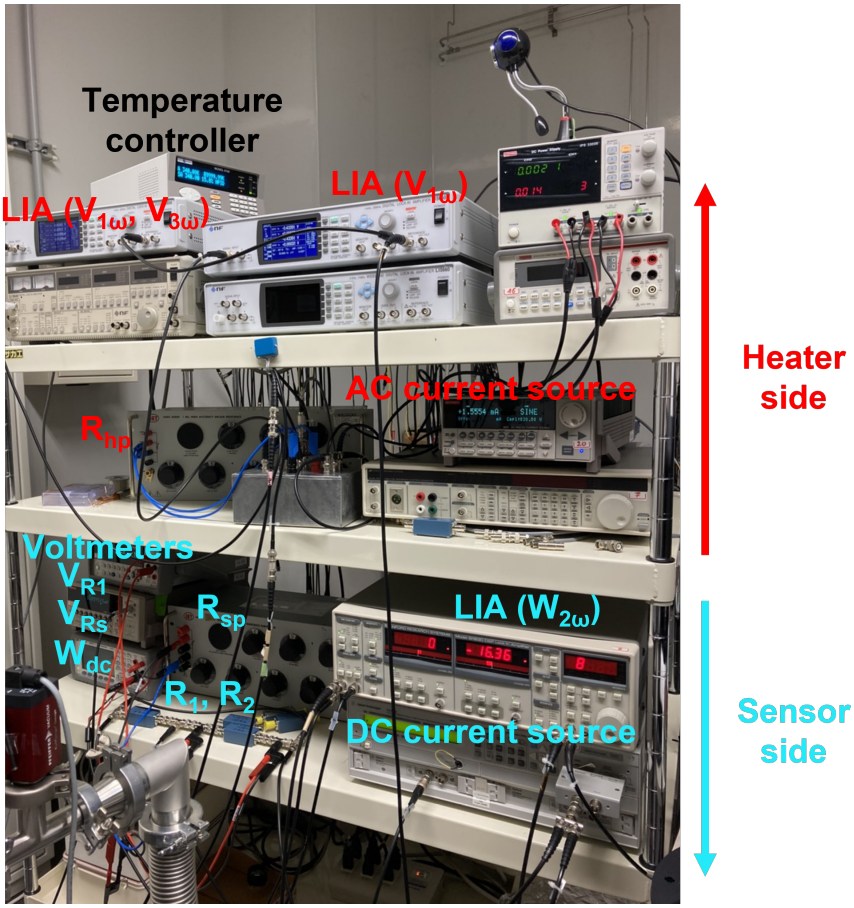

Figure3.9 Picture of the equipment and devices of 3ω coupled with Wheatstone bridge setup. The abbreviation "LIA" stands for lock-in-amplifier.

3.2.2 Device design and thermal model

The thermal property was measured using our 3ω coupled with Wheatstone bridge setup, therefore the fabricated device was consisted of a heater platform and a sensor platform suspended by beams, with a metal heater and a metal sensor integrated on each platform. Figure 3.10a shows the schematic of the device. The device was fabricated from a silicon-on-insulator (SOI) wafer with top device layer of Si (10-μm thick), oxide layer of SiO_2 (2-μm thick), and bottom handle layer of Si (400-μm thick). The handle layer was removed underneath the device in order to suspend it. The heater and the sensor were integrated by depositing thin metal wires symmetrically. Both Si plates are sandwiched by SiO_2 nanolayers, which generate SPhPs, and integrated with platinum (Pt) thermometers on top. A sinusoidal electrical current $I(\omega)$ is applied to the Pt thermometer of the hot plate, causing temperature rise due to Joule heating. The radiative heat flux emitted from the hot plate is absorbed in the cold plate. The resulting modulated temperature rise on the cold plate is calculated from the voltage fluctuation at 2ω measured by flowing a d.c. electrical current I_{dc} along the thermometer. The hot plate and the cold plate were separated by a gap of ~ 10 μm (Fig. 3.10b). Each Si plate had two extra beams used for thermal passes during the deep reactive ion etching of Si layer. The extra beams were cut by focused ion beam (FIB) at the end of all the fabrication process to achieve a high thermal isolation, thus high sensitivity to the temperature modulation.

Effective gap thermal conductance was calculated by using the input power (P_{dc}) on the heater side, $T_{h,2\omega}$ and $T_{s,2\omega}$, derived as explained in the section 3.2.1. Using the input power on the heater, the gap conductance between the hot and the cold plate (G_{g}), and the losses through the supporting beams (G_{b}) and radiation (G_{loss}), one can solve the thermal circuit equations as below due to the energy conversion (Fig. 3.10a):

$$P_{\mathrm{dc}} = G_{\mathrm{b}}(T_{\mathrm{h}} - T_0) + G_{\mathrm{g}}(T_{\mathrm{h}} - T_{\mathrm{s}}) + G_{\mathrm{loss}}(T_{\mathrm{h}} - T_0), \tag{3.22}$$

$$G_{\mathrm{g}}(T_{\mathrm{h}} - T_{\mathrm{s}}) = G_{\mathrm{b}}(T_{\mathrm{s}} - T_0) + G_{\mathrm{loss}}(T_{\mathrm{s}} - T_0), \tag{3.23}$$

where G_b, G_g and G_{loss} are thermal conductance of the beams, through the gap and of radiation losses, respectively. Equations above can be recalculated as

$$P_{\mathrm{dc}} = (G_{\mathrm{b}} + G_{\mathrm{loss}})(\Delta T_{\mathrm{h}} + \Delta T_{\mathrm{s}}), \tag{3.24}$$

$$(\Delta T_{\mathrm{h}} + \Delta T_{\mathrm{s}})G_{\mathrm{g}} = (G_{\mathrm{b}} + G_{\mathrm{loss}})\Delta T_{\mathrm{s}}. \tag{3.25}$$

Therefore, the gap thermal conductance can be obtained as

$$G_{\mathrm{g}} = P_{\mathrm{dc}} \frac{T_{s,2\omega}}{T_{h,2\omega}^2 - T_{s,2\omega}^2}. \tag{3.26}$$

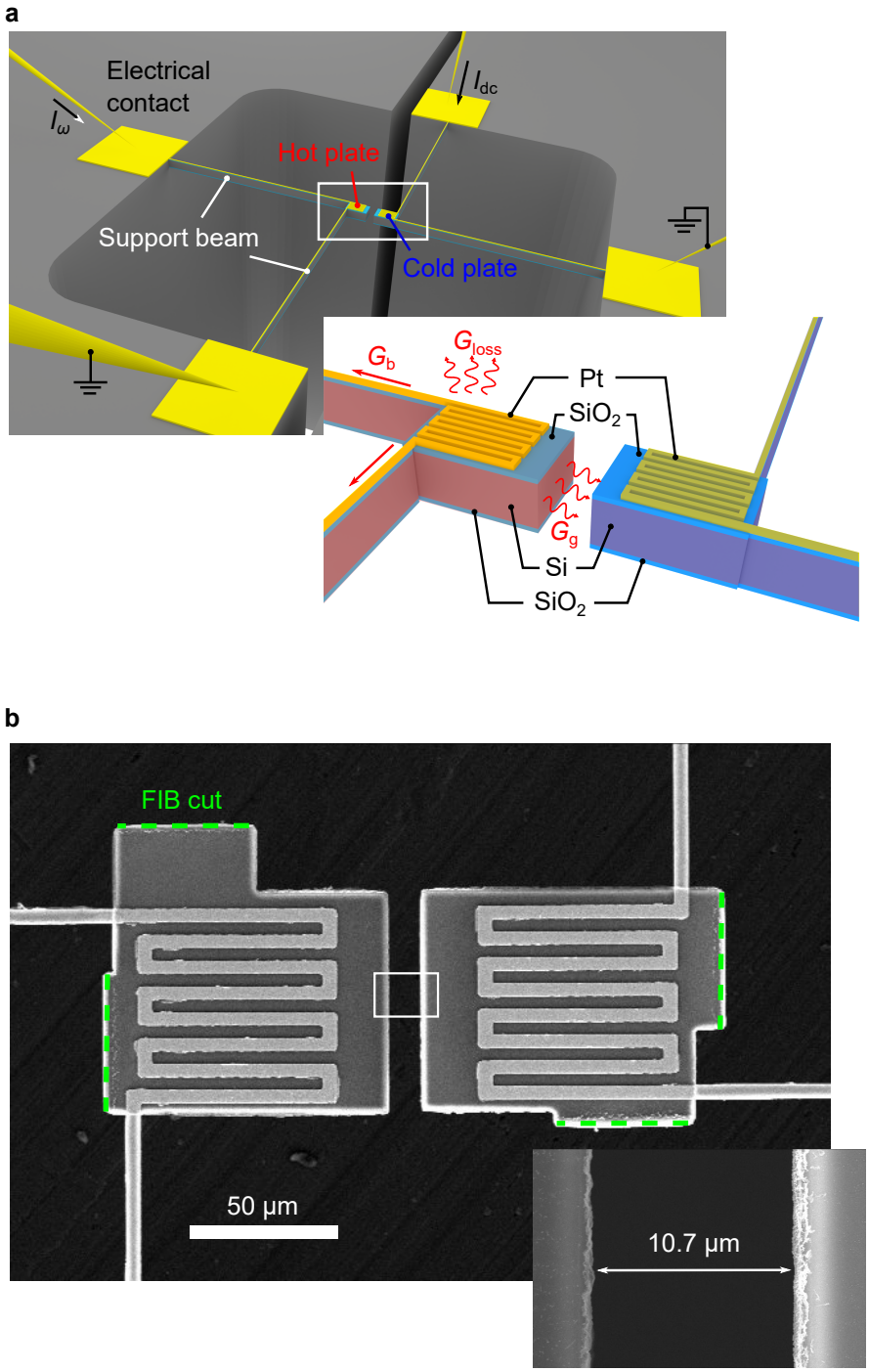

Figure3.10 **a** Schematic of the device. Each Si plates are suspended by two support beams. The right bottom inset is the zoom-in on the hot and the cold plate. **b** Scanning electron microscope (SEM) images of the top view of the device and the zoom-in on the region marked with the rectangular box. After all the fabrication process, the extra beams were cut by focused ion beam (FIB). The actual size of the gap is measured to be g =10.7 μm

Chapter 4

Sample fabrication

4.1 Fabrication techniques

The fabrication of the device can be roughly divided into 3 steps; backside etching, front side metal patterning, and front side Si structure patterning. Figure. 4.1 shows the schematic of fabrication process flow.

The SOI we used had the top device layer of 10 μm thick Si, the box layer of 2 μm thick SiO_2, and the handle layer of 300 μm thick Si. The wafer was first processed by the backside etching by deep reactive ion etching (DRIE) of a Bosch process (Fig.4.1(1)–(2)). An aluminium mask was used to leave a large suspended area of the 10 μm thick device layer. The DRIE back etching process was followed by RIE process to remove the 2 μm thick SiO_2 box layer with CHF_3 gas (Fig.4.1(2)). Then the sample was processed in the thermal oxidation (Fig.4.1(3)). It was a dry process with O_2 gas flow of 1.5 L/min. For each SiO_2 thickness of 30 nm, 70 nm and 200 nm, the process conditions were 850 °C 90 min, 1000 °C 90 min and 1100 °C 180 min respectively. After oxidizing both the front and backside of the top 10 μm thick Si layer, we deposited chromium/platinum resistors of 10 nm/100 nm thick by lift-off (Fig.4.1(4) – (6)). Chromium of 10 nm was under the platinum (Pt) resistors as an adhesion layer. Silicon and oxide layers were etched according to the pattern drawn by photolithography (Fig.4.1(7)–(8)). The layers were etched by RIE, with SF_6 and CHF_3 gas for Si and SiO_2 layer respectively. The suspended SiO_2/Si/SiO_2 structures with heater or sensor resistors were fabricated. The remaining photoresist was cleaned by the O_2 plasma process (Fig.4.1)(9)). The details of the techniques and machines we used for fabrication are introduced in the following subsections.

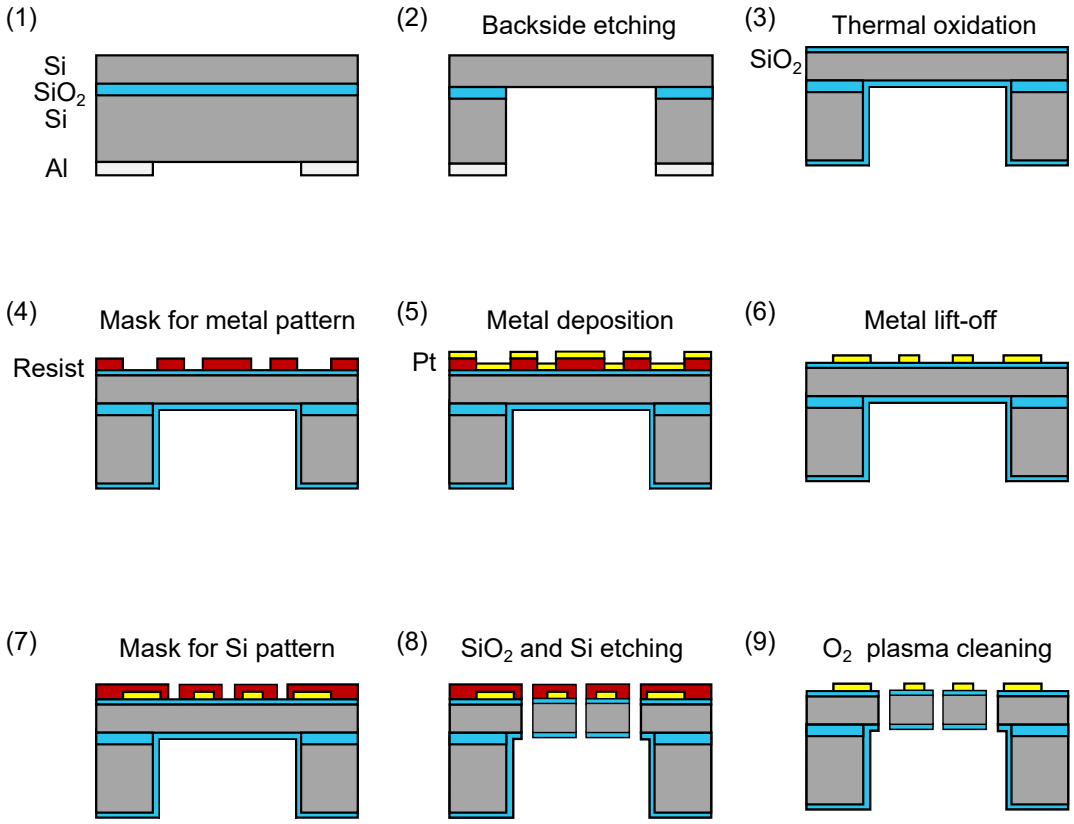

Figure4.1 Schematic of the fabrication process flow, showing the cross-sectional view of wafer sample.

Laser photo lithography

Lithography is a method to print the pattern. Later, this pattern will work as a mask for metal deposition or etching of the material underneath. The wafer is first coated by a polymer resist which is sensitive to light or electron beams. Once it is exposed to the light or beams, the chemical in the resist changes its formation and becomes either soluble or resistive to the certain solvent. The former type is named "positive" photo resist, while the latter is named "negative" photo resist. This process is called "development" and the solvent is called "developer". Figure. 4.2a shows the schematic of the photo lithography technique using positive photoresist. In our fabrication, we used photo lithography with positive photo resist (AZ1500 series) sensitive to UV light. The photolithography machine we used was laser drawer, $\mu PG101 Heidelberg$, which enables the direct writing of the pattern onto the photoresist without the need of photomasks. Figure. 4.2b shows the tabletop machine.

Deep reactive ion etching (DRIE)

Reactive ion etching is a technology to remove the material either by chemical reaction between ions of the injected gases and the material atoms, or by physically sputtering the material with the ions. For etching of Si, the SF_6 plasma is used to chemically create the gas of SiF_4 and detach Si from the surface. However, this process is isotropic etching. In order to etch Si anisotropically in depth with high aspect ratio, a particular etching method called Bosch process is needed. Figure. 4.3 shows the schematic of this Bosch process. It has etching step and passivation step switched to one another by quickly changing the gas injection. In the step of etching, Si is isotopically etched by SF_6 ions. In the passivation step, a Teflon based layer is deposited on surfaces by C_4F_8 plasma. In the beginning of the next etching step, directional etching is conducted to remove the passivation layer at the bottom caused by ion bombardment, however, sidewalls will be protected to achieve etching of high aspect ratio.

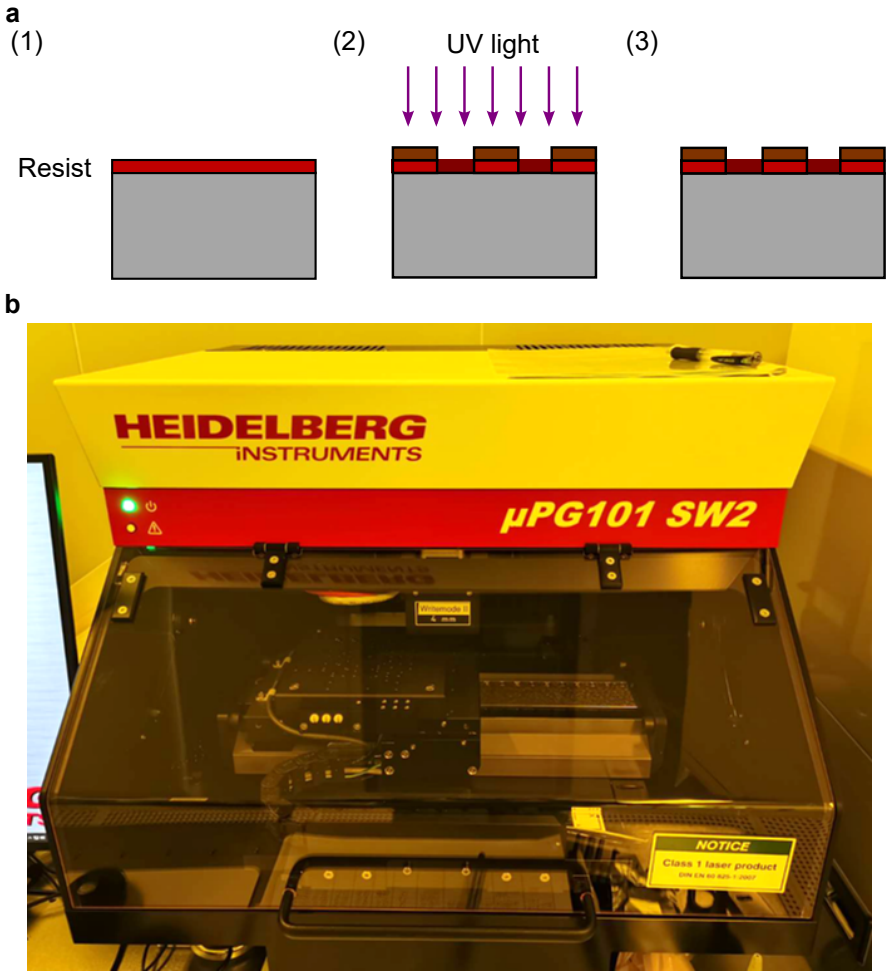

Figure4.2 **a** The schematic of photo lithography process. (1) The sample surface is coated with photo resist, using spin coater. Positive photo resist is used in this schematic. (2) The resist is exposed to UV light while masked by a photomask. The exposed area becomes soluble to the developer. (3) After the development, resist under the photomask, which was not exposed to the UV light, remains. **b** The laser writer for photo lithography, $\mu PG101 Heidelberg$

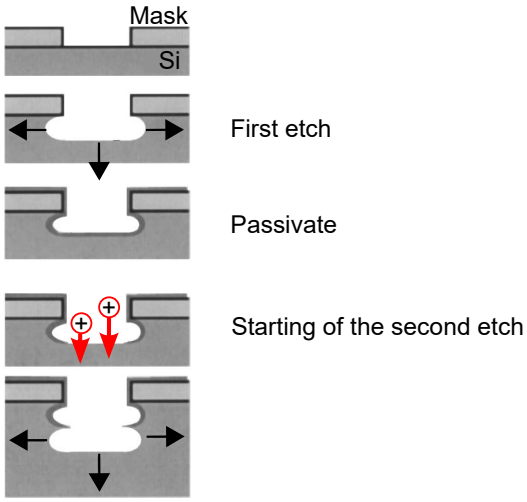

Figure4.3 The schematic of Bosch process. [19]

Figure4.4 The DRIE machine.

Metal deposition

For metal deposition, we used electron beam (EB) deposition system. Figure. 4.5 shows the inside of the EB deposition machine. The sample is fixed at the sample holder with its surface facing down. The electrons emitted from the filament will be directed to the target by magnetic field, and the target will be sputtered. The sputtered vapors will fly to the sample surface to form the deposition.

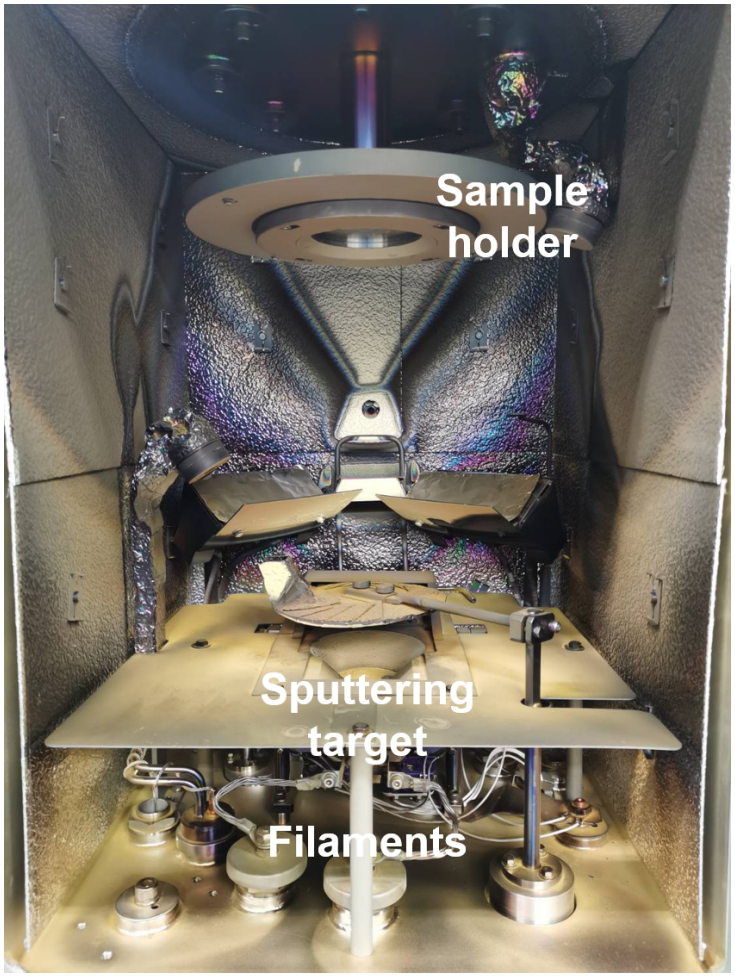

Figure4.5 The inside of the EB deposition machine.

4.2 Fabrication processes

In this section, we give explanations to each step of the fabrication flow.

Backside etching

In order to suspend the structure of the device layer in the end, the bulk of the handle layer has to be removed by etching it from the backside. This backside etching requires DRIE of a few hundreds of μm thick Si. Under such long etching process, a mask of photo resist cannot survive till the end. Therefore, we used Al mask for this particular DRIE step. Aluminium of 100 nm thickness was deposited on the backside of the SOI wafer, and laser photo lithography was used to pattern the backside Si to be etched. Aluminum was then etched by an Al etchant (mixture of acetic acid, nitric acid, and phosphoric acid) according to the photoresist masking. This corresponds to the step (1) in Fig.4.1. Then, we etched the handle layer by DRIE machine shown in Fig.4.4. This is followed by the removal of the box layer of SiO_2 by RIE using CHF_4 gas. This corresponds to the step (2) in Fig.4.1.

Thermal oxidation

In order to finally have a suspended structure of SiO_2-Si-SiO_2 three-layer system, we thermally oxidized the sample at this point (Fig.4.1, step (3)). We cleaned the sample carefully and put it into the oxidation furnace (Fig. 4.6). Thermal oxidation was conducted under dry condition with O_2 gas injections at 1000 °C for 90 minutes. The thickness of oxide layer was confirmed to be approximately 76 nm by interferometry method (Fig.4.7).

Frontside metal liftoff

In order to have metal wires as a micro-heater and a micro-sensor, metal patterning was done by liftoff process. The laser photo lithography was used again to pattern the metal pattern (Fig.4.1, step (4)). After the development, we removed SiO_2 layer in the open area by BHF to have no oxide layer under the metal. The metal of Cr, 10 nm thick, and Pt, 100 nm thick, were deposited using EB deposition machine (Fig.4.1, step (5)). Chromium was deposited as a adhesion layer. The photo resist was then removed by acetone to lift-off unnecessary metal in surrounding area (Fig.4.1, step (6)).

Frontside Si structure patterning

In order to have fully suspended structure of SiO_2/Si/SiO_2 three-layer system, front side patterning and etching are needed, leaving the heater and the sensor platforms and suspension beams. The laser photo lithography was used to pattern the frontside Si pattern to be etched (Fig.4.1, step (7)). Then, top oxide layer was removed by RIE CHF_4 plasma, followed by DRIE of 10 μm thick Si, and again the etching of bottom SiO_2 layer by RIE CHF_3 plasma. We got suspended SiO_2-Si-SiO_2 three-layer system, protected by photoresist (Fig.4.1, step (9)), at the end of the process. The sample will go through FIB process of cutting the heater platform and the sensor platform apart with a gap, then the photoresist protection was finally removed by RIE O_2 plasma.

Figure4.6 The thermal oxidation furnace.

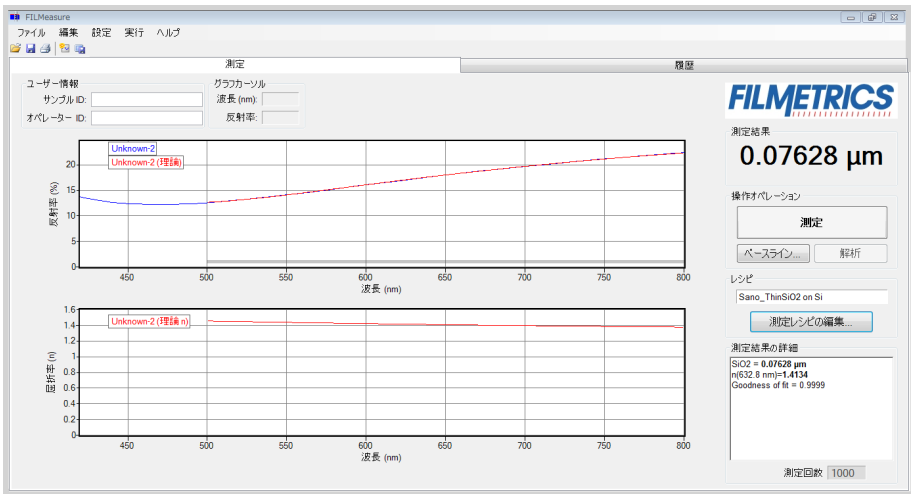

Figure4.7 The result of thermal oxide layer thickness obtained by the interferometry. The thickness was approximately 76 nm.

Chapter 5

Results and discussions

5.1 Results

The measured G_g between Si plates (Si-only system) is shown in Fig.5.1**a** (blue circles) for different holder temperatures. It increases with the holder temperature as it is an expected behavior of radiative heat transfer. The measured G_g for SiO_2/Si/SiO_2 (3-layer) system of different SiO_2 thicknesses are shown in Fig.5.1b. The experimental G_g of Si-only system shown in Fig. 5.1a are also plotted in comparison. The G_g for three-layer system increases with the holder temperature for all the SiO_2 thicknesses, indicating the heat exchange is due to radiative heat transfer. Although difference between three SiO_2 thicknesses was not clear, G_g for three-layer system were almost twice as higher than that of Si-only system.

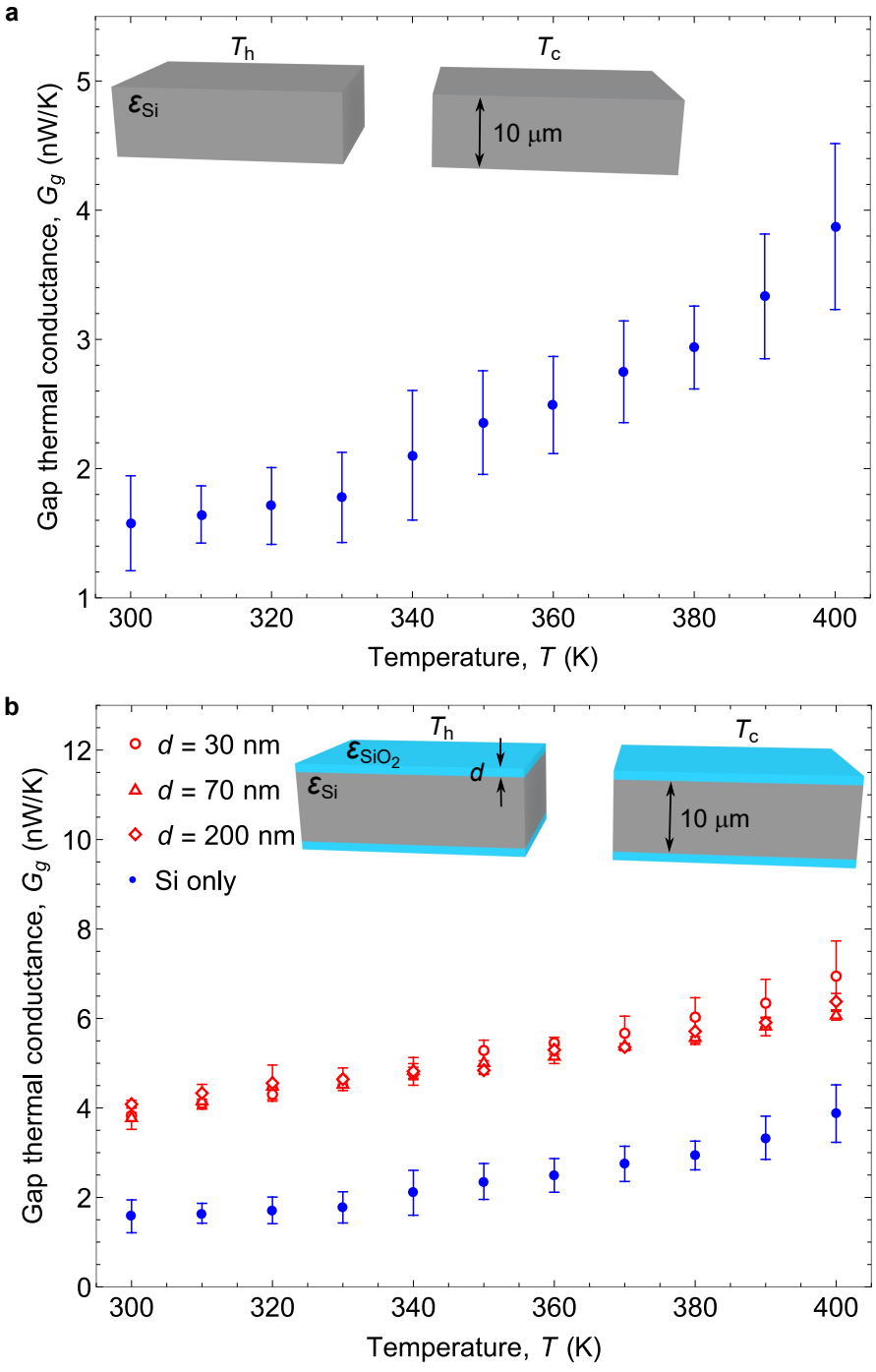

Figure5.1 Experimental gap thermal conductance for **a** Si-only system **b** SiO_2/Si/SiO_2three-layer system with SiO_2 thickness of 30, 70 and 200 nm, compared with that of only-Si layer device. Theoretical estimation of the far-field radiative heat transfer between SiO_2/Si/SiO_2 structure with a maximum SiO_2 emissivity (pink region) is much smaller than the experimental G_g.

5.2 Discussion

5.2.1 Temperature distribution on the hot plate

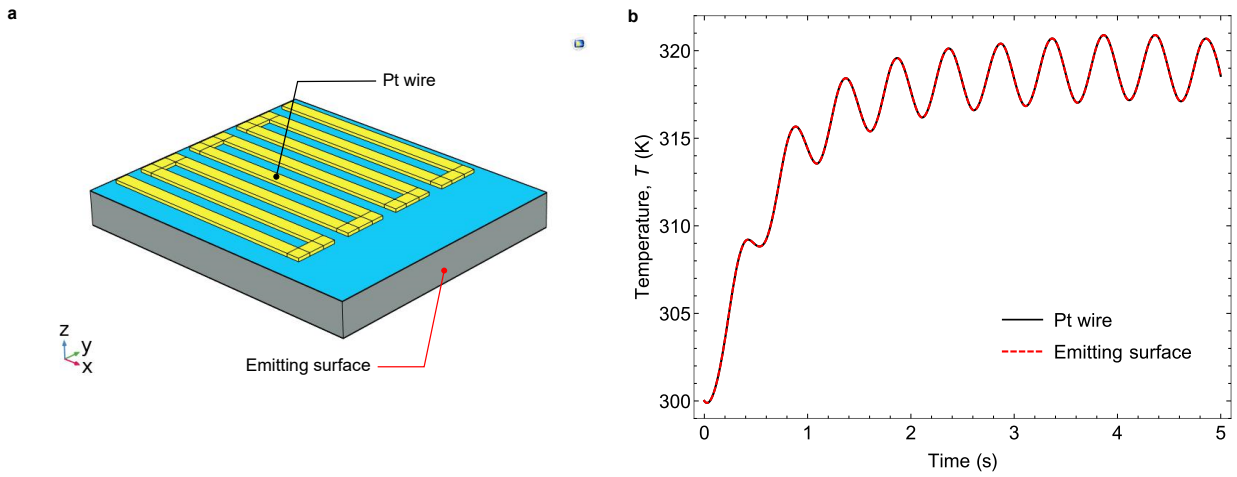

Figure5.2 **a**, Schematic of the computational model for the temperature distribution on the hot plate. The 10 μm-thick Si layer (in grey) is sandwiched with SiO_2 layers (in blue) of 200 nm in thickness. The temperature on the Pt wire and on the emitting surface are computed. **b**, Temperatures on the Pt wire and on the emitting surface.

To confirm that the temperature measured on the platinum (Pt) thermometer is equivalent to the temperature of the emitting surface of the hot plate, we determined the temperature distribution over the hot plate by using FDTD simulation. The computational system consists of a 10 μm-thick Si sandwiched with the thickest (200 nm) SiO_2 layers, as shown in Fig. 5.2a. By using a sinusoidal current with an oscillating frequency of 1 Hz to generate Joule heating, the time evolution of the temperature of the Pt wire and the emitting surface are calculated and shown in Fig. 5.2b. One can see that both spots are at the same temperature, which indicates that the temperature measured by the Pt thermometer represents an accurate estimation of the emitting surface temperature. This result is expected to apply for all modulation frequencies f= 1–100 Hz used in our experiments. As for all of the frequencies, the diffusion length $\mu = \sqrt{\alpha/2\pi f}$ of the excited thermal waves is greater than the distance between the Pt wire and the emitting surface (20 μm). For instance, as the system consists of Si mainly, its thermal diffusivity $\alpha \approx 80$ mm^2/s, μ =12732.4 μm (127.3 μm) for f=1 Hz (f=100 Hz) and therefore the thermal waves travel from the Pt wire to the emitting surface with practically no attenuation. This is the reason why these two spots exhibit nearly the

same temperature field. Regarding the time constant, the longest dimension of the hot plate island is $L = 96\ \mu$m, which yields the time constant of $\tau = L^2/\alpha \approx 0.12$ ms [63]. This also proves that the frequencies of 1-100 Hz we used for the measurement was in the range to guarantee a uniform temperature on the hot plate island.

5.2.2 Far-field radiative heat transfer between finite bodies

The theory for far-field radiative heat transfer is well-established by Stefan–Boltzmann law. It describes the heat flux radiated from a body with the emissivity of ϵ, q, is proportional to 4th power of the body's temperature,

$$q = \epsilon\sigma T^4, \tag{5.1}$$

where σ is the Stefan–Boltzmann constant. The power exchanged between the surface i and j is described as,

$$q_{12} = \sigma\epsilon_i F_{ij}(T_i^4 - T_j^4) = \sigma A_j \epsilon_j F_{ji}(T_i^4 - T_j^4), \tag{5.2}$$

where F_{ij} is a view factor, which is a geometrical function to indicate how much heat fluxes leaving one surface can reach the other surface. It is given by

$$F_{ij} = \frac{1}{A_i}\int_{A_i}\int_{A_j}\frac{\cos\theta_i \cos\theta_j}{\pi r_{ij}^2} dA_i dA_j, F_{ji} = \frac{1}{A_j}\int_{A_i}\int_{A_j}\frac{\cos\theta_j \cos\theta_i}{\pi r_{ji}^2} dA_j dA_i, \tag{5.3}$$

where $A_{i,j}$ is the surface areas of each surface, $\theta_{i,j}$ is the angles between the surface normals and a ray between the two differential areas. The distance between the differential areas is r_{ij}. The relationship $A_i F_{ij} = A_j F_{ji}$ is always satisfied. The heat fluxes from N numbers of surfaces can be written in a matrix form as

$$\sum_{j=1}^{N}\chi_{ij}q_{ij} = \sigma\sum_{j=1}^{N}F_{ij}\left(T_i^4 - T_j^4\right), \tag{5.4}$$

where $\chi_{ij} = -F_{ij}(\epsilon_j^{-1} - 1)$. Here, we consider 3 surfaces as shown in Fig.5.3a, in which the emitter with the emissivity and the temperature of (ϵ_1,T_1) and the receiver with (ϵ_2,T_2) are positioned in vacuum with ambient temperature of T_{amb}, exchanging heat fluxes.

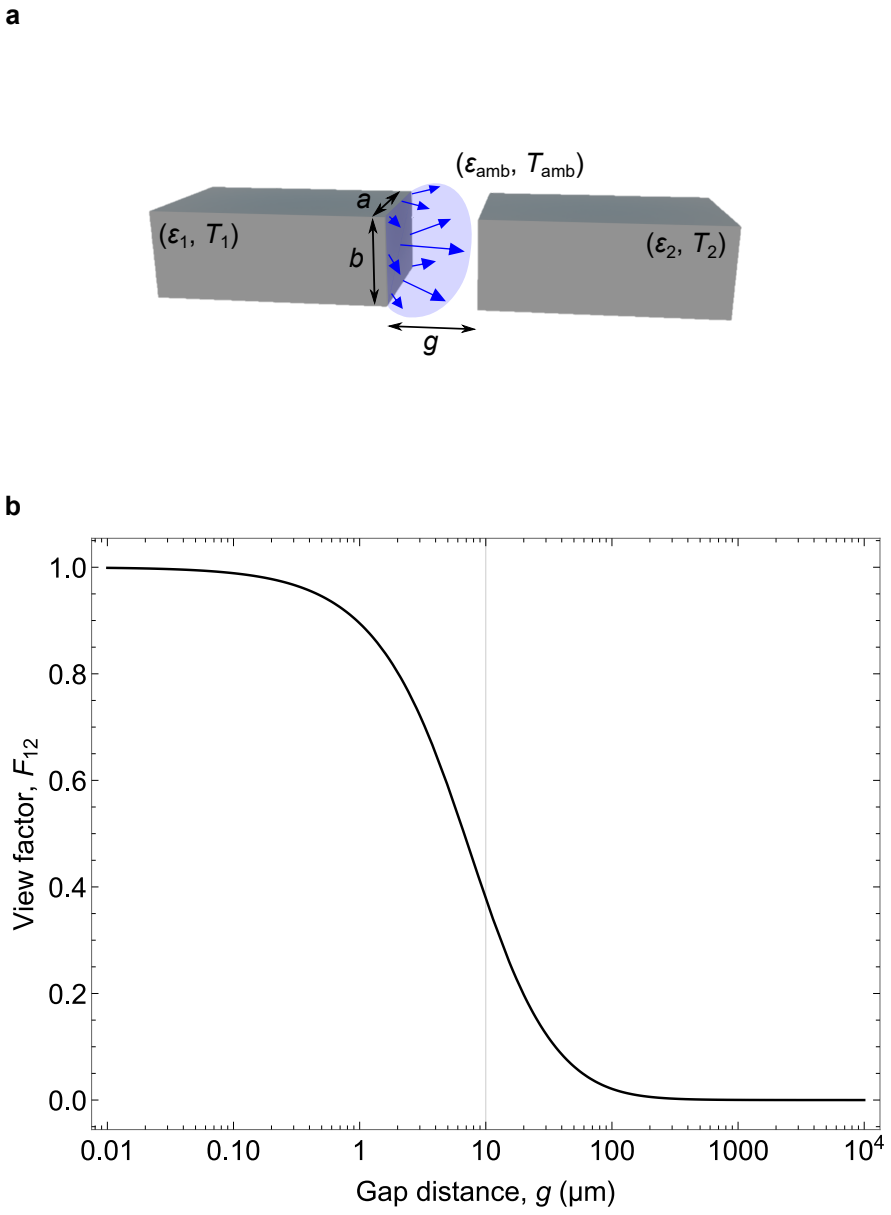

Figure5.3 a Schematic of the emitter and the receiver exchanging heat flux. b The view factor typically for our device geometry (a = 78 μm and b = 10 μm) for different gap distance.

The emitter and the receiver are in the same geometry, corresponding with our device so that their opposing surfaces have same areas, $A_1 = A_2 = ab$. Applying this condition to Eq. 5.4 gives,

$$\begin{bmatrix} \chi_{11} & \chi_{12} & \chi_{13} \\ \chi_{21} & \chi_{22} & \chi_{23} \\ \chi_{31} & \chi_{32} & \chi_{33} \end{bmatrix} \begin{bmatrix} q_1 \\ q_2 \\ q_3 \end{bmatrix} = \sigma \begin{bmatrix} F_{12}\left(T_1^4 - T_2^4\right) + F_{13}\left(T_1^4 - T_{amb}^4\right) \\ F_{21}\left(T_2^4 - T_1^4\right) + F_{23}\left(T_2^4 - T_{amb}^4\right) \\ F_{31}\left(T_{amb}^4 - T_1^4\right) + F_{32}\left(T_{amb}^4 - T_2^4\right) \end{bmatrix}, \tag{5.5}$$

while $F_{11} = F_{22}$. Since $\sum_{j=1}^{N} F_{ij} = 1$ and $A_i F_{ij} = A_j F_{ji}$ are satisfied, the view factors between the device surfaces and the ambient surface can be written as

$$\begin{aligned} F_{13} &= 1 - F_{12}, \\ F_{23} &= 1 - F_{21} = 1 - F_{12}, \\ F_{33} &= 1 - F_{31} - F_{32} = 1 - A_{13}F_{13} - A_{23}F_{23} = 1 - 2A_{13}(1 - F_{12}), \end{aligned} \tag{5.6}$$

where $A_{ij} = \frac{A_j}{A_i}$. The χ_{ij} in Eq. 5.17 are

$$\begin{bmatrix} \chi_{11} & \chi_{12} & \chi_{13} \\ \chi_{21} & \chi_{22} & \chi_{23} \\ \chi_{31} & \chi_{32} & \chi_{33} \end{bmatrix} = \begin{bmatrix} \epsilon_1^{-1} & -F_{12}(\epsilon_2^{-1} - 1) & 0 \\ -F_{12}(\epsilon_1^{-1} - 1) & \epsilon_2^{-1} & 0 \\ -A_{13}(1 - F_{12})(\epsilon_1^{-1} - 1) & -A_{13}(1 - F_{12})(\epsilon_2^{-1} - 1) & 0 \end{bmatrix}, \tag{5.7}$$

since $\epsilon_{vac} = 1$. The equation above gives

$$\begin{aligned} q_1 D &= \left[\epsilon_2^{-1} - F_{12}^2(\epsilon_2^{-1} - 1)\right]\sigma(T_1^4 - T_{amb}^4) - \sigma F_{12}(T_2^4 - T_{amb}^4), \\ q_2 D &= \left[\epsilon_1^{-1} - F_{12}^2(\epsilon_1^{-1} - 1)\right]\sigma(T_2^4 - T_{amb}^4) - \sigma F_{12}(T_1^4 - T_{amb}^4), \end{aligned} \tag{5.8}$$

where $D = \epsilon_1^{-1}\epsilon_2^{-1} - F_{12}^2(\epsilon_1^{-1} - 1)(\epsilon_2^{-1} - 1)$. Since the heat exchange between the emitter and the receiver is $q_{12} = F_{12}\left[\sigma(T_1^4 - T_2^4) + (\epsilon_2^{-1} - 1)q_2 - (\epsilon_1^{-1} - 1)q_1\right]$, q_{12} can be described as,

$$q_{12} = \epsilon\sigma\left\{(T_1^4 - T_2^4) + \frac{\left(F_{12}^{-1} - 1\right)}{\epsilon_1\epsilon_2}\left[\epsilon_1(T_1^4 - T_{amb}^4) - \epsilon_2(T_2^4 - T_{amb}^4)\right]\right\}, \tag{5.9}$$

where $\epsilon^{-1} = \epsilon_1^{-1} + \epsilon_2^{-1} - 1 + (F_{12}^{-1} - 1)\epsilon_1^{-1}\epsilon_2^{-1}$. In our case of the device with only Si layer, $\epsilon_1 = \epsilon_2 = \epsilon_{Si}$ therefore above equation can be reduced to

$$q_{12} = \frac{\epsilon_{Si}\sigma\left(T_1^4 - T_2^4\right)}{F_{12}^{-1} + 1 - \epsilon_1}. \tag{5.10}$$

One can see that it is independent of T_{amb}. The gap thermal conductance between the emitter and the receiver via far-field radiative heat transfer (FFRHT) is,

$$G_{FFRHT} = \frac{q_{12}}{T_1 - T_2}. \tag{5.11}$$

For the configuration of opposing rectangles, the view factor is defined typically as

$$F_{12} = \frac{2}{\pi xy}\left[\ln\sqrt{\frac{(1+x^2)(1+y^2)}{1+x^2+y^2}} + x\sqrt{1+y^2}\tan^{-1}\left(\frac{x}{\sqrt{1+y^2}}\right) + y\sqrt{1+x^2}\tan^{-1}\left(\frac{y}{\sqrt{1+x^2}}\right) - x\tan x^{-1} - y\tan y^{-1}\right], \tag{5.12}$$

where $x = \frac{a}{c}$ and $y = \frac{b}{c}$. The view factor for our device geometry of $a = 78\ \mu$m and $b = 10\ \mu$m is plotted for different gap distance in Fig.5.3b.

To quantitatively evaluate the experimental data, we calculated the gap thermal conductance based on the far-field radiative heat transfer theory, between Si opposing blocks and plotted with the experimental result as shown in Fig.5.4. We implemented the geometric view factor corresponding to our device geometry and the gap size derived from Fig.5.3b. The experimental data is well-fitted when Si emissivity is $\epsilon_{Si} = 0.7 \sim 0.9$. This result shows that the gap thermal conductance between Si-only device can be explained using the classical Planck's fa-field radiative heat transfer.

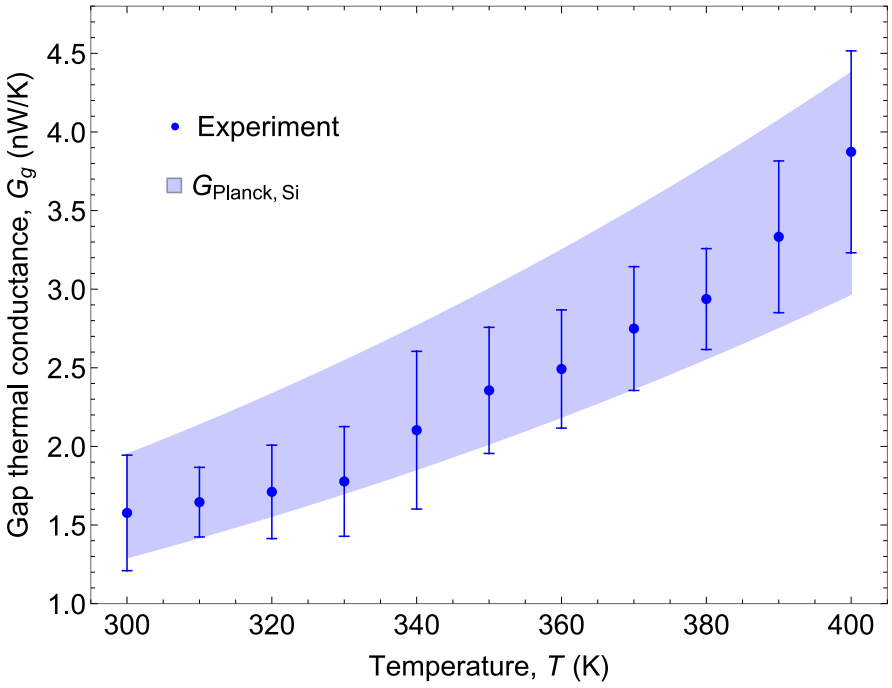

Figure5.4 Experimental gap thermal conductance for the device with only Si layer (blue circles), compared with that predicted by the far-field radiative heat transfer theory (lighter blue region).

5.2.3 Far-field radiative heat transfer between 3-layered bodies

Here, we show the calculation of the far-field radiative heat transfer between SiO_2/Si/SiO_2 3-layered structure, of which schematic image is displayed in Fig. 5.5a.

The exchanged heat flux is

$$\begin{aligned}(2A_1 + A_2)q_{123-456} &= (2A_1 + A_2)\left[q_{123-4} + q_{123-5} + q_{123-6}\right] \\ &= A_1\left[q_{14} + q_{15} + q_{16}\right] + A_2\left[q_{24} + q_{25} + q_{26}\right] + A_1\left[q_{34} + q_{35} + q_{36}\right] \\ &= 2A_1\left[q_{14} + q_{15} + q_{16}\right] + A_2\left[2q_{24} + q_{25}\right] \\ &= 2A_1\left[q_1 - q_{17}\right] + A_2\left[q_2 - q_{27}\right],\end{aligned} \tag{5.13}$$

since we assume $q_{11} = q_{12} = q_{13} = q_{21} = q_{22} = q_{23} = 0$, $q_{24} = q_{26}$, and $q_i = \sum_{j=1}^{N} q_{ij}$ is satisfied. The exchanged heat flux is defined as $q_{ij} = F_{ij}\left[\sigma\left(T_i^4 - T_j^4\right) + \left(\epsilon_j^{-1} - 1\right)q_j - \left(\epsilon_i^{-1} - 1\right)q_i\right]$, which describes q_{17} and q_{27} as

$$\begin{aligned}q_{17} &= F_{17}\left[\sigma\left(T_h^4 - T_{amb}^4\right) + \left(\epsilon_{evac}^{-1} - 1\right)q_7 - \left(\epsilon_1^{-1} - 1\right)q_1\right] = F_{17}\left[\sigma\left(T_h^4 - T_{amb}^4\right) - \left(\epsilon_1^{-1} - 1\right)q_1\right] \\ q_{27} &= F_{27}\left[\sigma\left(T_h^4 - T_{amb}^4\right) + \left(\epsilon_{evac}^{-1} - 1\right)q_7 - \left(\epsilon_2^{-1} - 1\right)q_2\right] = F_{27}\left[\sigma\left(T_h^4 - T_{amb}^4\right) - \left(\epsilon_2^{-1} - 1\right)q_2\right].\end{aligned} \tag{5.14}$$

Applying these q_{17} and q_{27} to Eq. 5.13 gives

$$q_{123-456} = \frac{2\left[1 + F_{17}\left(\epsilon_1^{-1} - 1\right)\right]q_1 + A_{21}\left[1 + F_{27}\left(\epsilon_2^{-1} - 1\right)\right]q_2 - \sigma\left(2F_{17} + A_{21}F_{27}\right)\left(T_h^4 - T_{amb}^4\right)}{2 + A_{21}}. \tag{5.15}$$

The heat flux $q_1, 2$ can be derived by solving Eq. 5.4, which is, in this case, as follows

$$\begin{bmatrix} \epsilon_1^{-1} & 0 & 0 & \chi_{14} & \chi_{15} & \chi_{16} & 0 \\ 0 & \epsilon_2^{-1} & 0 & \chi_{24} & \chi_{25} & \chi_{24} & 0 \\ 0 & 0 & \epsilon_1^{-1} & \chi_{16} & \chi_{15} & \chi_{14} & 0 \\ \chi_{14} & \chi_{15} & \chi_{16} & \epsilon_1^{-1} & 0 & 0 & 0 \\ \chi_{24} & \chi_{25} & \chi_{24} & 0 & \epsilon_2^{-1} & 0 & 0 \\ \chi_{16} & \chi_{15} & \chi_{14} & 0 & 0 & \epsilon_1^{-1} & 0 \\ \chi_{71} & \chi_{72} & \chi_{71} & \chi_{71} & \chi_{72} & \chi_{71} & 1 \end{bmatrix}\begin{bmatrix} q_1 \\ q_2 \\ q_3 \\ q_4 \\ q_5 \\ q_6 \\ q_7 \end{bmatrix} = \sigma\begin{bmatrix} \left(F_{14} + F_{15} + F_{16}\right)\left(T_h^4 - T_c^4\right) + F_{17}\left(T_h^4 - T_{amb}^4\right) \\ \left(2F_{24} + F_{25}\right)\left(T_h^4 - T_c^4\right) + F_{27}\left(T_h^4 - T_{amb}^4\right) \\ \left(F_{14} + F_{15} + F_{16}\right)\left(T_h^4 - T_c^4\right) + F_{17}\left(T_h^4 - T_{amb}^4\right) \\ -\left(F_{14} + F_{15} + F_{16}\right)\left(T_h^4 - T_c^4\right) + F_{17}\left(T_c^4 - T_{amb}^4\right) \\ -\left(2F_{24} + F_{25}\right)\left(T_h^4 - T_c^4\right) + F_{27}\left(T_c^4 - T_{amb}^4\right) \\ -\left(F_{14} + F_{15} + F_{16}\right)\left(T_h^4 - T_c^4\right) + F_{17}\left(T_c^4 - T_{amb}^4\right) \\ \left(2F_{71} + F_{72}\right)\left\{\left(T_h^4 - T_{amb}^4\right) + \left(T_c^4 - T_{amb}^4\right)\right\} \end{bmatrix}. \tag{5.16}$$

Please note that $\epsilon_{vac} = 1$, $\epsilon_1 = \epsilon_3 = \epsilon_4 = \epsilon_6$, and $\epsilon_2 = \epsilon_5$ and by assuming that $F_{ii} = 0$ and $F_{12} = F_{13} = F_{23} = F_{45} = F_{46} = F_{56} = 0$, the view factor matrix is

$$\begin{bmatrix} F_{11} & F_{12} & F_{13} & F_{14} & F_{15} & F_{16} & F_{17} \\ F_{21} & F_{22} & F_{23} & F_{24} & F_{25} & F_{26} & F_{27} \\ F_{31} & F_{32} & F_{33} & F_{34} & F_{35} & F_{36} & F_{37} \\ F_{41} & F_{42} & F_{43} & F_{44} & F_{45} & F_{46} & F_{47} \\ F_{51} & F_{52} & F_{53} & F_{54} & F_{55} & F_{56} & F_{57} \\ F_{61} & F_{62} & F_{63} & F_{64} & F_{65} & F_{66} & F_{67} \\ F_{71} & F_{72} & F_{73} & F_{74} & F_{75} & F_{76} & F_{77} \end{bmatrix} = \begin{bmatrix} 0 & 0 & 0 & F_{14} & F_{15} & F_{16} & F_{17} \\ 0 & 0 & 0 & F_{24} & F_{25} & F_{24} & F_{27} \\ 0 & 0 & 0 & F_{16} & F_{15} & F_{14} & F_{17} \\ F_{14} & F_{15} & F_{16} & 0 & 0 & 0 & F_{17} \\ F_{24} & F_{25} & F_{24} & 0 & 0 & 0 & F_{27} \\ F_{16} & F_{15} & F_{14} & 0 & 0 & 0 & F_{17} \\ F_{71} & F_{72} & F_{71} & F_{71} & F_{72} & F_{71} & F_{77} \end{bmatrix}. \tag{5.17}$$

Since $\sum_{j=1}^{N} F_{ij} = 1$ and $A_i F_{ij} = A_j F_{ji}$ are satisfied, as well as $A_1 = A_3 = A_4 = A_6 = ab$ and $A_2 = A_5 = ad$, the view factors between the device surfaces and the ambient surface can be written as

$$\begin{aligned} F_{17} &= 1 - F_{14} - F_{15} - F_{16}, \\ F_{27} &= 1 - F_{24} - F_{25} - F_{24} = 1 - 2F_{24} - F_{25}, \\ F_{77} &= 1 - 4F_{71} - 2F_{72} = 1 - 4A_{17}F_{17} - 2A_{27}F_{27}. \end{aligned} \tag{5.18}$$

All the view factors can be expressed by F_{14},F_{15},F_{16},F_{24} and/or F_{25}. The view factor F_{14} and F_{25} can be calculated according to Eq. 5.12 and other view factors can be derived by solving the view factors' algebra.

$$A_2 F_{24} = A_4 F_{42} = A_1 F_{15}, \tag{5.19}$$

$$\begin{aligned} (A_1 + A_2)F_{12-45} &= (A_1 + A_2)(F_{12-4} + F_{12-5}) \\ &= A_4 F_{4-12} + A_5 F_{5-12} \\ &= A_4(F_{41} + F_{42}) + A_5(F_{51} + F_{52}) \\ &= A_1(F_{14} + 2F_{15}) + A_2 F_{25}, \end{aligned} \tag{5.20}$$

$$\begin{aligned} (2A_1 + A_2)F_{123-456} &= (2A_1 + A_2)(F_{123-4} + F_{123-5} + F_{123-6}) \\ &= A_4 F_{4-123} + A_5 F_{5-123} + A_6 F_{6-123} \\ &= A_4(F_{41} + F_{42} + F_{43}) + A_5(F_{51} + F_{52} + F_{53}) + A_6(F_{61} + F_{62} + F_{63}) \\ &= 2A_1(F_{14} + 2F_{15} + F_{16}) + A_2 F_{25}. \end{aligned} \tag{5.21}$$

Therefore,

$$\begin{aligned} F_{24} &= A_{12} F_{15}, \\ F_{15} &= \frac{1}{2}\left[(1 + A_{21})F_{12-45} - A_{21}F_{25} - F_{14}\right], \end{aligned} \tag{5.22}$$

$$F_{15} = \frac{1}{2}\left[(1 + A_{21})F_{12-45} - A_{21}F_{25} - F_{14}\right], \tag{5.23}$$

$$F_{16} = \left(1 + \frac{A_{21}}{2}\right)F_{123-456} - (1 + A_{21})F_{12-45} - \frac{A_{21}}{2}F_{25}. \tag{5.24}$$

The view factors, F_{12-45} and $F_{123-456}$ can be also calculated from Eq. 5.12. The gap thermal conductance between SiO_2/Si/SiO_2 3-layered structure via far-field radiative heat transfer is finally,

$$G_{FFRHT,3-layer} = \frac{q_{123-456}}{T_h - T_c}. \tag{5.25}$$

In order to investigate the origin of the higher G_g for SiO_2/Si/SiO_2 three-layer system, we calculated the far-field radiative heat transfer between three-layer system ($G_{\text{Planck,3-layer}}$), accounting for the geometric view factors and assuming the emissivity of SiO_2 layer to be 1, to evaluate the maximum predicted G_g. The result is plotted in Fig. 5.5b in comparison with the experimental G_g. However, the elevation of the predicted $G_{\text{Planck,3-layer}}$ by having 2 additional SiO_2 layers was insufficient to fit the experimental G_g for three-layer system due to the small impact coming from more than $50 \sim 300$ times thinner SiO_2 layer than Si layer. It is clear from these data that the disagreement between the G_g for three-layer system and G_g of Si-only system cannot be explained by the classical far-field radiative heat transfer theory.

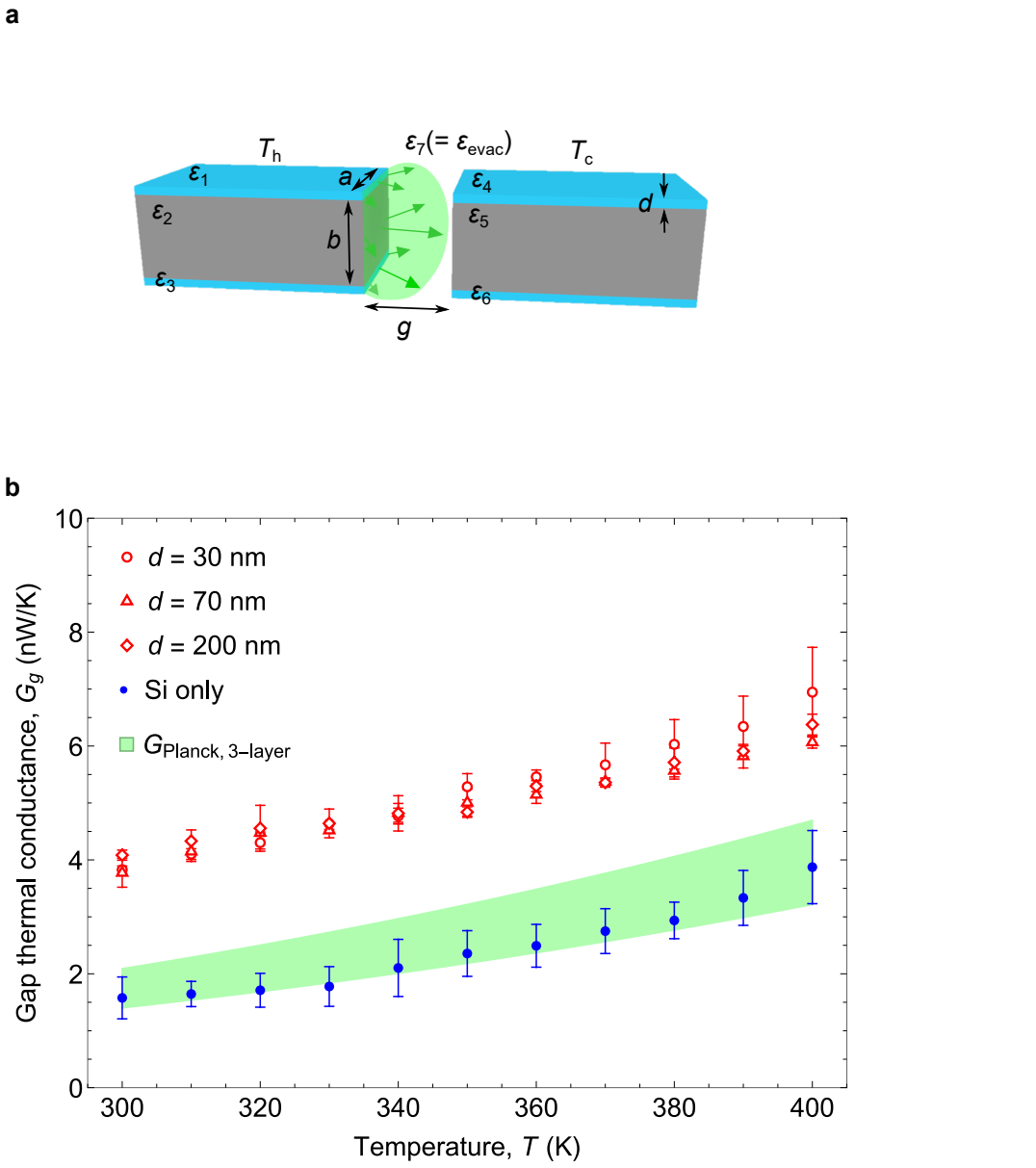

Figure5.5 **a** Schematic of the emitter and the receiver of 3-layered structure, exchanging heat flux. **b** Experimental gap thermal conductance for SiO_2/Si/SiO_2 three-layer system with SiO_2 thickness of 30, 70 and 200 nm, compared with that of only-Si layer device and the theoretical estimations of the far-field radiative heat transfer of three-layer system ($G_{\text{Planck,3-layer}}$) plotted in green zone. The theoretical calculation $G_{\text{Planck,3-layer}}$, derived with the maximum SiO_2 emissivity, is much smaller than the experimental G_g.

5.2.4 Near-field radiative heat transfer contribution to the measured gap conductance

To investigate heat exchanges due to other than the classical far-field radiative heat transfer, we evaluated the contribution of near-field effects. We calculated the near-field radiative heat transfer between infinite Si plates, separated by a vacuum gap of 10 μm. The heat transfer coefficient per unit area is [64, 3]:

$$h_{\mathrm{NF}} = \sum_{i=s,p} \int d\omega \int_{\frac{\omega}{c}}^{\infty} \frac{k}{2\pi^3} dk \frac{\partial}{\partial T} \left(\frac{\hbar\omega}{e^{\frac{\hbar\omega}{k_B T}} - 1} \right) \frac{\mathrm{Im}[r_{31}^i]\mathrm{Im}[r_{32}^i] e^{-2\mathrm{Im}[\gamma_3]d}}{\left| 1 - r_{31}^i r_{32}^i e^{2i\gamma_3 d} \right|^2}, \tag{5.26}$$

where s, p correspond to s- and p-polarization, 1,2 and 3 are for emitter, receiver and vacuum in between, respectively. Further, γ_3 is a cross-plane wave vector in vacuum, $r_{31,32}^i$ is Fresnel reflection factors. The G_g for evanescent wave through gap was calculated by the heat transfer coefficient derived above multiplied by the actual cross-section area for our device (Fig. 5.6). It is less than one order of magnitude lower than far-field radiative heat transfer between Si rectangular surfaces. Since it was calculated between infinite plates, actual near-field effects in our experiments can be predicted even lower. Therefore, the contribution of near-field radiative heat transfer to the measured G_g is negligible.

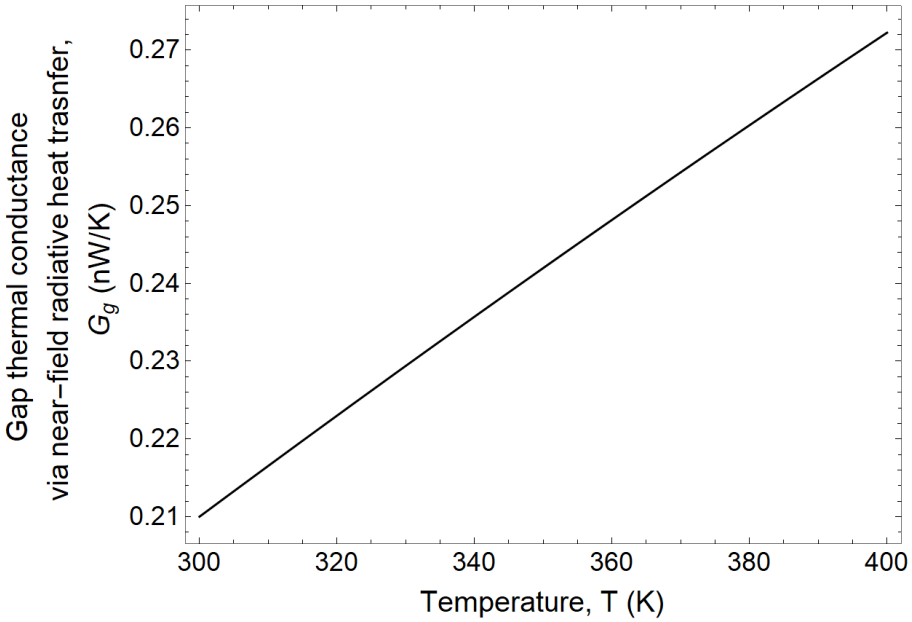

Figure5.6 The gap thermal conductance by near-field radiative heat transfer. The conductance was calculated between infinite Si plates separated by a vacuum gap of 10 μm

5.2.5 SPhP guided modes

To investigate the origin of the discrepancy between the measured G_g of the three-layer system and the measured G_g of the Si-only system, we analysed the SPhP energy propagation inside the three-layer system.

We first calculated wave vectors in the system (the details are discussed in the Chapter 2, the section 2.2). The relative permittivity of SiO_2 shown in Fig. 2.8 was used. Silicon has a constant and real permittivity of $\epsilon_{Si} = 11.7$. The relative permittivity in a vacuum, ϵ_{vac}, was set as unity. We defined the SPhP in-plane wave vector along the interfaces as a complex wave vector, $\beta = \beta_r + i\beta_i$ and the cross-plane wave vectors in each medium as p_{vac}, p_{SiO_2} and p_{Si}.

Once the Maxwell's equations with the proper boundary conditions are solved and the in-plane wave vector ($\beta = \beta_r + i\beta_i$) and the cross-plane wave vectors (p_{vac}, p_{SiO_2}, p_{Si}) are derived, electric fields and magnetic fields were expressed. We visualized the in-plane Poynting vectors inside the structure and compared with that inside the pristine Si film of 10-μ thickness as shown in Fig. 5.7 and Fig. 5.8.

We found that the in-plane Poynting vectors of three-layer system mainly exist inside Si layer, although SPhPs are excited by SiO_2 nanolayers. Remarkably, we also found that in-plane SPhP energy present guided resonant modes inside Si. The 1st branch has the largest amplitude, contributing the most to the energy transfer. The Poynting vector profile does not significantly differ for the Si film and the three-layer system with $d = 30$ nm and $d = 200$ nm. We calculated the dispersion relation and the propagation length spectrum in both configurations as reported in Fig. 5.9. In Fig. 5.9a, the coloured solid lines are the first to fifth modes in the three-layer system, and the dashed lines are the modes in the 10 μm-thick Si film. Figure 5.9a shows that the dispersion curves of the three-layer system match the ones of the silicon film except in the vicinity of the polariton resonances, where slight differences appear. The propagation length spectrum in the three-layer system reported in Fig. 5.9b reveals the basic difference between the pristine Si film and the three-layer system. While the Si film has negligible absorption (zero imaginary dielectric function), the three-layer system appears as significantly absorbing in the full spectrum. These results and also the arguments in Chapter2.6.1 indicate that, due to the thick Si layer, SPhPs project oblique waves inside Si layer and hybridize with the guided resonant modes inside Si layer. Since Si is non-absorptive, the thick Si layer act as a wave guide and most of the energy is distributed inside Si layer. Although this guided resonant modes exist also in pristine Si film, we have to note that the calculations of dispersion relation, absorption spectrum and in-plane Poynting vector were based on the assumption that there is an input of waves propagating along the interface.

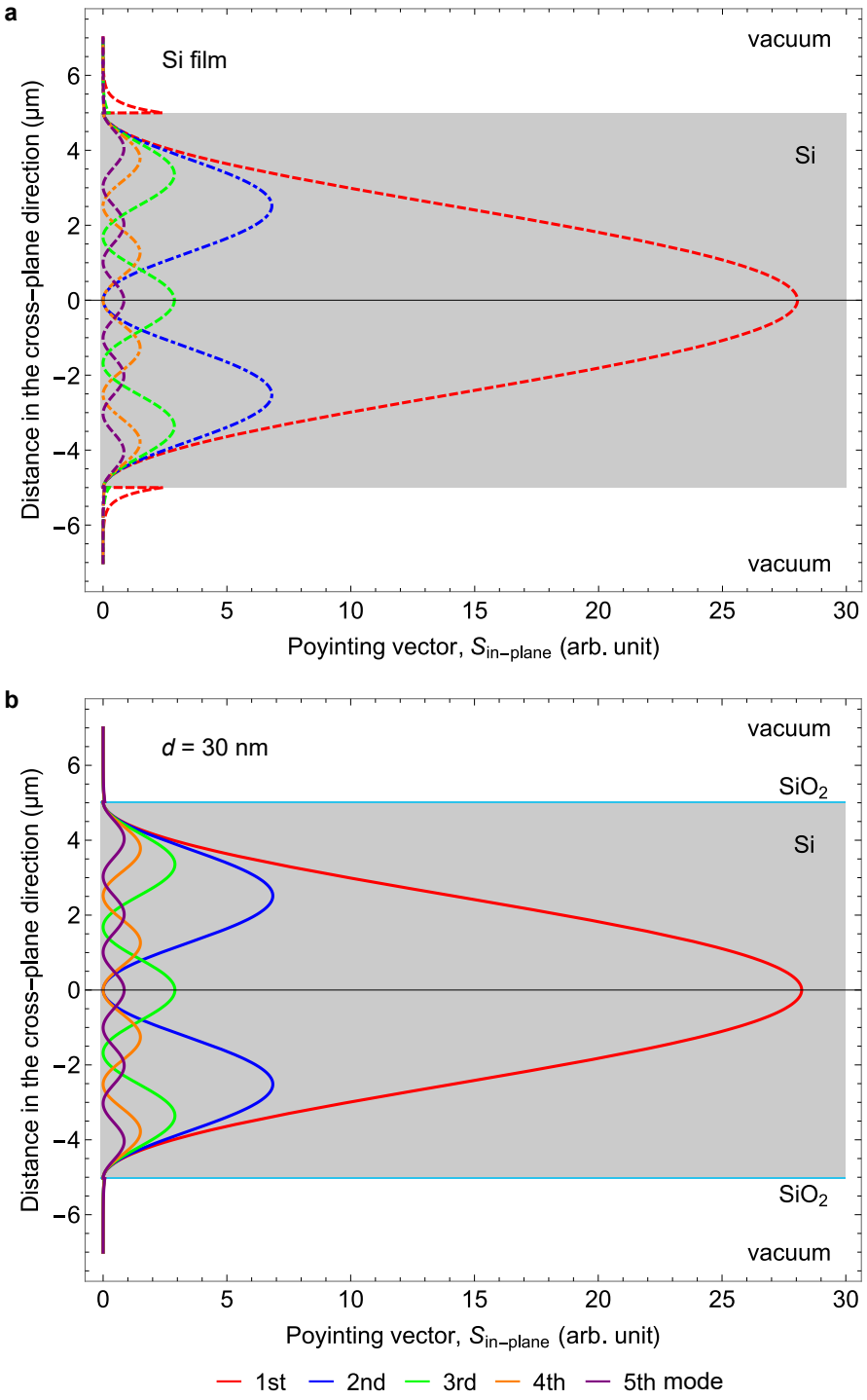

Figure5.7 Poynting vector in the in-plane direction. The Poynting vectors were calculated inside **a** the Si film and the three-layer system with **b** $d = 30$ nm. The calculations were done for the frequency $\omega = 203$ Trad/s, at which the SPhPs have the strongest cross-plane confinement.

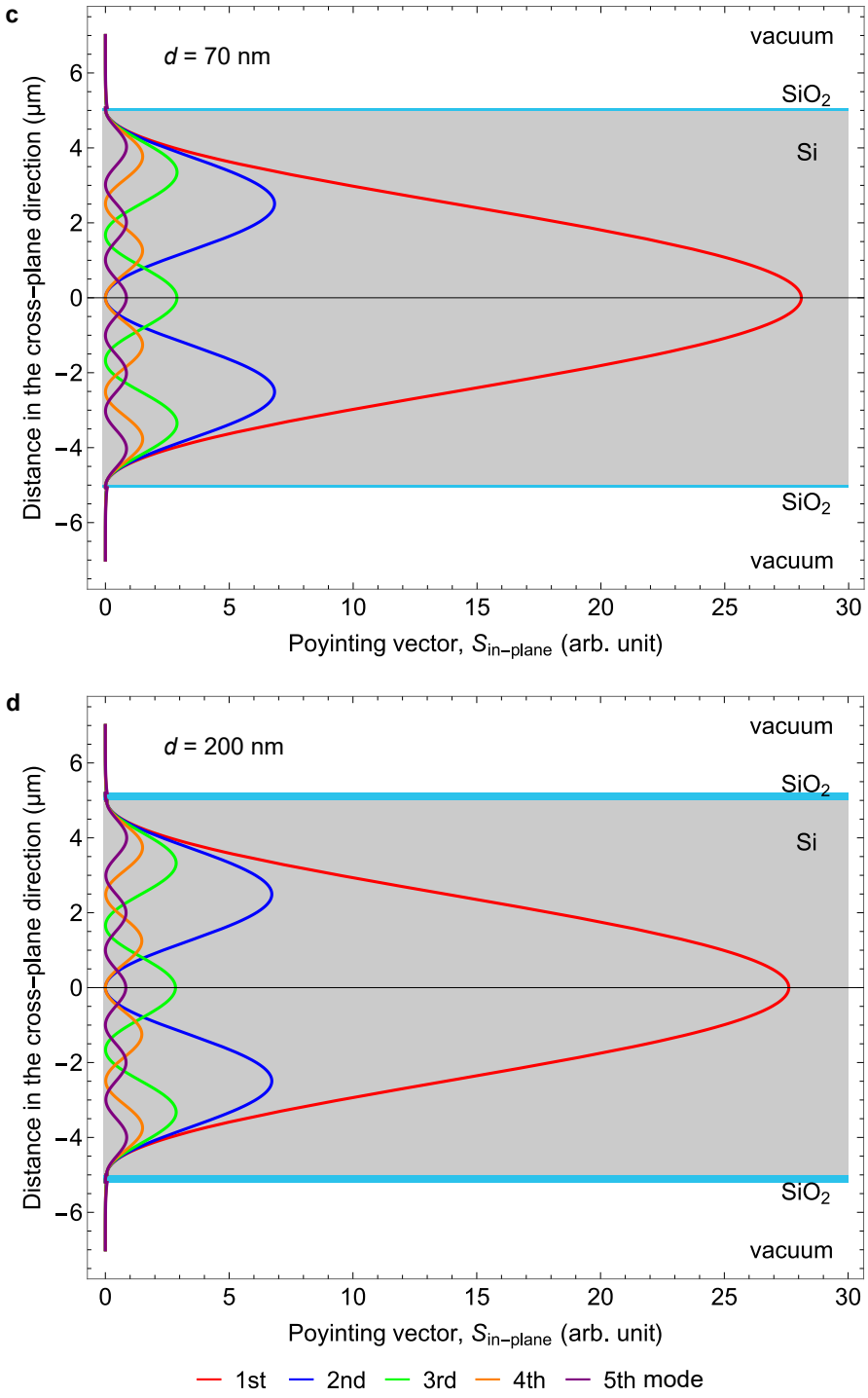

Figure5.8 Poynting vector in the in-plane direction. The Poynting vectors were calculated inside **c** d = 70 nm and **d** d = 200 nm. The calculations were done for the frequency ω = 203 Trad/s, at which the SPhPs have the strongest cross-plane confinement.

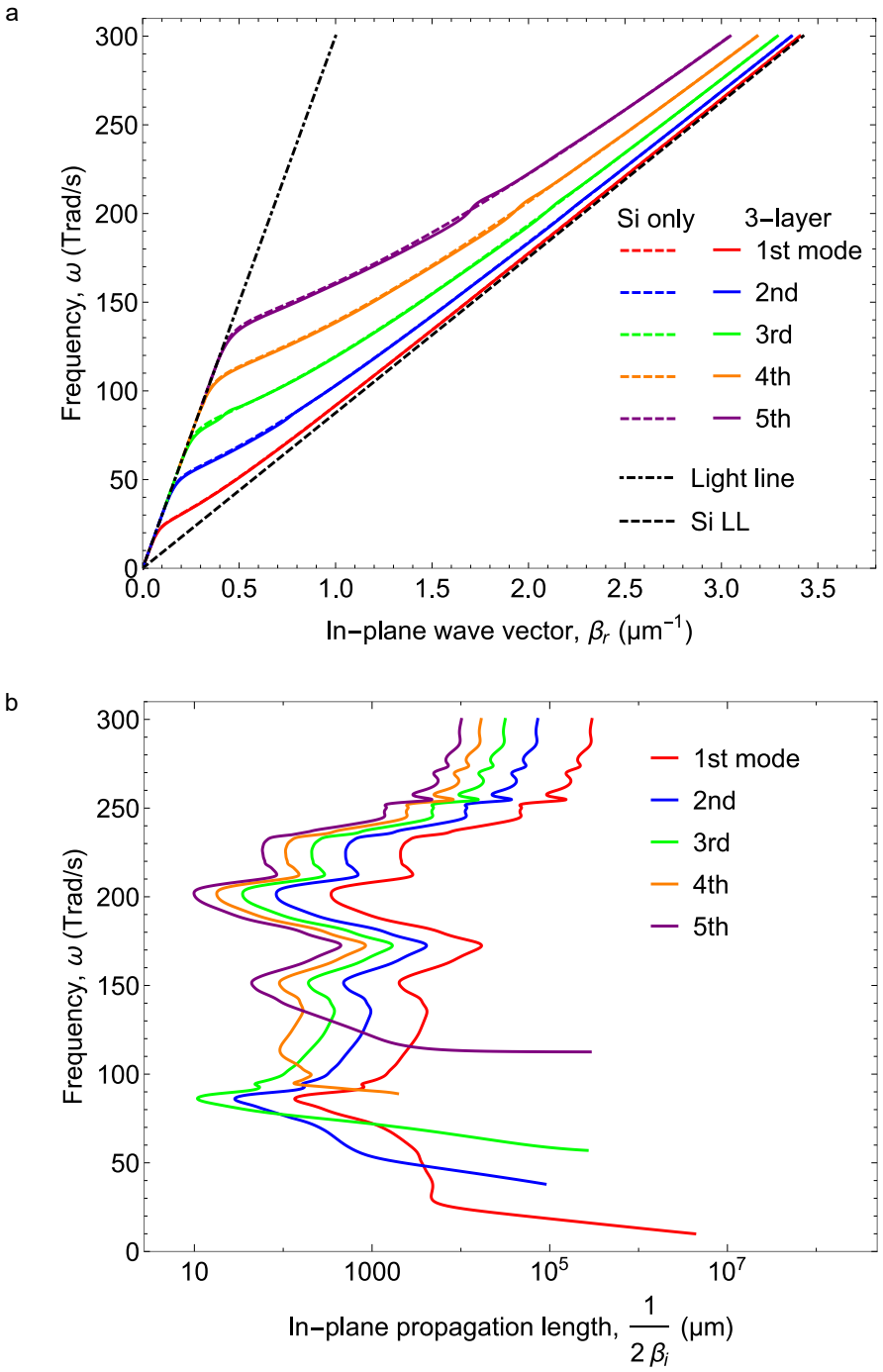

Figure5.9 The dispersion relation and the absorption spectrum of SPhPs inside the three-layer system. **a**, The dispersion relation of SPhPs wave vector in in-plane direction and **b**, the SPhPs in-plane propagation length calculated for the oxide thickness of d = 200 nm. The dashed lines in **a** are the guided resonant modes inside the 10 μm-thick silicon film.

However, in our experiments, those modes cannot be excited thermally without the presence of SiO_2 nanolayers which excite SPhPs that propagate along the interfaces. The guided resonant modes can only be thermally excited if absorption is large enough to couple heating to the electromagnetic field. Consequently, those modes are only contributing to the gap conductance when SiO_2 nanolayers are thermally activating them while remaining unexcited in the case of the non-absorbing pristine Si film. Figure 5.10 shows mapping of the in-plane Poynting vector outside the three-layer structure. The calculation was gained with FEM simulation using the software named "COMSOL". A plane wave was input into the edge of SiO_2 nanolayers. The density mapping shows that SPhP guided modes inside Si are emitted mainly into the in-plane direction.

According to the discussions above on SPhP guided modes inside the Si layer, propagating mainly in the in-plane direction, we consider the two-dimensional conductance of SPhP guided modes in the next subsection.

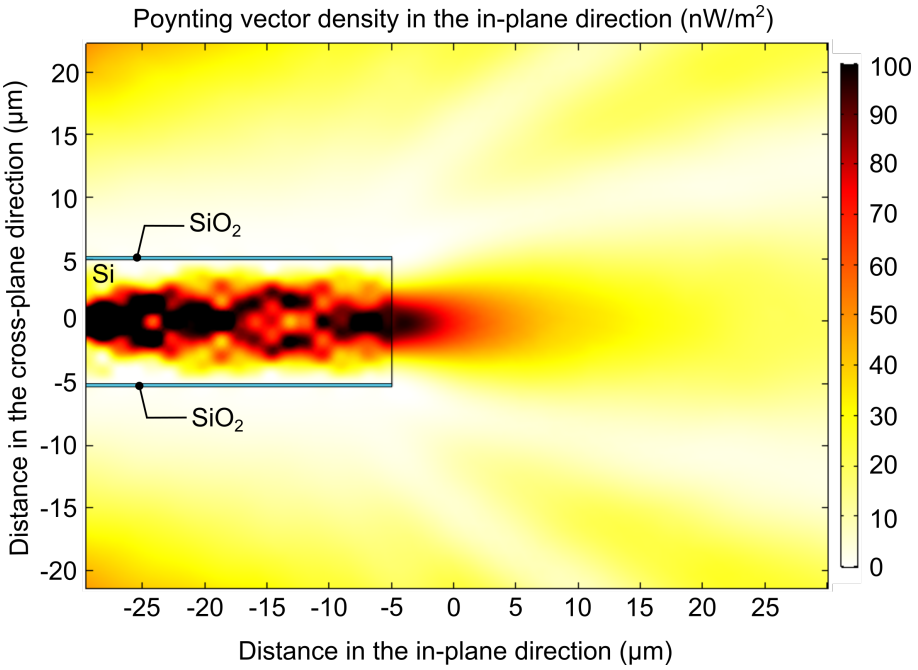

Figure5.10 Density mapping of SPhP in-plane energy. It shows how the electromagnetic flux is emitted from the hot plate along the in-plane direction mainly. The calculations were done for the frequency ω = 203 Trad/s, at which the SPhPs have the strongest cross-plane confinement.

5.2.6 Two-dimensional conductance of SPhP guided modes

To evaluate the gap conductance in the three-layer system, we consider, firstly, the contribution of Planck's radiation that was proven in the case of the pristine Si film. As explained above, a second contribution should be added to the gap conductance to take into account in-plane guided resonant modes that are thermally activated only in the case of the three-layer system.

To derive this second contribution, we take into account the wave vector space as shown in Fig.5.11.

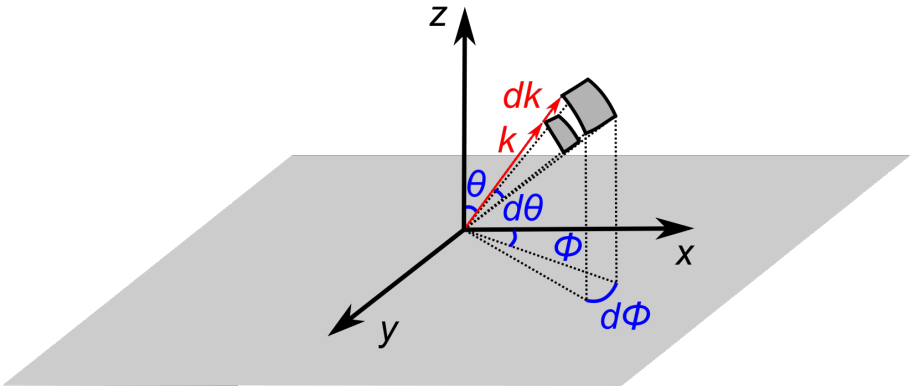

Figure5.11 Wave vector space. In our SPhP model, the radiation energy is assumed to propagate in x axis direction, $\theta = 0$.

We start with the definition of the heat flux as established by the classical theory of far-field radiation where only the in-plane azimuth angle ϕ is taken into account, as

$$dq = \frac{dE}{dydzdt} = \frac{dE}{dyBdt}, dE = \hbar\omega f(\omega) D(\omega) d\omega d\phi, \tag{5.27}$$

where B is the total thickness of the plate, $\hbar$ is the Planck's constant, ω the angular frequencies, $f(\omega)$ the Bose-Einstein distribution function and $D(\omega)$ the density of states. The density of states can be written as

$$D(\omega)d\omega d\phi = \frac{dxdydp^2}{h^2} = \frac{dxdydk^2}{(2\pi)^2} = \frac{dxdy}{(2\pi)^2} dk(kd\phi) = \frac{dxdy}{(2\pi c)^2} \omega d\omega d\phi, \tag{5.28}$$

where $p = \hbar k$ and $k = \frac{\omega}{c}$. By combining Eq. 5.28 and Eq. 5.27, the differential of the heat flux can be rewritten as

$$dq = \frac{dE}{dyBdx}\frac{dx}{dt} = \frac{dE}{dxdyB} c\cos\phi = \frac{\hbar\omega c}{B} f(\omega) \frac{\omega}{(2\pi c)^2} d\omega \cos\phi d\phi. \tag{5.29}$$

Integration of the above equation yields the heat flux as

$$q = \int_0^\infty \frac{\hbar c}{(2\pi c)^2 B}\omega^2 f(\omega)d\omega \int_{-\pi/2}^{\pi/2} \cos\phi d\phi = \frac{\sigma_{2D}}{B}T^3, \tag{5.30}$$

where $\sigma_{2D} = 4\zeta(3)\frac{k_B^3}{ch^2}$ W m^{-1}K^{-3}. Therefore, the gap thermal conductance in the in-plane direction which is our model for the gap thermal conductance of SPhP, G_{SPhP}, is

$$G_{\mathrm{SPhP}} = \frac{q}{T_\mathrm{h} - T_\mathrm{s}} = \frac{\epsilon\sigma_{2D}a(T_\mathrm{h}^3 - T_\mathrm{s}^3)}{T_\mathrm{h} - T_\mathrm{s}}, \tag{5.31}$$

where $\epsilon = \frac{\epsilon_{3\text{-layer}}}{F^{-1}+1-\epsilon_{3\text{-layer}}}$, a is the width of the plate, F refers to the view factor and $\epsilon_{3\text{-layer}}$ to the emissivity of the three-layer system.

We evaluated G_{SPhP} according to Eq. 5.31 with the view factor of $F = 0.9 - 1.0$. Since the energy was mainly distributed inside and emitted from the Si layer, we set $\epsilon_{3\text{-layer}} \approx \epsilon_{\mathrm{Si}} = 0.7 - 0.9$. The thermal radiation through the gap consists of the far-field radiation between the facing surfaces and of the radiation caused by SPhPs, which yields the following total thermal conductance through the gap.

$$G = G_{\text{Planck, 3-layer}} + G_{\mathrm{SPhPs}}. \tag{5.32}$$

We derived G by summing $G_{\text{Planck, 3-layer}}$ (shown as a green zone in Fig.5.5b) and G_{SPhP} as in Eq. 5.32, and plotted in Fig.5.12b as a red zone. The result shows that $G = G_{\text{Planck, 3-layer}} + G_{\mathrm{SPhPs}}$ is in a good agreement with the G_g obtained for three-layer system. It indicates that by exploiting the radiative heat transfer by SPhP guided modes, we can obtain the heat exchange beyond what can be predicted by the classical Planck's theory of far-field radiative heat transfer.

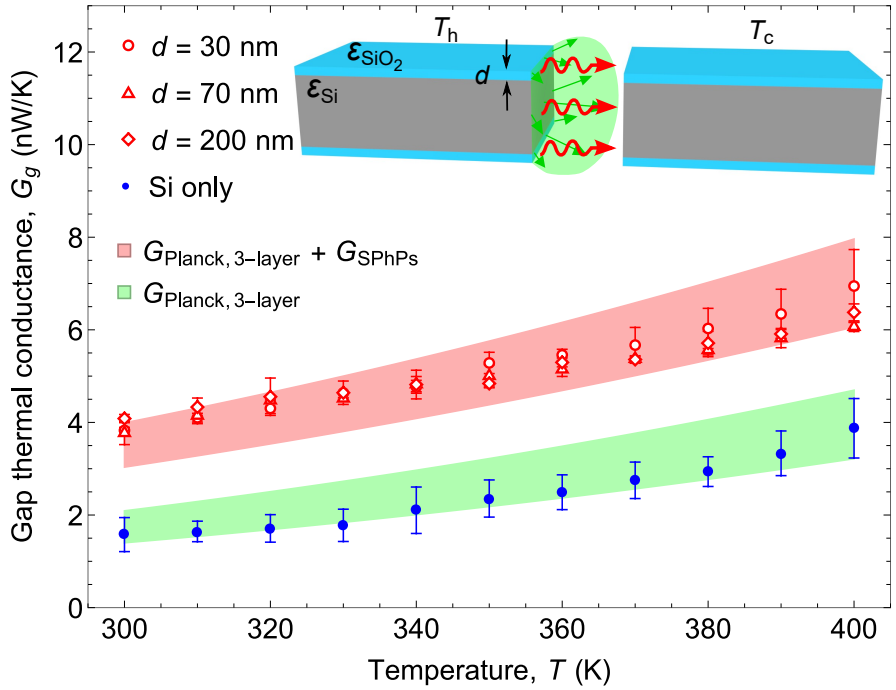

Figure5.12 Measured thermal conductance through the gap between two Si plates sandwiched with SiO_2 nanolayers (three-layer system), plotted with Eq. 5.32 for the gap thermal conductance of the three-layer system ($G_{Planck,\,3\text{-}layer}$+$G_{SPhP}$), shown in red zone. The view factor used in the calculation of G_{SPhP} was $F = 0.9 - 1.0$ to be appropriate for the in-plane propagation of SPhPs.

5.2.7 Influence of Pt resistors on SPhP propagation

We solved Maxwell's equation in the presence of the Pt layer of 100 nm thickness and calculated the in-plane Poynting vector, as shown in Fig. 5.13. Although the energy at the interface between the top SiO_2 and the Si layers are slightly higher due to the reflection at the Pt layer, the in-plane Poynting vectors with and without the Pt layer do not show the substantial difference. Thus, we confirmed that the influence of the Pt thermometer on the energy inside the three-layer structure is negligible.

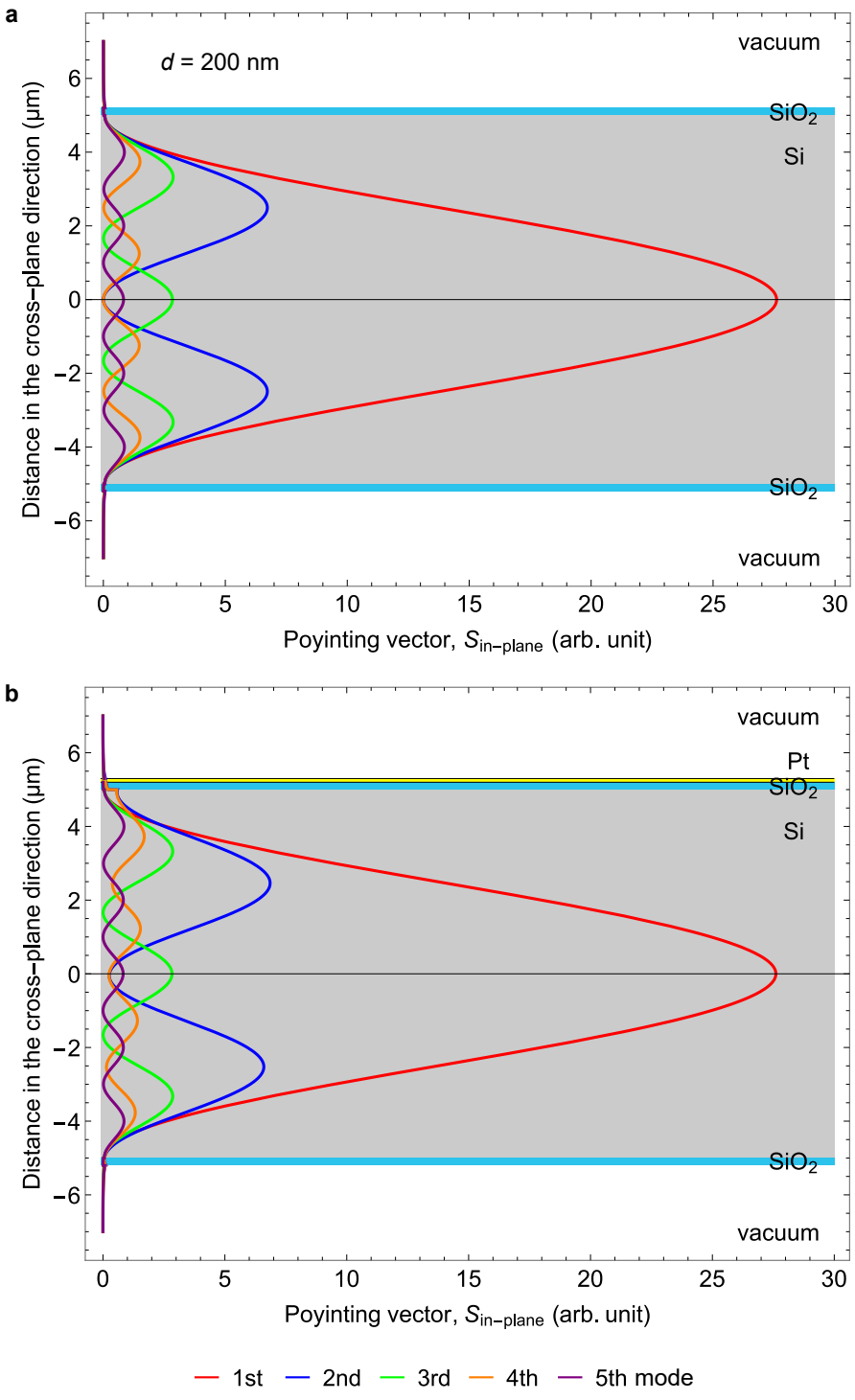

Figure5.13 Poynting vector in the in-plane direction inside the three-layer system **a** without and **b** with the Pt layer of 100 nm thickness

5.3 Conclusion

In this section, we measured the gap thermal conductance for SiO_2/Si/SiO_2 three-layer system and compared with that of the system with only Si layer. The result for the Si-only system met a good agreement with the conventional far-field radiative heat transfer prediction while the obtained conductance for the three-layer system was approximately twice higher than that of the Si-only system and beyond the prediction of the classical Planck's theory of far-field radiative heat transfer. We analysed the SPhP propagation inside the three-layer system and found that SPhPs excited inside the SiO_2 nanolayers hybridize with the resonant guided modes of thick Si and propagate mainly inside Si layer. This finding was counterintuitive because SPhP was believed to propagate only at the interface of absorptive materials. By implementing the two-dimensional conductance based on the results showing that SPhP guided modes mainly propagate in the in-plane direction, we could fit well the measured gap conductance of the three-layer system. The radiative heat exchange over the Planck's limit has been only possible with either the separation distance or dimensions of the bodies are smaller than the dominant wavelength, and the latter condition was experimentally achieved using absorbent materials which can excite SPhPs.

However in our work, we experimentally demonstrated that the super-Planckian far-field radiative heat transfer is possible with non-absorbent bodies just by coating them with an absorbent material, due to the SPhP guided modes. This outcome was derived with rathre simple geometry, and thus, will provide new insights to thermal management in semiconductor fields for wide applications.

Chapter 6

General conclusions and prospects

In our work, we studied SPhP propagation and thermal transport inside SiO_2/Si/SiO_2 three-layered system and how it can contribute to radiative heat transport.

In theoretical studies, we investigated dispersion relations and in-plane propagation length of SPhP in SiO_2/Si/SiO_2 three-layered system. As the SiO_2 layers become thinner, propagation length becomes longer due to less absorption within SiO_2 layers, thus higher thermal conductivity. We found that SPhP thermal conductance in SiO_2/Si (10 μm thick)/SiO_2 three-layered system can be higher than that of a single SiO_2 film when SiO_2 thickness is thicker than $\sim$ 150 nm. This is an interesting finding, since it has always been believed that the thinner the structure, the higher the SPhP thermal conductance. We also investigated Si thickness dependence and remarkably we found that there was a minimum propagation length, thus thermal conductivity when Si layer is thinner than $\sim$ 1 μm. Our simulation results indicated that for thicker Si, there exists propagative waves inside Si which is a projection of SPhPs generated in SiO_2 layers. This propagative waves inside Si couple with guided resonant modes of Si and result in efficient energy transport in in-plane direction. Once Si layer is thinner than half of a wavelength in Si, propagative waves can no longer exist and SPhPs generated in upper and lower SiO_2 layers couple only by evanescent components inside Si. They couple stronger as Si thickness decreases, causing the minimum in the in-plane thermal conductivity.

The SPhPs coupled with Si resonant guided modes play a very important role in radiative heat transfer as well. Most of in-plane SPhP energy is distributed inside the non-absorptive Si layer via SPhP guided resonant modes and is emitted mainly in in-plane direction.

This led to radiative heat transfer between SiO_2/Si (10 μm thick)/SiO_2 three-layered systems, overcoming the Planck's blackbody limit in the far-field regime.

This is remarkable since we showed that the in-plane SPhP propagation can still contribute to the super-Planckian radiative heat transfer when the geometry is a multilayer structure including

a thick non-absorbent material which does not excite SPhP.

We demonstrated that the super-Planckian radiative heat transfer is achievable with relatively simple and large structures thanks to SPhP guided modes, and this finding gives new insight to thermal management in semiconductor fields.

However, taking advantage of SPhP guided modes in thermal management applications, especially for efficient cooling of the local heat spot in transistors, still remains challenging. The gap thermal conductance of SPhP guided modes is only twice higher than the blackbody limit, and as for heat conduction inside the system, the absolute values of thermal conductance are orders of magnitude lower than the thermal conductivity of the bulk Si. This study is physically important and interesting, but still needs further improvements in an application point of view.

Though, another significance of this work is that SPhP worked as an input into the Si wave guide. Silicon slab used as a mid-infrared waveguide is a well-known technology in photonics [65, 66, 67, 68]. But, in their studies, Si slab is in nanometric size, and the input is by a laser. In contrast, our results showed that heat can excite SPhP in SiO_2 that can eventually act as an input into the Si wave guide. Heat is an incoherent energy that diffuse into the surrounding space in all direction. It is difficult to manage its directionality, unlike electrons and photons in electronics and photonics. Our work indicate that by converging the phonon heat energy into SPhP, we can exploit energy in electromagnetic form, and take advantage of well-established optics technology to broaden thermal management possibility.

Acknowledgement

My deep gratitude goes to my supervisor, Professor Masahiro Nomura, who supervised my study during the past years. I am grateful for his patient guidance and how he encouraged me to challenge myself in research and my career.

I would like to express my deep appreciation to Prof. Sebastian Volz for his thorough supervision. He showed me the new field of study and brought me to this level. I learned a lot and enjoyed the discussions with a cup of coffee in our hands.

I am grateful to Dr. Jose Ordonez-Miranda and Dr. Laurent Jalabert for their active guidance and research support during my Ph.D. Dr. Jose Ordonez-Miranda helped me a lot with the understanding of SPhP, and his passion always inspired me. Since my time in Fujita lab, Dr. Laurent Jalabert has always taken deep care regarding my research and my struggle in the lab. Our successful results could not have been accomplished without his consistent support.

I appreciate Prof. Hiroyuki Fujita for his deep care even after graduating from Fujita lab. His instructions, not only on the research itself but also on how to conduct research and keep looking out to open perspectives, enriched my experiences during the beginning of the researcher path.

I am also grateful to Prof. Hiroshi Toshiyoshi and his lab members: Mr. Manabu Ataka, Dr. Hiroaki Honma, Ms. Hiroko Koizumi, Mr. Yukiya Tohyama, and others. Prof. Toshiyoshi always cared about me, although I was not his student. I appreciate how he listened to my problems and gave advice to me. Thanks to Ataka san and Honma san, I could learn complete fabrication techniques and their support enabled me to use their facilities comfortably. Koizumi san's warm care and her wise daughters always healed my heart. Thank Tohyama kun, for helping me with JSPS applications and other members to accept me in their facility and office.

My gratitude also goes to Prof. Teru Okitsu, Prof. Momoko Kumemura, Dr. Yuki Takayama, and Ms. Minako Makino, who supported me and have been affectionate to me since my master course in Fujita lab. Prof. Okitsu and Prof. Kumemrura's support was inevitable to maintain my mental.

I want to thank Dr. Wang-Ting Chiu, Dr. Stephany Nishikawa, Dr. Shu Okumura, Dr. Nicolas

Lobato-Dauzier, and Dr. Samar Emara for always being cheerful, enthusiastic, motivated, and stimulating Ph.D. friends. It is my precious memory to fight in difficult situations with them.

I would like to thank all the members from Nomura lab for helping me in laboratory life. Dr. Ryoto Yanagisawa, Sota Koike, Noboru Okamoto, Dr. Zhongwei Zhang helped me with research and let me have a comfortable stay in Nomura lab. I appreciate Dr. Sergei Gluchko, Dr. Yangyu Guo, and Dr. Byunggi Kim for all the constructive advice and fruitful discussions.

Last but not least, I want to thank my family, Dr. Chikako Sano, Dr. Roman Anufriev, and Dr. Yunhui Wu, for supporting me mentally and for their kind care. Thanks to them creating a warm environment for me to enjoy the time in my Ph.D., I could overcome various obstacles and continue to conduct my research.

Bibliography

[1] B. Song, A. Fiorino, E. Meyhofer, and P. Reddy, "Near-field radiative thermal transport: From theory to experiment," *AIP advances*, vol. 5, no. 5, p. 053503, 2015.

[2] S. Basu, B. J. Lee, and Z. M. Zhang, "Near-Field Radiation Calculated With an Improved Dielectric Function Model for Doped Silicon," *Journal of Heat Transfer*, vol. 132, no. 2, Feb. 2010. [Online]. Available: https://asmedigitalcollection.asme.org/heattransfer/article/132/2/023302/467868/Near-Field-Radiation-Calculated-With-an-Improved

[3] J.-P. Mulet, K. Joulain, R. Carminati, and J.-J. Greffet, "Enhanced radiative heat transfer at nanometric distances," *Microscale Thermophysical Engineering*, vol. 6, no. 3, pp. 209–222, 2002.

[4] B. Song, D. Thompson, A. Fiorino, Y. Ganjeh, P. Reddy, and E. Meyhofer, "Radiative heat conductances between dielectric and metallic parallel plates with nanoscale gaps," *Nature nanotechnology*, vol. 11, no. 6, pp. 509–514, 2016.

[5] A. Fiorino, L. Zhu, D. Thompson, R. Mittapally, P. Reddy, and E. Meyhofer, "Nanogap near-field thermophotovoltaics," *Nature nanotechnology*, vol. 13, no. 9, pp. 806–811, 2018.

[6] K. Ito, K. Nishikawa, A. Miura, H. Toshiyoshi, and H. Iizuka, "Dynamic modulation of radiative heat transfer beyond the blackbody limit," *Nano letters*, vol. 17, no. 7, pp. 4347–4353, 2017.

[7] J.-J. Greffet, R. Carminati, K. Joulain, J.-P. Mulet, S. Mainguy, and Y. Chen, "Coherent emission of light by thermal sources," *Nature*, vol. 416, no. 6876, p. 61, 2002.

[8] E. Rephaeli, A. Raman, and S. Fan, "Ultrabroadband photonic structures to achieve high-performance daytime radiative cooling," *Nano letters*, vol. 13, no. 4, pp. 1457–1461, 2013.

[9] D.-Z. A. Chen, A. Narayanaswamy, and G. Chen, "Surface phonon-polariton mediated thermal conductivity enhancement of amorphous thin films," *Physical Review B*, vol. 72, no. 15, p. 155435, Oct. 2005. [Online]. Available: https://link.aps.org/doi/10.1103/PhysRevB.72.155435

[10] J. Ordonez-Miranda, L. Tranchant, T. Tokunaga, B. Kim, B. Palpant, Y. Chalopin,

T. Antoni, and S. Volz, "Anomalous thermal conductivity by surface phonon-polaritons of polar nano thin films due to their asymmetric surrounding media," *Journal of Applied Physics*, vol. 113, no. 8, p. 084311, Feb. 2013. [Online]. Available: https://aip.scitation.org/doi/10.1063/1.4793498

[11] J. Ordonez-Miranda, L. Tranchant, Y. Chalopin, T. Antoni, and S. Volz, "Thermal conductivity of nano-layered systems due to surface phonon-polaritons," *Journal of Applied Physics*, vol. 115, no. 5, p. 054311, Feb. 2014. [Online]. Available: http://aip.scitation.org/doi/10.1063/1.4864430

[12] E. D. Palik, *Handbook of optical constants of solids*. Orlando: Academic Press, 1985, oCLC: 11068280.

[13] S. Tachikawa, J. Ordonez-Miranda, Y. Wu, L. Jalabert, R. Anufriev, S. Volz, and M. Nomura, "High surface phonon-polariton in-plane thermal conductance along coupled films," *Nanomaterials*, vol. 10, no. 7, p. 1383, 2020.

[14] R. Anufriev, S. Gluchko, S. Volz, and M. Nomura, "Quasi-ballistic heat conduction due to levy phonon flights in silicon nanowires," *ACS nano*, vol. 12, no. 12, pp. 11 928–11 935, 2018.

[15] Y. Wu, J. Ordonez-Miranda, S. Gluchko, R. Anufriev, D. D. S. Meneses, L. Del Campo, S. Volz, and M. Nomura, "Enhanced thermal conduction by surface phonon-polaritons," *Science Advances*, vol. 6, no. 40, p. eabb4461, 2020.

[16] L. Tranchant, S. Hamamura, J. Ordonez-Miranda, T. Yabuki, A. Vega-Flick, F. Cervantes-Alvarez, J. J. Alvarado-Gil, S. Volz, and K. Miyazaki, "Two-dimensional phonon polariton heat transport," *Nano letters*, vol. 19, no. 10, pp. 6924–6930, 2019.

[17] S. Shin, M. Elzouka, R. Prasher, and R. Chen, "Far-field coherent thermal emission from polaritonic resonance in individual anisotropic nanoribbons," *Nature communications*, vol. 10, no. 1, pp. 1–11, 2019.

[18] D. Thompson, L. Zhu, R. Mittapally, S. Sadat, Z. Xing, P. McArdle, M. M. Qazilbash, P. Reddy, and E. Meyhofer, "Hundred-fold enhancement in far-field radiative heat transfer over the blackbody limit," *Nature*, vol. 561, no. 7722, pp. 216–221, 2018.

[19] C. Craigie, T. Sheehan, V. Johnson, S. Burkett, A. J. Moll, and W. Knowlton, "Polymer thickness effects on bosch etch profiles," *Journal of Vacuum Science & Technology B: Microelectronics and Nanometer Structures Processing, Measurement, and Phenomena*, vol. 20, no. 6, pp. 2229–2232, 2002.

[20] F. J. B. Joseph, "Théorie analytique de la Chaleur," Tech. Rep., 1822. [Online]. Available: https://www3.nd.edu/{~}powers/ame.20231/fourier1878.pdf

[21] D. G. Cahill, W. K. Ford, K. E. Goodson, G. D. Mahan, A. Majumdar, H. J. Maris, R. Merlin,

and S. R. Phillpot, "Nanoscale thermal transport," *Journal of applied physics*, vol. 93, no. 2, pp. 793–818, 2003.

[22] K. E. Goodson, "Thermal Conduction in onhomogeneous. CVD eamond Layers =n Electronic Microstructures," Tech. Rep., 1996. [Online]. Available: http://www.asme.org/terms/Terms{_}Use.cfm

[23] T. Zeng and G. Chen, "Phonon Heat Conduction in Thin Films: Impacts of Thermal Boundary Resistance and Internal Heat Generation," *Journal of Heat Transfer*, vol. 123, no. 2, p. 340, apr 2001. [Online]. Available: http://heattransfer.asmedigitalcollection.asme.org/article.aspx?articleid=1444834

[24] K. Joulain, J.-P. Mulet, F. Marquier, R. Carminati, and J.-J. Greffet, "Surface Electromagnetic Waves Thermally Excited: Radiative Heat Transfer, Coherence Properties and Casimir Forces Revisited in the Near Field," apr 2005. [Online]. Available: http://arxiv.org/abs/physics/0504068http://dx.doi.org/10.1016/j.surfrep.2004.12.002

[25] E. Rousseau, A. Siria, G. Jourdan, S. Volz, F. Comin, J. Chevrier, and J.-J. Greffet, "Radiative heat transfer at the nanoscale," *Nature Photonics*, vol. 3, no. 9, pp. 514–517, sep 2009. [Online]. Available: http://www.nature.com/articles/nphoton.2009.144

[26] L. Worbes, D. Hellmann, and A. Kittel, "Enhanced near-field heat flow of a monolayer dielectric island," *Physical review letters*, vol. 110, no. 13, p. 134302, 2013.

[27] A. Narayanaswamy, S. Shen, and G. Chen, "Near-field radiative heat transfer between a sphere and a substrate," *Physical Review B*, vol. 78, no. 11, p. 115303, 2008.

[28] S. Shen, A. Narayanaswamy, and G. Chen, "Surface phonon polaritons mediated energy transfer between nanoscale gaps," *Nano letters*, vol. 9, no. 8, pp. 2909–2913, 2009.

[29] K. Kim, B. Song, V. Fernández-Hurtado, W. Lee, W. Jeong, L. Cui, D. Thompson, J. Feist, M. H. Reid, F. J. García-Vidal, *et al.*, "Radiative heat transfer in the extreme near field," *Nature*, vol. 528, no. 7582, pp. 387–391, 2015.

[30] B. Song, Y. Ganjeh, S. Sadat, D. Thompson, A. Fiorino, V. Fernández-Hurtado, J. Feist, F. J. Garcia-Vidal, J. C. Cuevas, P. Reddy, *et al.*, "Enhancement of near-field radiative heat transfer using polar dielectric thin films," *Nature nanotechnology*, vol. 10, no. 3, pp. 253–258, 2015.

[31] L. Hu, A. Narayanaswamy, X. Chen, and G. Chen, "Near-field thermal radiation between two closely spaced glass plates exceeding planck' s blackbody radiation law," *Applied Physics Letters*, vol. 92, no. 13, p. 133106, 2008.

[32] M. Lim, S. S. Lee, and B. J. Lee, "Near-field thermal radiation between doped silicon plates at nanoscale gaps," *Physical Review B*, vol. 91, no. 19, p. 195136, 2015.

[33] R. St-Gelais, L. Zhu, S. Fan, and M. Lipson, "Near-field radiative heat transfer between

parallel structures in the deep subwavelength regime," *Nature nanotechnology*, vol. 11, no. 6, pp. 515–519, 2016.

[34] M. Lim, J. Song, S. S. Lee, and B. J. Lee, "Tailoring near-field thermal radiation between metallo-dielectric multilayers using coupled surface plasmon polaritons," *Nature communications*, vol. 9, no. 1, pp. 1–9, 2018.

[35] J. DeSutter, L. Tang, and M. Francoeur, "A near-field radiative heat transfer device," *Nature nanotechnology*, vol. 14, no. 8, pp. 751–755, 2019.

[36] D.-Z. A. Chen, A. Narayanaswamy, and G. Chen, "Surface phonon-polariton mediated thermal conductivity enhancement of amorphous thin films," *Physical Review B*, vol. 72, no. 15, p. 155435, 2005.

[37] J. Ordonez-Miranda, L. Tranchant, T. Tokunaga, B. Kim, B. Palpant, Y. Chalopin, T. Antoni, and S. Volz, "Anomalous thermal conductivity by surface phonon-polaritons of polar nano thin films due to their asymmetric surrounding media," *Journal of Applied Physics*, vol. 113, no. 8, p. 084311, 2013.

[38] K. Park, S. Basu, W. King, and Z. Zhang, "Performance analysis of near-field thermophotovoltaic devices considering absorption distribution," *Journal of Quantitative Spectroscopy and Radiative Transfer*, vol. 109, no. 2, pp. 305–316, 2008.

[39] Y. Yang, S. Basu, and L. Wang, "Vacuum thermal switch made of phase transition materials considering thin film and substrate effects," *Journal of Quantitative Spectroscopy and Radiative Transfer*, vol. 158, pp. 69–77, 2015.

[40] A. Barker Jr, H. Verleur, and H. Guggenheim, "Infrared optical properties of vanadium dioxide above and below the transition temperature," *Physical Review Letters*, vol. 17, no. 26, p. 1286, 1966.

[41] F. Yang, J. R. Sambles, and G. W. Bradberry, "Long-range surface modes supported by thin films," *Phys. Rev. B*, vol. 44, pp. 5855–5872, Sep 1991. [Online]. Available: http://link.aps.org/doi/10.1103/PhysRevB.44.5855

[42] D.-Z. A. Chen and G. Chen, "_USHeat flow in thin films via surface phonon-polaritons," *_USFrontiers in Heat and Mass Transfer (FHMT)*, vol. 1.2, Jan. 2010. [Online]. Available: https://dspace.mit.edu/handle/1721.1/65086

[43] A. J. Huber, B. Deutsch, L. Novotny, and R. Hillenbrand, "Focusing of surface phonon polaritons," *Applied Physics Letters*, vol. 92, no. 20, p. 203104, May 2008. [Online]. Available: https://aip.scitation.org/doi/10.1063/1.2930681

[44] M. Francoeur, M. P. Mengüç, and R. Vaillon, "Local density of electromagnetic states within a nanometric gap formed between two thin films supporting surface phonon polaritons," *Journal of Applied Physics*, vol. 107, no. 3, p. 034313, Feb. 2010. [Online].

Available: https://aip.scitation.org/doi/full/10.1063/1.3294606

[45] K. Joulain, Y. Ezzahri, J. Drevillon, B. Rousseau, and D. D. S. Meneses, "Radiative thermal rectification between SiC and SiO_2," *Optics Express*, vol. 23, no. 24, pp. A1388–A1397, Nov. 2015. [Online]. Available: https://www.osapublishing.org/oe/abstract.cfm?uri=oe-23-24-A1388

[46] S. Gluchko, J. Ordonez-Miranda, L. Tranchant, T. Antoni, and S. Volz, "Focusing of surface phonon-polaritons along conical and wedge polar nanostructures," *Journal of Applied Physics*, vol. 118, no. 6, p. 064301, Aug. 2015. [Online]. Available: https://aip.scitation.org/doi/full/10.1063/1.4928207

[47] S. Gluchko, B. Palpant, S. Volz, R. Braive, and T. Antoni, "Thermal excitation of broadband and long-range surface waves on SiO2 submicron films," *Applied Physics Letters*, vol. 110, no. 26, p. 263108, June 2017. [Online]. Available: https://aip.scitation.org/doi/10.1063/1.4989830

[48] D.-Z. A. Chen and G. Chen, "Measurement of silicon dioxide surface phonon-polariton propagation length by attenuated total reflection," *Applied Physics Letters*, vol. 91, no. 12, p. 121906, Sept. 2007. [Online]. Available: https://aip.scitation.org/doi/10.1063/1.2789177

[49] B. Zhao and Z. Zhang, "Enhanced photon tunneling by surface plasmon–phonon polaritons in graphene/hbn heterostructures," *Journal of Heat Transfer*, vol. 139, no. 2, 2017.

[50] Q. Zhang, Z. Zhen, Y. Yang, G. Gan, D. Jariwala, and X. Cui, "Hybrid phonon-polaritons at atomically-thin van der waals heterointerfaces for infrared optical modulation," *Optics express*, vol. 27, no. 13, pp. 18 585–18 600, 2019.

[51] A. Y. Nikitin, E. Yoxall, M. Schnell, S. Vélez, I. Dolado, P. Alonso-Gonzalez, F. Casanova, L. E. Hueso, and R. Hillenbrand, "Nanofocusing of hyperbolic phonon polaritons in a tapered boron nitride slab," *ACS Photonics*, vol. 3, no. 6, pp. 924–929, 2016.

[52] J. Yang, M. Mayyas, J. Tang, M. B. Ghasemian, H. Yang, K. Watanabe, T. Taniguchi, Q. Ou, L. H. Li, Q. Bao, *et al.*, "Boundary-induced auxiliary features in scattering-type near-field fourier transform infrared spectroscopy," *ACS nano*, vol. 14, no. 1, pp. 1123–1132, 2019.

[53] M. Lim, J. Ordonez-Miranda, S. S. Lee, B. J. Lee, and S. Volz, "Thermal-Conductivity Enhancement by Surface Electromagnetic Waves Propagating along Multilayered Structures with Asymmetric Surrounding Media," *Physical Review Applied*, vol. 12, no. 3, p. 034044, Sept. 2019. [Online]. Available: https://link.aps.org/doi/10.1103/PhysRevApplied.12.034044

[54] C. Kittel, "Introduction to solid state physics," 1976.

[55] D.-Z. A. Chen, A. Narayanaswamy, and G. Chen, "Surface phonon-polariton mediated thermal conductivity enhancement of amorphous thin films," *Phys. Rev. B*, vol. 72,

p. 155435, Oct 2005. [Online]. Available: http://link.aps.org/doi/10.1103/PhysRevB.72.155435

[56] C. Yeh and F. I. Shimabukuro, *The Essence of Dielectric Waveguides*. Boston, MA: Springer US, 2008. [Online]. Available: http://link.springer.com/10.1007/978-0-387-49799-0

[57] F. Yang, J. R. Sambles, and G. W. Bradberry, "Long-range surface modes supported by thin films," *Physical Review B*, vol. 44, no. 11, pp. 5855–5872, sep 1991. [Online]. Available: https://link.aps.org/doi/10.1103/PhysRevB.44.5855

[58] A. Vega-Flick, R. A. Duncan, J. K. Eliason, J. Cuffe, J. A. Johnson, J.-P. Peraud, L. Zeng, Z. Lu, A. A. Maznev, E. N. Wang, *et al.*, "Thermal transport in suspended silicon membranes measured by laser-induced transient gratings," *AIP advances*, vol. 6, no. 12, p. 121903, 2016.

[59] D. G. Cahill, "Thermal conductivity measurement from 30 to 750 k: the 3ω method," *Review of scientific instruments*, vol. 61, no. 2, pp. 802–808, 1990.

[60] S.-A. Biehs and P. Ben-Abdallah, "Revisiting super-planckian thermal emission in the far-field regime," *Physical Review B*, vol. 93, no. 16, p. 165405, 2016.

[61] V. Fernández-Hurtado, A. I. Fernández-Domínguez, J. Feist, F. J. García-Vidal, and J. C. Cuevas, "Super-planckian far-field radiative heat transfer," *Physical Review B*, vol. 97, no. 4, p. 045408, 2018.

[62] D. Thompson, L. Zhu, E. Meyhofer, and P. Reddy, "Nanoscale radiative thermal switching via multi-body effects," *Nature nanotechnology*, vol. 15, no. 2, pp. 99–104, 2020.

[63] I. Lienhard and H. John, *A heat transfer textbook*. phlogiston press, 2005.

[64] D. Polder and M. Van Hove, "Theory of radiative heat transfer between closely spaced bodies," *Physical Review B*, vol. 4, no. 10, p. 3303, 1971.

[65] G. Z. Mashanovich, M. M. Milošević, M. Nedeljkovic, N. Owens, B. Xiong, E. J. Teo, and Y. Hu, "Low loss silicon waveguides for the mid-infrared," *Optics Express*, vol. 19, no. 8, pp. 7112–7119, 2011.

[66] M. M. Milošević, M. Nedeljkovic, T. M. Ben Masaud, E. Jaberansary, H. M. Chong, N. G. Emerson, G. T. Reed, and G. Z. Mashanovich, "Silicon waveguides and devices for the mid-infrared," *Applied physics letters*, vol. 101, no. 12, p. 121105, 2012.

[67] B. Dong, X. Guo, C. P. Ho, B. Li, H. Wang, C. Lee, X. Luo, and G.-Q. Lo, "Silicon-on-insulator waveguide devices for broadband mid-infrared photonics," *IEEE Photonics Journal*, vol. 9, no. 3, pp. 1–10, 2017.

[68] M. He, S. I. Halimi, T. G. Folland, S. S. Sunku, S. Liu, J. H. Edgar, D. N. Basov, S. M. Weiss, and J. D. Caldwell, "Guided mid-ir and near-ir light within a hybrid hyperbolic-material/silicon waveguide heterostructure," *Advanced Materials*, vol. 33, no. 11, p. 2004305, 2021.

Publication list

Journal paper

1. S. Tachikawa, J. Ordonez-Miranda, Y. Wu, L. Jalabert, R. Anufriev, S. Volz, M. Nomura, ”High surface phonon-polariton in-plane thermal conductance along coupled films”, Nanomaterials, 10(7), 1383. 2020
2. S. Tachikawa, J. Ordonez-Miranda, L. Jalabert, Y. Wu, Y. Guo, R. Anufriev, H. Fujita, S. Volz, M. Nomura, “Super-Planckian far-field thermal radiation enabled by guided surface phonon-polaritons”, Submitted.

International conference

1. S. Tachikawa, J. Ordonez-Miranda, Y. Wu, L. Jalabert, R. Anufriev, S. Volz, M. Nomura, “Thickness Dependence of Surface Phonon-Polariton Propagation Length in SiO_2/Si/SiO_2 Structures,” Oral presentation, 2021 Virtual MRS Spring Meeting and Exhibit, NM08.01.02: Late News, online, 2021
2. S. Tachikawa, S. Gluchko, L. Jalabert, H. Fujita, S. Volz, M. Nomura“Near field Radiative Heat Transfer between Parallel Silicon Microstructures”, Poster presentation, PIERS, 4P0 35, Rome, Italy, 2019
3. S. Tachikawa, J. Ordonez-Miranda, Y. Wu, L. Jalabert, R. Anufriev, S. Volz, M. Nomura, “Propagation of surface phonon-polaritons in the multilayer system”, Oral presentation, NAMIS Marathon Workshop, 11, National Tsing Hua University, Taiwan, 2021
4. S. Tachikawa, L. Jalabert, J. Ordonez-Miranda, Y. Wu, R. Anufriev, S. Volz, M. Nomura, “Detection of in-plane Surface Phonon Polaritons”, Oral presentation, NAMIS Marathon Workshop, Session A-7, National Tsing Hua University, Taiwan, 2019

Domestic conference

1. 立川 冴子，オルドネスーミランダ ホセ，ウー ユンフイ，ジャラベール ロラン，アヌフリエフ ロマン，ヴォルツ セバスチャン，野村政宏，“多層膜構造における表面フォノン

ポラリトンの熱伝導コンダクタンスの向上”, 口頭発表, 第 81 回応用物理学会 秋季学術講演会，8a-Z09-7，オンライン開催, 2020

2. 立川 冴子, オルドネス‐ミランダ ホセ, ウー ユンフイ, ジャラベール ロラン, アヌフリエフ ロマン, ヴォルツ セバスチャン, 野村 政宏, ”SiO2/Si/SiO2 構造における表面フォノンポラリトンの伝搬長の膜厚依存性”, ポスター発表, 第 68 回応用物理学会春季学術講演会, 17p-P07-6, オンライン開催、2021
3. 立川 冴子, 野村政宏, “ナノギャップを伝わる熱輸送”, ポスター発表, 第 3 回フォノンエンジニアリング研究会, P-6, 箱根, 7 月 5 日, 2019